

Institut für Angewandte Physik
Fachrichtung Physik
Fakultät Mathematik und Naturwissenschaften
Technische Universität Dresden

**Ultrafast exciton relaxation in
quasi-one-dimensional perylene derivatives**

Dissertation
zur Erlangung des akademischen Grades
Doctor rerum naturalium
(Dr. rer. nat.)

vorgelegt von
Egbert Konstantin Engel
geboren am 28. Februar 1975 in Aalen

Dresden 2005

Eingereicht am 25.11.2005

1. Gutachter: Prof. Dr. K. Leo, Dresden
2. Gutachter: Prof. Dr. P. Petelenz, Krakau
3. Gutachter: Prof. Dr. F. Stienkemeier, Freiburg

Verteidigt am 30.01.2006

JEGESMEDVÉMNEK

Abstract

This thesis deals with exciton relaxation processes in thin polycrystalline films and matrix-isolated molecules of the perylene derivatives PTCDA (3,4,9,10-perylenetetracarboxylic dianhydride) and MePTCDI (N,N'-dimethylperylene-3,4,9,10-dicarboximide). Using femtosecond pump-probe spectroscopy, transient absorption spectra, excitonic relaxation in the lowest excited state subsequent to excitation, and exciton-exciton interaction and annihilation at high excitation densities have been addressed.

Transient absorption spectroscopy in the range 1.2 eV–2.6 eV has been applied to thin polycrystalline films of PTCDA and MePTCDI and to solid solutions of PTCDA and MePTCDI molecules (monomers) in a SiO₂ matrix. We are able to ascribe the respective signal contributions to ground state bleaching, stimulated emission, and excited state absorption. Both systems exhibit broad excited-state absorption features below 2.0 eV, with dominant peaks between 1.8 eV and 2.0 eV. The monomer spectra can be consistently explained by the results of quantum-chemical calculations on single molecules, and the respective experimental polarization anisotropies for the two major transitions agree with the calculated polarizations. Dimer calculations allow to qualitatively understand the trends visible in the experimental results from monomers to thin films. The broad excited state absorption band between 1.8 eV and 2.0 eV allows to probe the population dynamics in the first excited state of thin films. We show that excitons created at the Γ -point relax towards the border of the Brillouin zone on a 100 fs time scale in both systems. Excitonic relaxation is accelerated by increase of temperature and/or excitation density, which is attributed to stimulated phonon emission during relaxation in k -space. Lower and upper limits of the intraband relaxation time constants are 25 fs (resolution limit) and 250 fs (100 fs) for PTCDA (MePTCDI). These values agree with the upper limit for the intraband relaxation time of 10 ps, evaluated from time-resolved luminescence measurements. While the luminescence anisotropy is in full accordance with the predictions made by a luminescence anisotropy model being consistent with the exciton model of DAVYDOV-split states, the pump-probe anisotropy calls for an explanation beyond the models presently available. At excitation densities $> 10^{19} \text{ cm}^{-3}$, the major de-excitation mechanism for the relaxed excitons is exciton-exciton annihilation, resulting in a strongly reduced exciton life time. Three different models for the microscopic behavior have been tested: a diffusion-limited annihilation model in both three and one dimensions (with diffusion constant D as fit parameter) as well as a long-range single-step FÖRSTER-type annihilation model (with FÖRSTER radius R_F as fit parameter). For PTCDA, the latter two, being structurally equivalent, allow to fit a set of multiexponential decay curves for multiple initial exciton densities with high precision. In contrast, the three-dimensional diffusion-limited model is clearly inferior. For all three models, we extract annihilation rates, diffusion constants and diffusion lengths (or FÖRSTER radii), for both room and liquid helium temperature. Temperature dependence and orders of magnitude of the obtained parameters D or R_F correspond to the expectations. For MePTCDI, the 1D and the FÖRSTER model are in good agreement for a smaller interval of excitation densities. For a initial exciton densities higher than $5 \times 10^{19} \text{ cm}^{-3}$, the 3D model performs significantly better than the other two.

Contents

1. Introduction	1
2. Quasi-1D organic molecular crystals	3
2.1. Organic molecular crystals	3
2.1.1. Isolated molecules	4
2.1.2. From molecules to molecular crystals	5
2.2. The perylene derivatives MePTCDI and PTCDA	8
2.3. Exciton band structure models	11
2.3.1. Quasi-1D band structure model	12
2.3.2. Alternative models	15
2.3.3. Davydov splitting and Davydov components	16
2.4. Questions of interest	17
3. Techniques of ultrafast spectroscopy	21
3.1. Pulsed light	21
3.1.1. Pulse length, pulse shape, bandwidth limitation	21
3.1.2. Propagation of a light pulse through dispersive media	23
3.2. Generation of ultrashort tunable pulses	26
3.2.1. Ti:sapphire amplifier system	26
3.2.2. Continuum generation	28
3.2.3. Optical parametric amplification	31
3.3. Pulse characterization and manipulation	32
3.3.1. Optical correlation	32
3.3.2. Pulse compression	33
3.3.3. The acousto-optic programmable dispersive filter (AOPDF)	34
3.4. Spectroscopic methods	38
3.4.1. Transient transmittance spectroscopy	38
3.4.2. CW absorption and emission, time-resolved luminescence	41
4. Transient absorption spectra of PTCDA and MePTCDI	43
4.1. Linear absorption and emission spectra	43
4.1.1. Matrix-isolated molecules	43
4.1.2. Thin polycrystalline films and monomers in solution	44
4.1.3. Comparison of linear spectra	45
4.2. Transient absorption spectra of matrix-isolated systems	46
4.2.1. MePTCDI transient absorption	48
4.2.2. PTCDA transient absorption	50
4.2.3. Anisotropy and transition dipole moments	51

4.2.4.	Assignment by means of quantum-chemical calculations	53
4.3.	Transient absorption spectra of thin films	56
4.3.1.	MePTCDI and PTCDA transient absorption	56
4.3.2.	From monomer to thin film	58
5.	Exciton dynamics: Photoluminescence and intraband relaxation	61
5.1.	Time-resolved photoluminescence	61
5.1.1.	Relaxation into the emitting states	61
5.1.2.	Davydov splitting and luminescence anisotropy	63
5.2.	Ultrafast intraband relaxation	70
5.2.1.	Depopulation of the absorbing states	70
5.2.2.	Intensity and temperature dependence	76
5.2.3.	Pump-probe anisotropy	82
6.	Exciton-exciton interaction and annihilation at high excitation densities	85
6.1.	Annihilation models	85
6.1.1.	Introduction	85
6.1.2.	Three-dimensional annihilation	86
6.1.3.	One-dimensional annihilation	87
6.1.4.	Förster-type interaction and annihilation	88
6.2.	Application of annihilation models	89
6.2.1.	Fits to experimental data	89
6.2.2.	Summarized fit results	95
7.	Summary and outlook	101
7.1.	Summary	101
7.2.	Outlook	103
A.	Quantum-chemical calculations	105
	Bibliography	111
	List of Symbols and Abbreviations	123
	Publications	125
	Acknowledgments	127

1. Introduction

The market volume of about 400 million US-dollars in 2004 and 2005 [1] for passive matrix displays based on organic (i. e., composed primarily of hydrocarbons) electroluminescent material is a clear evidence that the field of organic light emitting devices has emerged from its early stages of invention [2, 3], surpassed the level of mere innovation, and reached the stage of industrial production. Typical fields of application so far are consumer electronics with small to medium size displays for cell phones or PDAs¹, but also some flat TV displays with tens of inches in diagonal have been developed. Forecasts envision large area lighting applications or displays on disposable flexible substrates. Flexibility is also very attractive for “plastic electronic” devices, containing, e. g., organic transistors [4].

In contrast to the organic LED, organic solar cells have not yet reached a comparable level of maturity. Twenty years after their first presentation [5], the power conversion efficiencies do not exceed a few percent, in contrast to some 15% for industrial solar cells based on silicon. Nevertheless, intensive research is carried out in this field on the way to finding materials promising higher efficiencies.

One principal reason why new technologies conquer the market are low cost in combination with favorable or improved properties. Organic solar cells and OLEDs are heterostructures typically made of multiple thin films that can be produced on a large scale by sequential evaporation, or – in the case of polymers – by inkjet printing or spin coating. These manufacturing processes are simple and cheap, compared to the processing of inorganic semiconductors. Another particular advantage of thin-film devices from organic material is the unlimited variety of the organic synthesis, which in principle allows to custom-tailor highly specialized substances. Still, despite the existing commercial applications, the microscopic understanding of the electronic and related optical properties and relaxation processes in organic semiconducting material is still rather limited, compared to their inorganic counterparts. The numerous degrees of freedom hamper the theoretical understanding, which calls for more profound experimental efforts.

The group of organic material for device applications is commonly divided into polymers and “small molecules”. In this context, “small’ is meant relative to the size of polymer chains, and small molecules usually contain some tens of carbon atoms, such as, e. g., perylene (20 atoms) or C₆₀ (60 atoms). Besides, one separates amorphous molecular materials on the one hand from crystalline materials on the other hand, with the molecules as structural units. Molecular crystals are weakly bound by VAN DER WAALS forces, which results in bonding energies significantly smaller than those of covalent or ionic bonds. Hence, in contrast to covalently bound semiconductor crystals, where the electronic structure of the valence electrons is largely determined by the crystal formation, the weak VAN DER WAALS forces evoke only moderate changes in the molecules

¹Personal digital assistants

upon formation of the crystal lattice, and the molecules mainly retain their individual identities.

In this thesis, we aim at crystals of small molecules of the perylene derivatives 3,4,9,10-perylenetetracarboxylic dianhydride (PTCDA) and N,N'-dimethylperylene-3,4,9,10-dicarboximide (MePTCDI). A characteristic property of these materials is their ability to form molecular crystals with a highly anisotropic structure. In particular, the crystals are called quasi-one-dimensional (quasi-1D), because the lattice constant in one direction is much smaller than the other two lattice constants. This results in a columnar stacking of the molecules and a strong interaction of adjacent molecules in the stack, which leads to the formation of strong excitonic bands. PTCDA and MePTCDI can be regarded as paradigmatic representatives of quasi-1D materials.

For device applications, the understanding of the lowest excited states is of essential importance. In PTCDA and MePTCDI crystals, these states can be excited by illumination with visible light with photon energies above 2 eV. Due to the strong interaction between electron and hole in these molecules, bound exciton states are created rather than free charge carriers. Our particular aim is to understand the various relaxation processes of these photo-generated excitons which follow optical excitation in polycrystalline films of PTCDA and MePTCDI. Before it is possible to make statements about relaxation time constants and relaxation pathways, it is first mandatory to understand the higher excited states of PTCDA and MePTCDI films. Since these states are closely related to the excited states of the monomers, we will first address isolated molecules and apply our knowledge to explain the film spectra afterwards. Our discussions of the relaxation process will be done in the framework of exciton band structure models, currently the only microscopic picture used for the description of the optical spectra of such materials. Since the excitonic relaxation processes happen on an ultrafast time scale in the fs- and ps-regime, we employ femtosecond pump-probe spectroscopy as experimental tool.

This thesis is divided into five chapters and a subsequent summary. Chapter 2 presents the model systems PTCDA and MePTCDI in more detail. Besides, the theoretical base-ment for the understanding and discussion of the key questions will be laid. We will elaborate on the extensive experimental pump-probe setup in Chapter 3. Therefore, some concepts of pulsed and nonlinear optics have to be introduced at the beginning of the chapter. Presentation of the experimental results start with Chapter 4, where we will illustrate transient absorption spectra of MePTCDI and PTCDA monomers and thin films. The spectra will be discussed in comparison with results from quantum-chemical calculations. Based on the conclusions of this chapter, we will tackle the question of relaxation of excitons subsequent to excitation in the Brillouin zone from the absorbing state to the emitting state in Chapter 5. The findings of this chapter about the dependence of this process on excitation intensity will lead us to the question of exciton-exciton interaction and annihilation, which we will report on in Chapter 6.

2. Quasi-1D organic molecular crystals

It was noted in the introduction that the properties of the excited states of organic molecular crystals (OMCs) are primarily determined by the properties of the molecules they are built of. This chapter starts with a brief introduction of the fundamentals being applied to obtain the energetic states and bands of OMCs from the molecular states in Sect. 2.1. Afterwards, we will present our quasi-one-dimensional model systems PTCDA and MePTCDI. In Sect. 2.3, the concepts of optical absorption, subsequent relaxation and emission are discussed in the framework of band structure models. We will finish this chapter with Sect. 2.4 by raising open questions about excitonic relaxation processes being addressed in this thesis.

2.1. Organic molecular crystals

In principle, there are two different approaches to describe the optical properties of a semiconductor crystal. One approach is usually applied to systems where the exciton formation is a small energetic effect in comparison with the formation of one-particle bands. The starting point is to introduce one-particle states and to refine these states by the inclusion of correlation effects. The resulting many-particle states, such as WANNIER-MOTT excitons, are called large-radius excitons, because the rather weak interaction between electron and hole leads to a large distance between them. This concept is commonly applied to inorganic semiconductors¹.

In contrast to this method, one can also start from the isolated molecule (monomer) and then introduce intermolecular interactions. Such an approach makes sense if the exciton binding energy is large compared to the one-particle bandwidths, which is typically the case in molecular crystals, being weakly bound by VAN DER WAALS-interaction². The most basic representation of such a small radius exciton theory considers only FRENKEL excitons (FE), assuming electron and hole to be located on the same molecule. Ground and excited states of the crystal can then be described by a many-electron wave function which is formed out of a basis of single molecular wave functions [9]. In this case, the eigenstates are more closely related to molecular states than to one-particle crystal states. Intermolecular interaction gives rise to a finite hopping integral for the transfer of the excitation from one molecule to one of its neighbors³.

Small radius exciton theories require the understanding of isolated molecules prior to discussion of interaction effects in the crystal. In this section, the basic concepts are only outlined, based upon common literature such as [6, 9–11].

¹In GaAs, for example, the binding-energy of the WANNIER-MOTT exciton of 4.2 meV is small compared to the one-particle bandwidth of ~ 2 eV (see, e. g., [6]).

²Even for PTCDA with its coplanar stacking, the binding energy of the lowest excitation is about 1 eV (derived from [7]), while the one-particle bandwidth is on the order of 0.2 eV [8].

³An additional type of exciton, the charge-transfer exciton (CTE), will be introduced later in this section.

2.1.1. Isolated molecules

Adiabatic approximation Generally, the problem to be solved to obtain the wave function Ψ_x^{tot} for an arbitrary stationary eigenstate x of a molecule is the time-independent SCHRÖDINGER equation:

$$\hat{H}^{\text{tot}} \Psi_x^{\text{tot}}(r_i, R_A) = E_x^{\text{tot}} \Psi_x^{\text{tot}}(r_i, R_A). \quad (2.1)$$

Here, r_i are the coordinates of the electrons with masses m_{el} and R_A the coordinates of the nuclei with masses M_{nuc} . The Hamiltonian takes the following form:

$$\hat{H}^{\text{tot}} = \hat{T}_{\text{el}} + V_{\text{el-el}} + V_{\text{el-nuc}} + V_{\text{nuc-nuc}} + \hat{T}_{\text{nuc}}, \quad (2.2)$$

where T_{el} and T_{nuc} are kinetic energies of the electrons and nuclei, respectively. The COULOMB interaction potentials between electrons is $V_{\text{el-el}}$, between nuclei $V_{\text{nuc-nuc}}$, and between electrons and nuclei $V_{\text{el-nuc}}$.

An essential step towards the solution of Eqs. (2.1, 2.2) is the BORN-OPPENHEIMER approximation or *adiabatic approximation*: Since the mass of an electron is much smaller than of a nucleus ($m_{\text{el}} \ll M_{\text{nuc}}$), the electrons react instantaneously to changes of the nuclear configuration. The problem can then be simplified to finding a solution for a fixed set of (parametric) values $\{R_A\}$ for the nuclear coordinates. This motivates to separate the total wave function Ψ_x^{tot} with $x = (n, m)$ into an electronic part Ψ_n and a vibrational part $\chi_{n,m}$:

$$\Psi_x^{\text{tot}} = \Psi_n(r_i) \Big|_{\{R_A\}} \chi_{n,m}(R_A). \quad (2.3)$$

In Eq. (2.3), Ψ_n is the wave function for all electron coordinates r_i for a fixed nuclear configuration and obeys the SCHRÖDINGER equation for the electrons⁴

$$\hat{H}^{\text{el}} \Psi_n(r_i) = E_n^{\text{el}} \Psi_n(r_i) \quad \text{with} \quad \hat{H}^{\text{el}}(r_i) = \hat{T}_{\text{el}}(r_i) + V_{\text{el-el}}(r_i) + V_{\text{el-nuc}}(r_i). \quad (2.4)$$

$\chi_{n,m}(R_A)$ is the wave function of the nuclei and solves the vibrational problem for the m -th phononic state of the electronic state n with energy E_n^{el} :

$$\hat{H}^{\text{vib}} \chi_{n,m}(R_A) = E_{n,m}^{\text{vib}} \chi_{n,m}(R_A) \quad \text{with} \quad \hat{H}^{\text{vib}} = \hat{T}_{\text{nuc}}(R_A) + E_n^{\text{el}}(R_A). \quad (2.5)$$

The total excitation energy relative to the ground state,

$$\Delta E_{n,m} = (E_n^{\text{el}} + E_{n,m}^{\text{vib}}) - E_0^{\text{el}}, \quad (2.6)$$

is thus a sum of the electronic and the vibrational part. Application of the adiabatic approximation is only valid if the electronic state does not change during the nuclear vibration and implies $\Delta E^{\text{vib}} \ll \Delta E^{\text{el}}$.

⁴Electron spin is neglected.

One-particle wave functions Since an analytical solution for the $\Psi_n(r_i)$ cannot be found for more than two electrons, the common procedure is to consider only a single electron in an effective potential v^{eff} defined by the states of all other particles and to start with one-particle basis functions $\varphi_m(r)$. We thus obtain the one-particle SCHRÖDINGER equation:

$$\hat{h}^{\text{eff}} \psi_n(r) = \epsilon_n \psi_n(r), \quad (2.7)$$

where $\hat{h}^{\text{eff}} = \hat{t}_{\text{el}} + v^{\text{eff}}$ is an effective Hamiltonian and ϵ_n the eigenvalue for the eigenstate ψ_n . The matrix-elements of \hat{h}^{eff} can be computed by

$$h_{m,n}^{\text{eff}} = \langle \varphi_m | \hat{h}^{\text{eff}} | \varphi_n \rangle. \quad (2.8)$$

The wave functions ψ_n can be approximated by a superposition of basis functions φ_m , i. e.,

$$\psi_n = \sum_m c_{n,m} \varphi_m. \quad (2.9)$$

Solving the SCHRÖDINGER equation Eq. (2.7) then allows to calculate a new effective potential v^{eff} from the ψ_n . Multiple additional iterations of this procedure help to sequentially refine the solution for the ψ_n and ϵ_n . Correlations between the particles (many-body effects) are introduced in a next step via configuration interaction.

2.1.2. From molecules to molecular crystals

We now sketch how to obtain one-particle electronic bands from the molecular orbitals, if we apply the results for the monomer and transfer them to the crystal. Since we consider FRENKEL (molecular) excitons, the best approach is to use the molecular excited states to deduce the excited states of the crystal. This is referred to as *Frenkel exciton theory*, where the strong interaction between electron and hole is already included in the solution for the molecular states.

Tight-binding Hamiltonian Throughout the following discussion, we consider a linear (one-dimensional) crystal with N molecules and periodic boundary conditions. Let $\Psi_n^{0,1}$ be the molecule at lattice site n in its ground or first excited state, respectively. Higher excited states are not considered now. The ground state $|0\rangle$ of the linear crystal is then given by the product of molecular wave functions:

$$|0\rangle = |\dots \Psi_{n-1}^0 \Psi_n^0 \Psi_{n+1}^0 \dots\rangle, \quad (2.10)$$

and the first excited state $|n\rangle$ with one exciton at site n by

$$|n\rangle = |\dots \Psi_{n-1}^0 \Psi_n^1 \Psi_{n+1}^0 \dots\rangle. \quad (2.11)$$

As noted above, the interaction between hole and electron is already included in Ψ_n^1 . The product wave functions $|n\rangle$ are considered orthogonal, i. e., $\langle m | n \rangle = \delta_{m,n}$. The

2. Quasi-1D organic molecular crystals

excitation may be transferred to adjacent molecules in the chain, which motivates to write the matrix elements of the exciton Hamiltonian \hat{H}^{Ex} as:

$$m = n : h_{m,m} = \langle m | \hat{H}^{\text{Ex}} | n \rangle = \epsilon_m \quad \text{on-site energy} \quad (2.12)$$

$$m \neq n : h_{m,n} = \langle m | \hat{H}^{\text{Ex}} | n \rangle = J_{m,n} \quad \text{exciton-hopping integral} . \quad (2.13)$$

The essential correlation effect introduced here is the matrix element $J_{m,n}$ of the FRENKEL transfer integral J between two exciton configurations. Hence, the major task is to find an appropriate representation of J . For this purpose, it is helpful to formulate the problem in second quantization notation and to solve it in the momentum space.

In second quantization notation, the tight-binding Hamiltonian takes the following form:

$$\hat{H}^{\text{Ex}} = \sum_n \epsilon_n a_n^\dagger a_n + \sum_{\substack{m,n \\ m \neq n}} J_{m,n} a_m^\dagger a_n , \quad (2.14)$$

where a_n^\dagger and a_n are operators to create and annihilate an exciton at site n , respectively:

$$a_n^\dagger |0\rangle = |n\rangle \quad (2.15)$$

$$a_n |n\rangle = |0\rangle . \quad (2.16)$$

Momentum space \hat{H}^{Ex} in Eq. (2.14) is in general not diagonal. The site index n is thus no good quantum number. Transferring the problem to the momentum space, however, allows for some simplifications that essentially diagonalize \hat{H}^{Ex} . In order to replace the site index n by a quasi-continuous quantum number k , we FOURIER-transform the operators a_n and a_n^\dagger :

$$a_k = \frac{1}{\sqrt{N}} \sum_n e^{-ikn} a_n \quad a_k^\dagger = \frac{1}{\sqrt{N}} \sum_n e^{ikn} a_n^\dagger , \quad (2.17)$$

where for the quantum number k holds:

$$k = \frac{2\pi}{N} l \quad -\frac{N}{2} < l \leq \frac{N}{2} \quad (2.18)$$

As $N \rightarrow \infty$, $\Delta k \rightarrow 0$, and k becomes continuous. The back-transformation of Eq. (2.17) is given by:

$$a_n = \frac{1}{\sqrt{N}} \sum_k e^{ikn} a_k \quad a_n^\dagger = \frac{1}{\sqrt{N}} \sum_k e^{-ikn} a_k^\dagger , \quad (2.19)$$

If we introduce the momentum representations of a_n and a_n^\dagger in Eq. (2.19) into \hat{H}^{Ex} in Eq. (2.14), we obtain⁵:

$$\hat{H}^{\text{Ex}} = \sum_k (\epsilon_0 + L_k) a_k^\dagger a_k , \quad (2.20)$$

⁵During this step the translation symmetry comes into play:

$$\epsilon_m = \epsilon_{n-x} = \epsilon_n \quad \text{and} \quad J_{m,n} = J_{m,n-x} = J_{m,0} .$$

where L_k is the ‘‘lattice sum’’

$$L_k = \sum_{m \neq 0} e^{ikm} J_{0,m} . \quad (2.21)$$

As can be clearly seen in Eq. (2.20), the Hamiltonian \hat{H}^{Ex} now is diagonal, i. e., there is no transfer between any states k and k' . k is thus a good quantum number. Another particular advantage of the momentum representation is that the eigenstates $|k\rangle$ and the eigenvalues $\epsilon(k)$ can be written down immediately:

$$|k\rangle = a_k^\dagger |0\rangle = \frac{1}{\sqrt{N}} \sum_n e^{ikn} |n\rangle \quad (2.22)$$

$$\epsilon(k) = \epsilon_0 + L_k = \epsilon_0 + \sum_{m \neq 0} e^{ikm} J_{0,m} . \quad (2.23)$$

In the one-dimensional case, the lattice sum L_k converges rapidly, so that the nearest-neighbor approximation ($m = \pm 1$) is usually sufficient. We thus obtain the following approximation for a the *exciton band* in a one-dimensional crystal:

$$\epsilon(k) = \epsilon_0 + 2J \cos k . \quad (2.24)$$

$\epsilon(k)$ describes a continuous (as $N \rightarrow \infty$) band of energy values for a continuous k with a single parameter J and the bandwidth $4|J|$. Reasonable values for J can already be derived from first order point-dipole approximations for the molecules. Depending on the orientation of the point dipoles, J becomes either positive or negative. For $J > 0$, the system is called an *H-aggregate*, and the exciton dispersion $\partial\epsilon/\partial k$ is negative, which implies that the Γ -point at $k = 0$ is the highest state in k -space. If $J < 0$, we talk of a *J-aggregate* with a positive exciton dispersion and with the lowest state at $k = 0$ ⁶. Both cases are schematically shown in the center panel of Fig. 2.1.

For spectroscopy, it is important to know which excited crystal states are involved in optical transitions. It can be shown that the total transition dipole moment \mathbf{P} of the crystal can be written as:

$$\mathbf{P} = \delta_{kk'} \sqrt{N} \mathbf{p} , \quad (2.25)$$

where k is the crystal wave vector, k' the wave vector of the light wave, and \mathbf{p} a molecular transition dipole moment. For visible light, the wavelength λ' is large compared to the lattice constant. Since the momentum conservation in Eq. (2.25) requires $k = k' = 2\pi/\lambda'$, absorption (or emission) of light is only possible if $k = k' = 0$. This means that optical transitions are only allowed at the Γ -point. This constraint leads to very different behavior for H-aggregates and J-aggregates, as depicted in Fig. 2.1. For J-aggregates, the lowest state is at $k = 0$, which results in both absorption and emission at the Γ -point⁷. For H-aggregates, absorption at the Γ -point is followed by a very rapid

⁶J-aggregates are extensively studied in [12].

⁷Yet, STOKES shift from additional interactions is responsible that the wavelengths for absorption and emission usually differ.

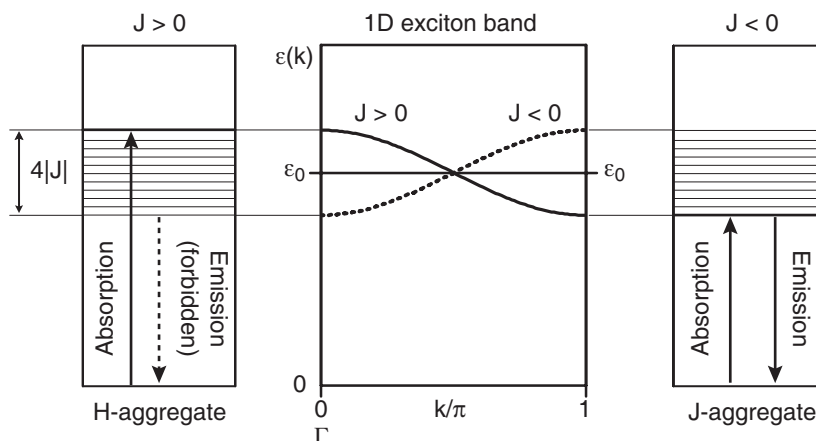


Figure 2.1.: One-dimensional exciton band scheme for positive and negative values of equal size of the FRENKEL transfer integral J . Center panel: $\epsilon(k)$ after Eq. (2.24) as a function of wave vector k for $J > 0$ (solid line) and $J < 0$ (dotted). Left panel: For $J > 0$, emission from the lowest state at $k = \pi$ is dipole forbidden. Right panel: Absorption and emission can occur at the Γ -point ($k = 0$). In both cases, the exciton bandwidth is $4|J|$.

relaxation in k -space. Since the lowest state is at $k = \pi$, luminescence is forbidden unless the momentum conservation is fulfilled by support of a lattice phonon.

The presented approach to obtain exciton bands in a linear crystal is only the simplest possible case. For additional effects, the Hamiltonian in Eq. (2.14) is to be refined accordingly. Relevant examples for possible effects are as follows:

- More than one molecule per unit cell results in additional exciton wave functions, which essentially results in additional bands (one per molecule per unit cell). The resulting “DAVYDOV-splitting” between these bands will be discussed in Sect. 2.3.3.
- The transition from a 1D to a 3D system is formally done by introduction of site vectors \mathbf{n} and 3D wave vectors \mathbf{k} instead of scalars. Yet, the 3D lattice sum $L_{\mathbf{k}}$ (cf. Eq. (2.21)) may not converge as easily as in the 1D case.
- More sophisticated exciton models encompass additional effects such as transfer of the hole or electron to an adjacent molecule (*charge-transfer excitons*). In Sect. 2.3, we will present band models for perylene derivatives including charge-transfer states.
- Interaction between excitons and molecular or lattice vibrations (phonons) has not yet been considered. This will also be addressed in Sect. 2.3.

2.2. The perylene derivatives MePTCDI and PTCD A

The increased interest in organic molecular crystals concentrates on finding materials with promising properties for optoelectronic devices. Especially the demand for reasonably high charge carrier mobilities has led to materials with strong intermolecular interaction. In addition to the demand for exciton energies in the visible range, much

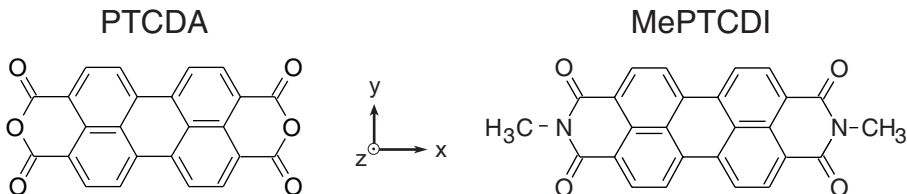


Figure 2.2.: Chemical structures of 3,4,9,10-perylenetetracarboxylic dianhydride (PTCDA) and *N,N'*-dimethylperylene-3,4,9,10-dicarboximide (MePTCDI), together with the molecular coordinate system. The PTCDA molecule and the carbon backbone of the MePTCDI molecule share a D_{2h} symmetry.

research has aimed at planar π -conjugated aromatic molecules with substituents at the periphery of the molecules that allow to fine-tune the optical spectra to accommodate specific requirements. Combination of the need for flatness and strong intermolecular interaction has made systems with coplanar arrangement with small intermolecular distance preferable. Prominent examples are derivatives of the perylenetetracarboxylic acid (PTC-derivatives, or also perylene derivatives) [13–15] and phthalocyanine dyes [16].

In framework of this thesis, we consider two of the most prominent perylene derivatives as model compounds, namely PTCDA (3,4,9,10-perylenetetracarboxylic dianhydride) and MePTCDI (*N,N'*-dimethylperylene-3,4,9,10-dicarboximide), cf. Fig. 2.2. PTCDA has become a paradigmatic material because it has been shown to readily form highly ordered films [17, 18], where the molecules are oriented parallel to various substrates. Various other perylene derivatives, among them also MePTCDI, have solar cell applications [5, 19–21]. For typical devices, polycrystalline thin films in the nanometer range made by vapor deposition are of particular interest. For this reason, this work focuses on investigations of thin films of 25–35 nm thickness.

Figure 2.3 depicts the crystal structure for MePTCDI as given in [14]. The structure is monoclinic centrosymmetric, and the unit cell contains $Z = 2$ molecules. Additional parameters are given in the caption of Fig. 2.3. The planar molecules arrange face-to-face, which results in a closely stacked structure along one lattice direction. In MePTCDI, the in-stack lattice constant is $a = 3.87 \text{ \AA}$, which is not only significantly smaller than the other lattice constants, but also small compared to the size of the molecule (*N-N'*-distance: 11.3 \AA). Hence, the crystal can be regarded as a two-dimensional array of one-dimensional stacks. Therefore, MePTCDI (and also PTCDA) crystals are considered paradigmatic representatives of *quasi-1D* systems.

A particular property of such a quasi-1D system is the strong mutual overlap of the π -electron systems, which leads to the strong coupling or *strong molecular overlap* between adjacent molecules⁸. Although two neighboring molecules in the stack are shifted with respect to each other within the molecular plane, this overlap of the π -systems still amounts to $\approx 50\%$. For MePTCDI, this is depicted in the lower right corner of Fig. 2.3. The strong intermolecular overlap leads to the expectation of large electronic

⁸Planar molecules alone need not necessarily lead to a strong overlap of the π -systems and a stacked structure: For example, anthracene molecules are perfectly flat, but the molecules do not at all lie above each other (crystal structure data for anthracene are given in [16]).

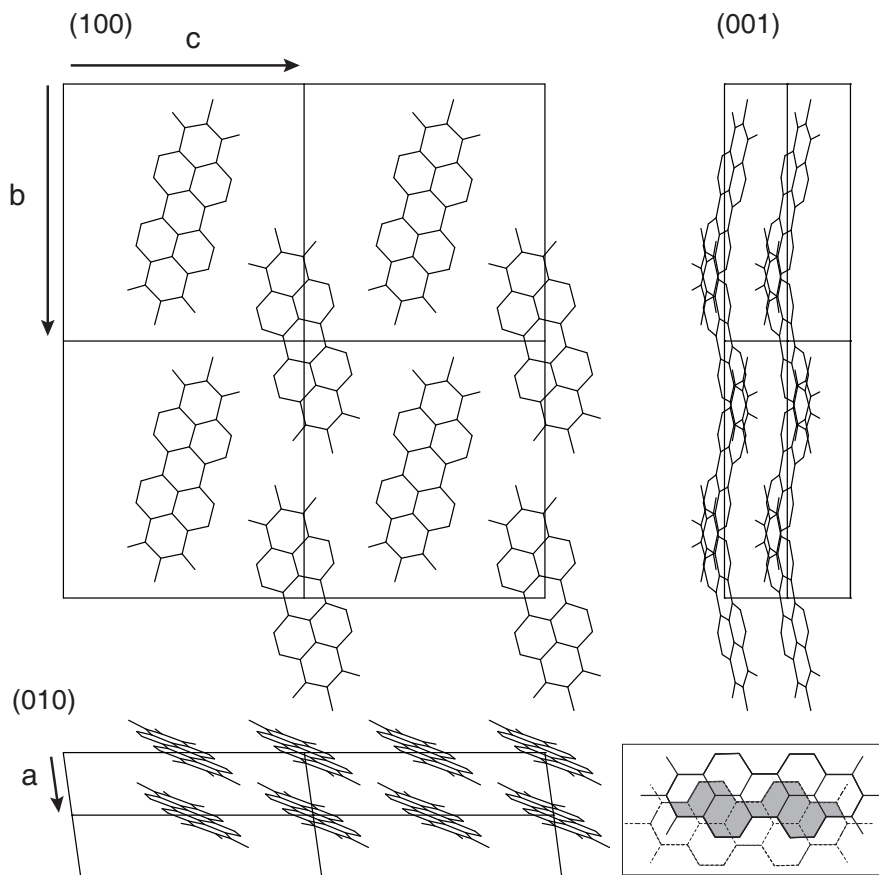


Figure 2.3.: Crystal structure of MePTCDI, derived from [14]. Shown are projections of 2×2 unit cells onto the b - c -plane (100), the a - b -plane (001), and the a - c -plane (010). The crystal structure is monoclinic centrosymmetric with $Z=2$ molecules per unit cell, $a = 3.87 \text{ \AA}$, $b = 15.58 \text{ \AA}$, $c = 14.60 \text{ \AA}$, $\beta = 97.65^\circ$. The frame in lower right corner depicts the mutual overlap of two adjacent molecules in the stack.

bandwidths and high charge carrier mobility. Yet, the reported electron mobility values for PTCDA did not exceed $3 \times 10^{-2} \text{ cm}^2/\text{Vs}$ for vapor-deposited layers at room temperature [22]. However, these values might still be limited by impurities, which calls for new measurements with single crystals of highest purity.

Evidence for the quasi-1D nature of MePTCDI can be seen in the fact that the interaction between translationally inequivalent stacks of molecules (cf. Fig. 2.3) is much smaller than the in-stack coupling, as inferred from the observation of DAVYDOV-splitting [23], which will be addressed in Sect. 2.3.3.

As for the PTCDA crystal, the structure is shown in Fig. 2.4, with structural data from [24]. In general, the same statements about strong intermolecular coupling valid for MePTCDI also apply to PTCDA: the lattice constant in stacking direction (3.72 \AA) is much smaller than the other two lattice constants, making PTCDA also a quasi-1D system. PTCDA also contains two molecules per unit cell arranged under an angle of

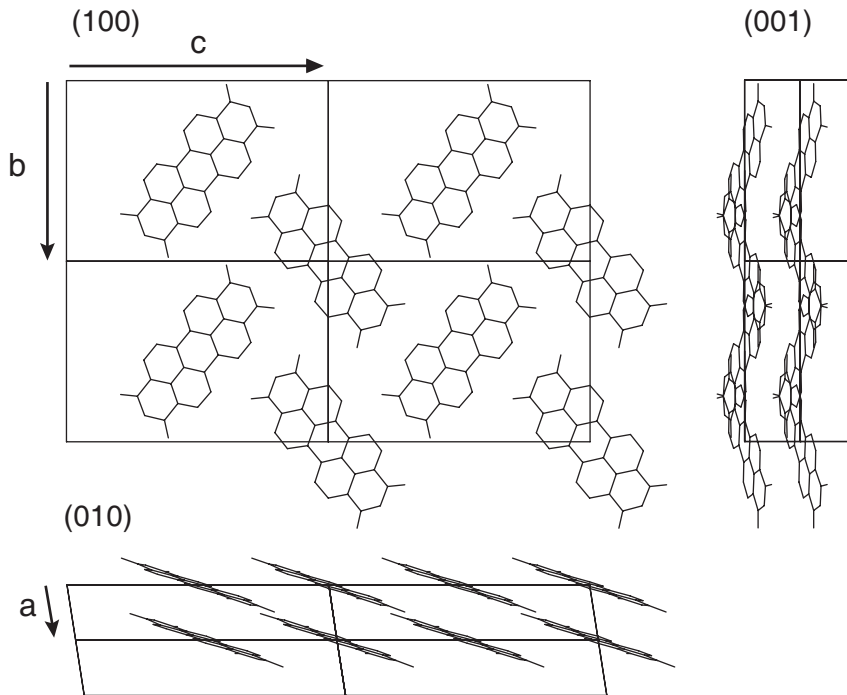


Figure 2.4.: Crystal structure of α -PTCDA, derived from [24]. Shown are projections of 2×2 unit cells onto the b - c -plane (100), the a - b -plane (001), and the a - c -plane (010). The crystal structure is monoclinic centrosymmetric with $Z=2$ molecules per unit cell, $a = 3.72 \text{ \AA}$, $b = 11.96 \text{ \AA}$, $c = 17.34 \text{ \AA}$, $\beta = 98.8^\circ$.

nearly 90° in a herringbone-like structure.

The PTCDA structure in Fig. 2.4 refers to the α -phase of PTCDA. It has been shown that deposition at room temperature preferentially results in films of the α -phase, whereas the β -phase preferentially grows at low substrate temperatures [25, 26]. Apart from the fact that our samples were grown by deposition on room-temperature substrates and should therefore predominantly consist of the α -phase, the difference in the spectra is small [26]. For these reasons, we need not consider this polymorphism in our investigations.

2.3. Exciton band structure models

Our particular interest lies in the investigation of (time-resolved) excitonic relaxation processes in thin films of MePTCDA and PTCDA, preferably for optoelectronic device applications. Therefore, the microscopic understanding of the lowest excited state in these materials is of essential importance for us. This motivates to apply the formalism outlined in Sect. 2.1 to our quasi-1D model systems, and to seek to understand optical transitions in the framework of band structure models.

Before turning to the treatment of the crystal, however, we summarize some properties of PTCDA and MePTCDA monomers being helpful for further considerations. A major

advantage of the PTCDA-derivatives is their simple molecular behavior. The lowest electronic excitation is a dipole-allowed $\pi - \pi^*$ transition, with a strong transition dipole along the long molecular axis of the molecule [27–30]. Using the molecular coordinate system in Fig. 2.2, we identify this direction as the x-direction. The electronic excitation couples predominantly to one effective vibrational mode of the carbon backbone, which dominates the absorption and emission spectra. Figure 2.5 (a) depicts this for MePTCDI in solution. Emission spectra of MePTCDI and PTCDA in solution are shown in Figs. 4.1 and 4.2⁹. The range above 2.2 eV up to 3.0 eV in Fig. 2.5 (a) is referred to as S_1 manifold. Around 3.4 eV, there is another small absorption feature [23] from the $S_0 \rightarrow S_2$ -transition, which is related to a transition dipole moment oriented along the short molecular y-axis [27, 28].

2.3.1. Quasi-1D band structure model

Upon formation of the crystal, the molecular excitonic states form excitonic bands, as outlined in Sect. 2.1.2. In principle, the one-dimensional approach with the tight-binding Hamiltonian for FRENKEL excitons (FE) from Eq. (2.14) is still applicable, yielding the result for the 1D exciton band in Eq. (2.24). Yet, the above treatment is too simple to adequately describe the optical spectra and requires the inclusion of additional effects. Various band structure models [8, 23, 36–40] have addressed this subject with increasing complexity and sought to understand absorption and emission spectra as well as properties of the electronic excitations. Throughout this work, we will use the model of HOFFMANN et al. [8, 23, 34] for quasi-1D systems with strong intermolecular overlap as a basis and a framework for further considerations and discussion¹⁰. The result for a MePTCDI crystal is shown in Fig. 2.5, and we will briefly outline the underlying concepts. It is worth mentioning at this stage that this preferential choice does not affect the conclusions drawn from the experimental results in the Chapters 4–6.

Due to the strong overlap of the π -systems in stack direction, the concept of the molecular FRENKEL exciton is not sufficient anymore. This overlap leads to a decreased energy of the lowest charge-transfer exciton (CTE) states, where electron and hole are located on different molecules. In this case, strong mixing between FE and CTE occurs. For the simplest case of a dimer, this mixing of two FRENKEL and two CT states leads to 2×2 supermolecular dimer states, either two of even or odd symmetry. In the crystal, this results in the electronic bands depicted in Fig. 2.5 (d), where any vibronic coupling of the mixed FE/CT states is omitted. The strongest support to incorporate CT states is the interpretation of electroabsorption spectra [38, 39], rather than the linear absorption spectra. Still, the detailed shape and the polarization dependence of the absorption spectra are additional arguments in favor of the charge-transfer exciton.

In addition to the inclusion of CT states, HOFFMANN et al. considered the linear coupling of both FE and CTE to the effective internal vibrational mode, using a HOLSTEIN

⁹The “effective mode” actually has a vibrational substructure, resolved for PTCDA films by RAMAN spectroscopy. Helium nanodroplet isolation spectroscopy (*HENDI*, cf. [31]) with very high resolution has successfully been applied to PTCDA monomers [32] and MePTCDI monomers [33].

¹⁰We will also address the developments of MAZUR et al. [39] and VRAGOVIĆ and co-workers [40] in Sect. 2.3.2.

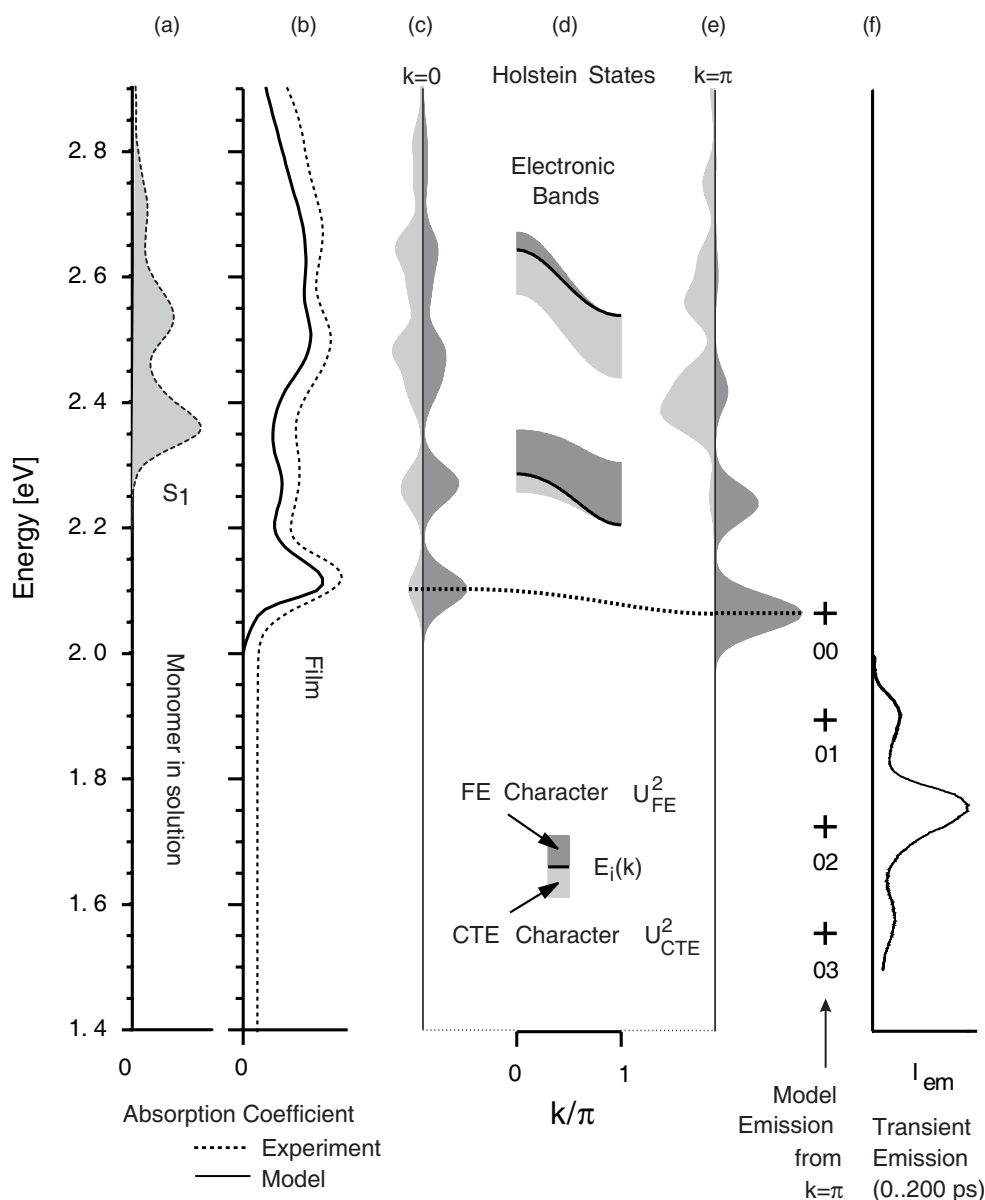


Figure 2.5.: Excitonic band structure for MePTCDI and experimental spectra (adapted from [34]). Leftmost panel (a): absorbance of MePTCDI molecules in chloroform solution (concentration $0.3 \mu\text{mol/l}$, from [23]). Panel (b) depicts the experimental (dashed line) and the calculated (solid line) absorption spectra for an MePTCDI crystal. Panels (c) and (e) show the vibronic model states from the HOLSTEIN formalism, either at $k=0$, or at $k=\pi$. Net contributions are summarized by shaded areas, either with FRENKEL character (dark gray) or CT character (light gray). Panel (d) depicts the purely electronic dispersion of the FE-CTE mixing bands, without any coupling to the phonon modes from the HOLSTEIN model. Rightmost panel (f): emission from an MePTCDI single crystal at 10 K, measured by CANZLER [35], together with the calculated emission energies at $k=\pi$ to vibrational levels of the ground state. The 00-transition is strictly dipole forbidden. The dotted line symbolizes the excitonic band with negative dispersion in the lowest S_1 state. A corresponding band structure for PTCDA can also be found in [34].

2. Quasi-1D organic molecular crystals

model [41, 42], allowing not only vibrations of the excited molecule, but also displaced exciton-phonon configurations over the complete stack. In total, the Hamiltonian has the following shape:

$$\hat{H}_{\text{Hol}}^{\text{FCT}} = \hat{H}_{\text{Hol}}^{\text{FE}} + \hat{H}^{\text{CT}} + \hat{H}^{\text{CT-ph}} + \hat{H}^{\text{FE-CT}}, \quad (2.26)$$

where $\hat{H}_{\text{Hol}}^{\text{FE}}$ is the complete 1D HOLSTEIN Hamiltonian containing linear coupling between exciton and phonon systems:

$$\hat{H}_{\text{Hol}}^{\text{FE}} = \hat{H}_{\text{elec}}^{\text{FE}} + \hat{H}^{\text{ph}} + \hat{H}^{\text{FE-ph}}. \quad (2.27)$$

We will not go into too much detail and discuss explicit expressions for all operators in Eqs. (2.26) and (2.27), but only mention their purpose. In fact, $\hat{H}_{\text{elec}}^{\text{FE}}$ corresponds to the pure electronic FRENKEL Hamiltonian \hat{H}^{Ex} in Eq. (2.14) from Sect. 2.1.2, limited to nearest neighbor-hopping with transfer integral J :

$$\hat{H}_{\text{elec}}^{\text{FE}} = \sum_n \epsilon_n a_n^\dagger a_n + \sum_n J (a_n^\dagger a_{n+1} + a_{n+1}^\dagger a_n). \quad (2.28)$$

In Eq. (2.27), \hat{H}^{ph} is the phonon Hamiltonian for the fundamental internal vibrational mode, and $\hat{H}^{\text{FE-ph}}$ couples the otherwise independent exciton and phonon systems. Accordingly, Eq. (2.26) extends the HOLSTEIN concept to CT states: \hat{H}^{CT} describes the on-site energy of a CT state arising from the transfer of an electron at site n to its nearest neighbor at site $n \pm 1$. The hopping of CT states as a whole is neglected, because the simultaneous hop of two particles is expected to be on a much smaller energy scale. $\hat{H}^{\text{CT-ph}}$ couples electron and hole to the same internal vibrational mode as the FE. Finally, $\hat{H}^{\text{FE-CT}}$ is the Hamiltonian for the mixing of FRENKEL and charge-transfer states. The treatment is still carried out in the concept of small radius exciton theories, since only nearest-neighbor interactions are discussed. The structure of $\hat{H}_{\text{Hol}}^{\text{FCT}}$ in Eq. (2.26) has also been used by HENNESSY et al. for a similar model, yet limited to the treatment of dimers only [38]. In contrast, HOFFMANN et al. treat the 1D stacks as infinite chains.

Details about the choice of basis functions and diagonalization of $\hat{H}_{\text{Hol}}^{\text{FCT}}$ are given in [8, 34], where also all technical questions are addressed in detail and the relevant fit parameters are reported. Here, we rather focus on the result, which is shown for MePTCDI in Fig. 2.5¹¹. The structure of the eigenstate spectrum is best visualized by the FRENKEL (U_{FE}^2) and the CT (U_{CTE}^2) character of the states. These are shown as shaded areas in panels (c) at the Γ -point and (e) at the band edge. The FE character at $k = 0$ determines the absorption coefficient, which agrees very well with the experiment, as can be seen from panel (b). In the rightmost diagram (f), the emission spectra from a single crystal is compared to the expected peaks of the modeled luminescence spectrum from the lowest point at $k = \pi$ back to the vibrational levels of the ground state. Again, the agreement is favorably well. In particular, the 00-transition is strictly dipole forbidden and not observed in luminescence. The indirect emission in k -space agrees with low external quantum efficiencies of a few percent, as reported by NOLLAU et al. [43].

¹¹For PTCDA, a corresponding band structure plot can be found in [34].

In contrast to the impression one might get from the illustration of the HOLSTEIN states in Fig. 2.5, the lowest absorbing state at $k = 0$ and the lowest emitting state at $k = \pi$ are discrete. The convolutions with Gaussian line shapes are for comparison purposes. For MePTCDI, the energy of the lowest state at $k = 0$ is at 2.11 eV, while for $k = \pi$ its energy is at 2.065 eV. For PTCDA, we obtain 2.22 eV vs. 2.175 eV. The difference in both cases is ≈ 45 meV. Hence, both MePTCDI and PTCDA are H-aggregates with a negative exciton dispersion dE/dk ¹². As argued in the discussion following Eq. (2.25), we expect the population created by photo-excitation at $k = 0$ to relax very rapidly to the lowest state at $k = \pi$. Throughout this thesis, we will call this process *intragrand relaxation or relaxation in k -space*.

2.3.2. Alternative models

As noted in the previous section, multiple other band structure models have been developed to explain the spectra and the energetic structure of perylene derivatives. In this section, we briefly want to comment on two of them.

MAZUR et al. [39] have proposed a three-dimensional analog of the MERRIFIELD model [44]. It contains mixing between FRENKEL and CT states and their coupling to the effective internal mode at the molecular site (i. e., the “molecular vibron”). Its primary aim is to explain the absorption and, in particular, the electroabsorption spectra of bulk PTCDA [45]. The predicted spectra agree very well with the experimental data, except for the anisotropy of the electroabsorption. This open issue, however, was attributed with good justification to the imperfectness of the samples. The 3D model lays the foundation for further application of the 1D treatment for similar systems, and the fit parameters in both cases are in reasonable agreement. One of the key statements of MAZUR et al. is the imperative role that they attribute to the charge-transfer excitons when it comes to the explanation of electroabsorption.

VRAGOVIĆ and co-workers considered a 3D model solely based on FRENKEL excitons, while neglecting any CT contributions. Phononic interaction is also limited to the case of intramolecular vibrations. The authors focus on the modeling of absorption and photoluminescence in PTCDA (α -phase). The correspondence with experimental linear absorption spectra is good. Yet, MAZUR et al. [39] have noted that the deficiencies are evident when it comes to the comparison with electroabsorption spectra in particular, which is regarded as the main evidence for the existence of CT states. As for photoluminescence (PL), KOBITSKI et al., who carried out investigations of time-resolved PL measurements of PTCDA thin films and single crystals [46, 47], claim very good agreement with the model of VRAGOVIĆ and co-workers.

In conclusion, band structure models are the only microscopic picture currently used for describing optical spectra of materials such as perylene derivatives. Despite many open questions about the precise nature and dispersion of the bands, the only properties of direct importance for the discussion in the framework of this thesis – namely a negative dispersion of the lowest band, in combination with indirectly emitting states – is accepted by all studies presented here.

¹²In Fig. 2.5 (d), we have symbolized this negative dispersion for the lowest HOLSTEIN states by a dotted line.

2.3.3. Davydov splitting and Davydov components

For later use in this thesis, we now return to the formation of excitonic bands in the framework of a 1D pure FRENKEL exciton model as in Sect. 2.1.2 and refine it for systems with $Z = 2$ molecules per unit cell. As can be seen from Figs. 2.3 and 2.4, this is the case for MePTCDI and PTCDA crystals. In complete analogy to the Hamiltonian in Eq. (2.14), we can write:

$$\hat{H}^{\text{Ex},Z} = \sum_{n\alpha} \epsilon_{n\alpha} a_{n\alpha}^\dagger a_{n\alpha} + \sum_{\substack{m\beta, n\alpha \\ m\beta \neq n\alpha}} J_{m\beta, n\alpha} a_{m\beta}^\dagger a_{n\alpha}, \quad (2.29)$$

where the summation indices α and β symbolize the translationally non-equivalent molecules A and B in the unit cell. Again, the momentum representation is better suited for finding a solution. After FOURIER-transformation of the creation and annihilation operators $a_{n\alpha}^\dagger$ and $a_{n\alpha}$, we obtain instead of Eq. (2.29):

$$\hat{H}^{\text{Ex},Z} = \sum_k \sum_{\alpha\beta} (\epsilon_{0\alpha} \delta_{\alpha\beta} + L_k^{\alpha\beta}) a_{k\alpha}^\dagger a_{k\beta}. \quad (2.30)$$

Of course, $\hat{H}^{\text{Ex},Z}$ is diagonal with respect to k , but there are still transfer elements between states α and β . Essentially, the lattice sum matrix $L_k^{\alpha\beta}$ of rank 2×2 has to be diagonalized. This leads to two solutions $\epsilon_\pm(k)$ for two excitonic bands which are split in energy. The DAVYDOV-splitting $\Delta\epsilon = |\epsilon_+ - \epsilon_-|$ is small compared to the total excitation energy, because the in-plane intermolecular coupling for a quasi-1D system is much smaller than the in-stack coupling. $\Delta\epsilon$ is also small compared to the excitonic dispersion $|\epsilon(\pi) - \epsilon(0)|$.

DAVYDOV-splitting can also be discussed in the picture of transition dipole moments. In Fig. 2.6, this is depicted for the unit cells of both MePTCDI (top panel) and PTCDA (bottom panel). The major molecular transition dipole moments along the molecular x-axis for the two molecules are denoted by \mathbf{P}_A and \mathbf{P}_B , respectively. \mathbf{P}_A and \mathbf{P}_B are the molecular transition dipole moments for the FRENKEL excitons. Superposition of \mathbf{P}_A and \mathbf{P}_B yields two mutually perpendicular transition dipole moments¹³.

$$\mathbf{P}_\pm = \frac{\mathbf{P}_A \pm \mathbf{P}_B}{\sqrt{2}}. \quad (2.31)$$

As for PTCDA, \mathbf{P}_\pm are nearly equal in size, because of the mutual orientation of the molecules in the unit cell. For later use in this thesis, we define the ratio $\xi = |\mathbf{P}_-|/|\mathbf{P}_+|$. Since $\mathbf{P}_+ \perp \mathbf{P}_-$, a polarization dependence of the absorption spectra should be observable. For MePTCDI, DAVYDOV-splitting has in fact been verified by polarized absorption measurements in highly ordered films [23]. In PTCDA, however, this was not possible, because macroscopically oriented films are not available, which is not surprising for the almost isotropic in-plane orientation of the molecules. Still, DAVYDOV-splitting was proven in PTCDA by ellipsometry on single crystals [48].

¹³More details on the geometrical aspects of the orientation of the molecules and \mathbf{P}_\pm can be found in [23]. The coupling concept is still applicable although the molecular planes are tilted with respect to the (100) plane, which cannot be clearly seen in Fig. 2.6.

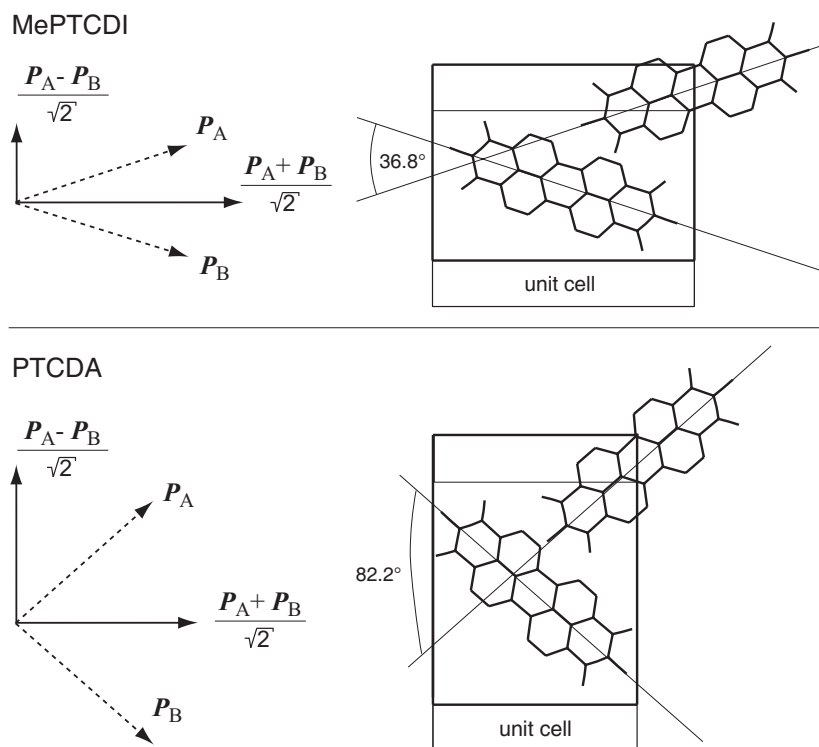


Figure 2.6.: Top: Unit cell of MePTCDI with two molecules. The major transition dipole moments for FRENKEL excitons P_A and P_B couple to form two DAVYDOV components. Bottom: The same situation, but for PTCDA. Note that since the angle is close to 90° , the DAVYDOV components are almost equal in size.

2.4. Questions of interest

In this chapter, we have outlined the electronic and related optical properties of the quasi-1D materials PTCDA and MePTCDI. Despite increasing interest in these materials in the last decade, virtually no information about the ultrafast excitonic response of these materials after photo-excitation is available¹⁴. Our particular interest lies in the exciton dynamics in the lowest excited state S_1 -manifold. We will briefly summarize the status of ultrafast measurements on MePTCDI and PTCDA, excluding the nature of photoluminescence, which is subject to a controversial debate.

Review of ultrafast measurements Canzler [35] has extensively studied MePTCDI thin films using pump-probe spectroscopy. Among many other topics, he addressed the depopulation of the lowest absorbing state at the Γ -point, extracting an upper limit of 50 fs for the life time from the decrease of the stimulated emission signal. The interpretation

¹⁴This is in surprising contrast to a variety of other vanguard materials. As prominent examples where ultrafast relaxation processes have been extensively studied, we mention here polymers [49–51], J-aggregates in solution [52, 53], or other organic molecular crystals such as oligothiophenes [54, 55] or even the 1D-stacked phthalocyanines [56, 57].

is based on an assumed absence of any coherent interaction of pump and probe pulses, which became questionable when repeating the experiment in this work (cf. Sect. 5.2.1). Moreover, CANZLER performed spectrally resolved pump-probe measurements to investigate the relaxation into the emitting state. An intraband relaxation time of about 50 fs was reported. Since the transient transmittance signal was superimposed by phononic modulations and the chirp present in the probe spectrum, a definite statement about the intraband relaxation time constant could not be made. Besides, the conclusions were based on the absence of intermediate states between absorbing and emitting states. However, this cannot be trivially derived, since transient absorption is not sensitive to specific momentum states in k -space.

INO and co-workers [58] have reported relaxation time constants for the S_1 and S_2 state of PTCDA thin films, measured by two-photon photoelectron spectroscopy (2PPE). The molecules were ionized by very intense degenerate excitation into high-energy states with a photon energy of 5 eV, far above the S_2 manifold. With 2PPE, it is not possible to distinguish different momentum states; in fact, INO et al. have not discussed their results in the framework of band structure models at all. Besides, the 2PPE experiment with fixed photon energies does not allow to derive information about higher excited states.

Open questions As seen from this short review of (ultrafast) measurements on PTCDA or MePTCDI, only a few questions are answered, while many answers are still missing. In particular, the relaxation dynamics in the lowest excited state (intraband relaxation or relaxation in k -space) in thin films is of very high importance. Excitons created by photo-excitation relax rapidly towards the surface of the Brillouin zone into the a lowest state where they recombine either by a radiative or nonradiative decay with intrinsic life times. Hence, the intermediate time window *after intraband relaxation and prior to recombination* is decisive for the “adventures” the excitons undergo during their life time. In the example of an organic solar cell, this would correspond to the time available to separate hole and electron at a heterojunction. Directly linked to this idea would be the question of how the excitons may reach such a junction, e. g., by diffusion. And if two excitons met in space during the diffusion process, would they interact?

Thus, a detailed understanding of excitonic properties is essential for all further applications. We therefore formulate the questions and topics to be addressed within this thesis:

Intraband relaxation: Is it possible to time-resolve the relaxation process in k -space, and what do we learn from it? This can be regarded as a direct continuation of the work of CANZLER [35]. We will address the important questions of the relaxation pathway, of intermediate states, of temperature and excitation dependencies. The treatment will be done on basis of the band structure model by HOFFMANN in Sect. 2.3.1.

A time resolution of about 25 fs and undistorted (unchirped) pulses are required for this experiment. This could only be achieved by the extension of the experimental setup through the integration of a new pulse shaper device. We will report on the outcome of its implementation, being an important part of this work, in Sect. 3.3.3.

Transient and nonlinear spectra: Relaxation dynamics in the excited state are to be monitored. The method of choice is excited state absorption by pump-probe spectroscopy. The interpretation of intraband relaxation is thus only reliably possible if the transitions to higher excited states are known. Hence, transient spectra of PTCDA and MePTCDI films are imperative.

Just as in the derivation of the crystal states from the molecular states in Sect. 2.1, nonlinear absorption spectra of the solid state cannot be understood without knowledge about nonlinear spectra of isolated molecules. Therefore, transient absorption spectra of MePTCDI and PTCDA monomers are mandatory.

Experiment vs. models: This thesis clearly is an experimental work. Still, it is important to discuss in what way existing model calculations can contribute to the understanding of the experimental data. Are the data in accordance with the concept of band structure models? Can quantum-chemical calculations predict transient spectra and transition dipole moments that correspond to the experimental results? If there is a disagreement, which issues should theoreticians focus on?

Exciton-exciton interaction: All previous list items consider only single excitons that do not interact. This presumption becomes questionable in pump-probe experiments, because measurements of nonlinear properties require high excitation densities. What information can we extract from intensity dependence? How do excitons interact and annihilate? On a microscopic scale, annihilation is always related to diffusion: Does the excited state dynamics allow to extract diffusion properties and diffusion constants and lengths?

In fact, annihilation at high exciton densities is of great importance for device applications: BALDO et al. have shown how exciton-exciton interaction and annihilation restrains the efficiency of triplet emitter OLED [59, 60] and that singlet-singlet annihilation is a crucial loss mechanism to be overcome in attempts towards electrically pumped organic lasers [61]. Although MePTCDI and PTCDA are indirect emitters and thus not suited for OLED, certain aspects might be of general importance.

Molecular fingerprints: Which differences are there in the relaxation behavior of PTCDA and MePTCDI?

3. Techniques of ultrafast spectroscopy

Since the excitonic relaxation processes in condensed matter happen on an extremely rapid time scale, they usually cannot be time-resolved by conventional electronic photodetectors, even though improvements have increased the time resolution of such devices down to the picosecond range [62]. The use of ultrashort laser pulses is still the only method to achieve a time resolution of a few femtoseconds. Within the framework of this thesis, the control over a reliable pulsed ultrafast laser source was a key requirement for data quality. Consequently, this chapter introduces the experimental background necessary to understand how to make, manage, manipulate, and measure ultrafast light pulses.

3.1. Pulsed light

Initially, some fundamental mathematical concepts about light pulses are recalled which are beneficial for further considerations. This short description is closely related to common textbooks on ultrafast laser science such as [62, 63]. Here, we address only the most important properties.

3.1.1. Pulse length, pulse shape, bandwidth limitation

Fundamentals

The propagation of electromagnetic waves are fully described by the time and space dependence of the electric field being related to one another via the wave equation. For our discussion, the spatial dependence of the electric field $\mathbf{E}(\mathbf{r}, t)$ can be omitted, because we are primarily interested in the temporal evolution of the laser pulse and the relation between the time and frequency domain:

$$E(t) = \frac{\mathbf{E}(\mathbf{r}, t)}{\mathbf{E}(\mathbf{r})} . \quad (3.1)$$

Even though the measured quantities are real, the discussion is facilitated by the use of a complex description. The (real) electric field $E(t)$ can thus be described as

$$E(t) = \frac{1}{2} \tilde{\mathcal{E}}(t) e^{i\Gamma(t)} + \frac{1}{2} \tilde{\mathcal{E}}^*(t) e^{-i\Gamma(t)} , \quad (3.2)$$

where $\tilde{\mathcal{E}}(t)$ is a complex envelope function, $\tilde{\mathcal{E}}^*(t)$ its complex conjugate, and $e^{\pm i\Gamma(t)}$ are fast varying phase terms with a total phase $\Gamma(t)$. As usual, the frequency spectrum $E(\omega)$

3. Techniques of ultrafast spectroscopy

is related to the electric field $E(t)$ via the FOURIER transform

$$E(\omega) = \frac{1}{\sqrt{2\pi}} \int_{-\infty}^{\infty} dt E(t) e^{-i\omega t} \quad (3.3)$$

$$= \frac{1}{2} \tilde{\mathcal{E}}(\omega - \omega_0) e^{-i\varphi(\omega - \omega_0)} + \frac{1}{2} \tilde{\mathcal{E}}^*(\omega + \omega_0) e^{-i\varphi(\omega + \omega_0)} \quad , \quad (3.4)$$

where $\tilde{\mathcal{E}}(\omega)$ is a complex amplitude. The function $\varphi(\omega)$ is called the *spectral phase*, which contains the time vs. frequency information.

It is worth mentioning that the spectrum may in principle cover negative frequencies. In most practical cases, however, the spectral amplitude $E(\omega)$ is centered around a mean frequency ω_0 , the carrier frequency, and it spans a symmetric interval $\Delta\omega$ of positive frequencies. In the time domain, this motivates to rewrite Eq. (3.2) as

$$E(t) = \frac{1}{2} \tilde{\mathcal{E}}(t) e^{i\omega_0 t} e^{-i\phi(t)} + \frac{1}{2} \tilde{\mathcal{E}}^*(t) e^{-i\omega_0 t} e^{i\phi(t)} \quad . \quad (3.5)$$

Here, $\phi(t)$ denotes the *temporal phase*, which will be called *the phase* in the following¹. It is worth mentioning that the usefulness of the separation of the carrier frequency from the envelope function is limited to cases where $\Delta\omega \ll \omega_0$. This is referred to as *slowly-varying envelope approximation (SVEA)*, which is hardly fulfilled for extremely short pulses. For instance, the period T of an electromagnetic wave with wavelength 600 nm is $T \approx 2$ fs. In case of, e. g., 5 fs-pulses, the envelope function varies on a time scale not much longer than the optical cycle, which implies that such a pulse essentially covers a considerable part of the visible spectrum. In our experiments, where a typical pulse length is of the order of 25 fs, the SVEA is well fulfilled.

Exemplary case

As indicated, pulse length and spectral width are linked to one another. In order to visualize this correlation, we consider a simple pulse with Gaussian envelope, where all the spectral components are initially in phase:

$$E(t) = \text{Re} \left(E_0 e^{i\omega_0 t} e^{-\beta t^2} \right) \quad \text{and} \quad I(t) = I_0 e^{-2\beta t^2} \quad . \quad (3.6)$$

The form factor

$$\beta = \frac{2 \ln 2}{\Delta\tau_p^2} \quad (3.7)$$

is related to the width $\Delta\tau_p$ of the pulse, which is defined as the FWHM (full width at half maximum) of the pulse intensity $I(t) = |E(t)|^2$.

For simplicity, we omit here and in the following the expression of the real part in Eq. (3.6). FOURIER transformation of Eq. (3.6) yields the spectrum

$$E(\omega) = \frac{E_0}{\sqrt{2\beta}} e^{-(\omega - \omega_0)^2 / (4\beta)} \quad \text{and} \quad I(\omega) = I_0 e^{-(\omega - \omega_0)^2 / (2\beta)} \quad . \quad (3.8)$$

¹Obviously, the decomposition of E into ω_0 and $\phi(t)$ is not unique, but commonly, as in our case, ω_0 is the carrier frequency at the pulse peak.

As can be seen from Eq. (3.8), the spectral FWHM is $\Delta\nu = \Delta\omega/(2\pi) = 2 \ln 2/(\pi \Delta\tau_p)$, and one obtains for the *time-bandwidth-product* of a pulse with Gaussian envelope:

$$\Delta\nu \Delta\tau_p = \frac{2 \ln 2}{\pi} \approx 0.4413. \quad (3.9)$$

In general, $\Delta\nu \Delta\tau_p \geq K$, where the constant K solely depends on the pulse envelope. The equality only holds if, as assumed, all spectral components are in phase. In this case, the pulse is called *bandwidth-limited* or *FOURIER-limited*, and for a given spectrum the minimum possible pulse duration can be calculated. As an example for our experiment, a bandwidth-limited 20 fs pulse, centered at 640 nm, has a FWHM of $\Delta\lambda = 30$ nm, but the complete spectrum covers almost 100 nm. The step towards shorter pulses becomes more and more difficult the shorter the pulse actually gets.

Apart from a Gaussian envelope, a hyperbolic secant-shaped (“sech²”) pulse is also of major importance, because experimentally, pulses from femtosecond lasers are very often sech-shaped. In this particular case, the time-bandwidth-product is 0.3148. Throughout this work, we have assumed Gaussian envelopes as in Eq. (3.6) because of their simplicity and the actual shape of our pulses (between Gaussian and sech²). An extensive overview of commonly used pulse shapes can be found in [62, 63].

3.1.2. Propagation of a light pulse through dispersive media

The a priori assumption of a bandwidth-limited pulse as in Eq. (3.6) is no longer fulfilled if the light pulse traverses a normal dispersive (and not absorbing) medium of a given thickness x . Because of dispersion, the different spectral components inside the envelope are separated in time. This can be accounted for by the introduction of a spectral phase factor in Eq. (3.8) in the spectral domain:

$$e^{-i\varphi(\omega)} = e^{-ik(\omega)x} \quad \text{with} \quad k = \frac{\omega n(\omega)}{c}. \quad (3.10)$$

Here, c is the velocity of light and n the refractive index. Applying the SVEA, we can expand $k(\omega)x = \varphi(\omega)$ in a TAYLOR series:

$$k(\omega)x = \sum_{m=0}^{\infty} \frac{1}{m!} \left. \frac{\partial^m k}{\partial \omega^m} \right|_{\omega_0} (\omega - \omega_0)^m x \quad (3.11)$$

If we truncate the expansion after the second derivative² and incorporate the spectral phase term into Eq. (3.8), we can analytically solve the reverse *FOURIER* transformation. We obtain for the electric field after transmission through the medium:

$$E(t) \propto E_0 \exp \left\{ i \left[\omega_0 \left(t - \frac{x}{v_\phi} \right) + c_1 \left(t - \frac{x}{v_g} \right)^2 \right] \right\} \exp \left\{ -\beta_1 \left(t - \frac{x}{v_g} \right)^2 \right\} \quad (3.12)$$

²Let k'' be the second derivative of k with respect to ω .

3. Techniques of ultrafast spectroscopy

The following abbreviations have been used in Eq. (3.12):

$$\beta_1 = \frac{\beta}{1 + 4k''^2 x^2 \beta^2} \quad v_\phi = \frac{\omega_0}{k} \quad (3.13)$$

$$c_1 = \frac{2k'' x \beta^2}{1 + 4k''^2 x^2 \beta^2} \quad v_g = \left. \frac{\partial \omega}{\partial k} \right|_{\omega_0} \quad (3.14)$$

It is worth discussing Eq. (3.12) in comparison with Eq. (3.6):

- The first term of the first exponential states that the central frequency ω_0 is delayed by an amount x/v_ϕ , where v_ϕ is the *phase velocity*. Since an absolute phase is not a measurable quantity, this delay has no effect.
- The exponent of the second exponential shows that the pulse envelope is still Gaussian. However, the center of the pulse is delayed with respect to the incident pulse by x/v_g , where v_g is the *group velocity* of the wavepacket. The form factor β_1 is smaller than β , which implies that the pulse is broadened. Comparison of Eqs. (3.7, 3.14) yields the new pulse length³:

$$\Delta\tau_{\text{out}} = \Delta\tau_{\text{in}} \sqrt{1 + 4k''^2 x^2 \left(\frac{2 \ln 2}{\Delta\tau_{\text{in}}^2} \right)^2}. \quad (3.15)$$

This means that the shorter the pulse, the more severe the influence of dispersion, and the longer the output pulse. Experimentally, it is very important to consider these effects that may be introduced by lenses or filters. From Eqs. (3.10, 3.11) it follows:

$$\frac{\partial k}{\partial \omega} = \frac{1}{c} \left(n + \omega \frac{\partial n}{\partial \omega} \right) = \frac{1}{c} \left(n - \lambda \frac{\partial n}{\partial \lambda} \right) \quad (3.16)$$

$$\frac{\partial^2 k}{\partial \omega^2} = \frac{1}{c} \left(2 \frac{\partial n}{\partial \omega} + \omega \frac{\partial^2 n}{\partial \omega^2} \right) = \frac{\lambda^3}{2\pi c^2} \frac{\partial^2 n}{\partial \lambda^2} \quad (3.17)$$

$$\frac{\partial^3 k}{\partial \omega^3} = \frac{1}{c} \left(3 \frac{\partial^2 n}{\partial \omega^2} + \omega \frac{\partial^3 n}{\partial \omega^3} \right) = -\frac{\lambda^4}{4\pi^2 c^3} \left(3 \frac{\partial^2 n}{\partial \lambda^2} + \lambda \frac{\partial^3 n}{\partial \lambda^3} \right) \quad (3.18)$$

⋮

Hence, if the derivatives of k are known, the dispersion and the pulse length after transmission through the medium can be calculated with Eq. (3.17). In particular, $k'' > 0$ for normal dispersive media in the visible range. Refractive index data can be deduced from data for optical materials and is available for a huge number of glasses (see, e. g., [64]). First- and third order derivatives are noted for use further below.

- The second term of the first exponential in Eq. (3.12) contains a phase which has a quadratic time dependence. According to our definition $\Gamma(t) = \omega_0 t - \phi(t)$ and

³Here, $\Delta\tau_p = \Delta\tau_{\text{in}}$ for the input pulse, to distinguish it from $\Delta\tau_{\text{out}}$ for the output pulse.

the SVEA, we can write the *instantaneous angular frequency*, which contains the frequency vs. time-information, as

$$\omega(t) = \frac{d\Gamma(t)}{dt} = \omega_0 - \frac{d\phi}{dt}. \quad (3.19)$$

With Eqs. (3.12, 3.14) we finally obtain:

$$\omega(t) = \omega_0 + 2c_1 \left(t - \frac{x}{v_g} \right). \quad (3.20)$$

Except for the above observation that the wavepacket is delayed, it follows from Eqs. (3.14, 3.17) with $k'' > 0$ that the frequency increases linearly with time. Therefore, the pulse is said to be linearly *positively chirped* or *up-chirped*. This means that the leading part of the pulse is more “reddish” than the trailing part, which is more “blueish”.

The linear time dependence of the temporal phase $\varphi(t)$ in Eq. (3.12) being responsible for the delay is related to the first-order derivative of $k(\omega)$ in the TAYLOR expansion in Eq. (3.12). The square time dependence of $\varphi(t)$, being responsible for the linear chirp, is related to the second derivative. For higher orders, this correspondence is equivalent. Experimentally, the time vs. frequency-information is easier to access than the frequency vs. time-information. For these reasons, the m -th order of the TAYLOR series is usually directly identified with the chirp of $(m - 1)$ -th order:

$$x \left. \frac{\partial k}{\partial \omega} \right|_{\omega_0} \longrightarrow \text{Delay (no chirp)} \quad (3.21)$$

$$x \left. \frac{\partial^2 k}{\partial \omega^2} \right|_{\omega_0} \longrightarrow \text{GVD, “Group velocity dispersion” (linear chirp)} \quad (3.22)$$

$$x \left. \frac{\partial^3 k}{\partial \omega^3} \right|_{\omega_0} \longrightarrow \text{TOD, “Third order dispersion” (quadratic chirp)} \quad (3.23)$$

⋮

With the help of Eqs. (3.16-3.18) we can then compute specific delay, linear and quadratic chirp of optical materials of a certain thickness. Table 3.1 contains some materials of importance for our experimental setup. We will make use of some data later in Sect. 3.3.3. In the context of that section, it is also useful to define the so-called *group delay* $\tau(\omega)$, i. e., the time of arrival of a certain frequency. This happens in complete analogy to Eq. (3.19) in the time-domain:

$$\tau(\omega) = \frac{\partial \varphi(\omega)}{\partial \omega} = \frac{\partial k(\omega) x}{\partial \omega}. \quad (3.24)$$

The concepts of this chapter are of fundamental importance when dealing with ultra-short pulses. Since dispersion cannot be avoided in our experiments due to lenses, filters, nonlinear crystals, etc., we will review in Sect. 3.3 various pulse compression methods to compensate for the chirp.

Table 3.1.: Specific delay, linear chirp and quadratic chirp for common materials at a wavelength of 640 nm. FS: Fused silica. Due to low dispersion and high transmission in the UV, FS glass is popular in femtosecond spectroscopy. BK7: “Borkron” glass. SF10: “Schwerflint” glass. Al₂O₃: Sapphire. TeO₂: Tellurium dioxide. “o” denotes ordinary axis and “e” extraordinary axis. Refractive index data taken from [64, 65].

Material	Delay	Linear chirp	Quadratic chirp
	$k'(\omega)$ [fs/mm]	$k''(\omega)$ [fs ² /mm]	$k'''(\omega)$ [fs ³ /mm]
FS	4981.1	25.9	28.1
BK7	5120.4	62.4	29.6
SF10	5949.1	225.5	127.5
Al ₂ O ₃ (o)	5979.7	81.1	37.9
TeO ₂ (o)	8130.0	728.0	478.1
TeO ₂ (e)	8743.3	857.5	568.3

3.2. Generation of ultrashort tunable pulses

With the fundamentals of pulse characteristics and propagation from Sect. 3.1 in mind, we now turn towards the generation of ultrashort pulses as realized in our experiment. Without going into too much detail, this section covers three major components, each of which can be regarded as a fundamental step towards the generation of femtosecond pulses over the whole visible spectrum: the fundamental laser source, the generation of white light that provides wide spectral ranges for both pump and probe pulses, and the parametric amplification of the pump-pulses. Figure 3.1 shows the complete experimental setup.

3.2.1. Ti:sapphire amplifier system

Core piece and starting point is a home-built passive KERR-lens mode-locked Ti:sapphire oscillator. Its cavity setup follows the simple arrangement with only the active laser medium and a cavity-internal prism compressor [66] (more on prism compressors in Sect. 3.3.2) to compensate for GVD. The pulsed regime is achieved by wobbling one of the prisms, which causes sufficient intensity fluctuations inside the resonator to start the mode-locking process (see, e. g., [62]). The Ti:sapphire oscillator is pumped by a commercial diode-pumped solid state laser (*Spectra-Physics*, model “Millenia V”) with intracavity second harmonic generation (SHG) running at an output power of approximately 2.3 W (cw) at 532 nm. The nearly Gaussian output pulses of the Ti:sapphire laser have an energy of 1 nJ/pulse at 795 nm with 70 fs pulse length, which corresponds to a bandwidth product of 0.465, close to the bandwidth limit of $K = 0.4413$.

The 78 MHz pulse train from this “seed” laser is injected into a commercial Ti:sapphire regenerative amplifier (*Spectra-Physics*, model “Spitfire”). By means of Pockels cells and polarization optics, a single pulse is trapped in a laser cavity and makes some 20 round trips through the laser rod before it is ejected from the resonator. The popula-

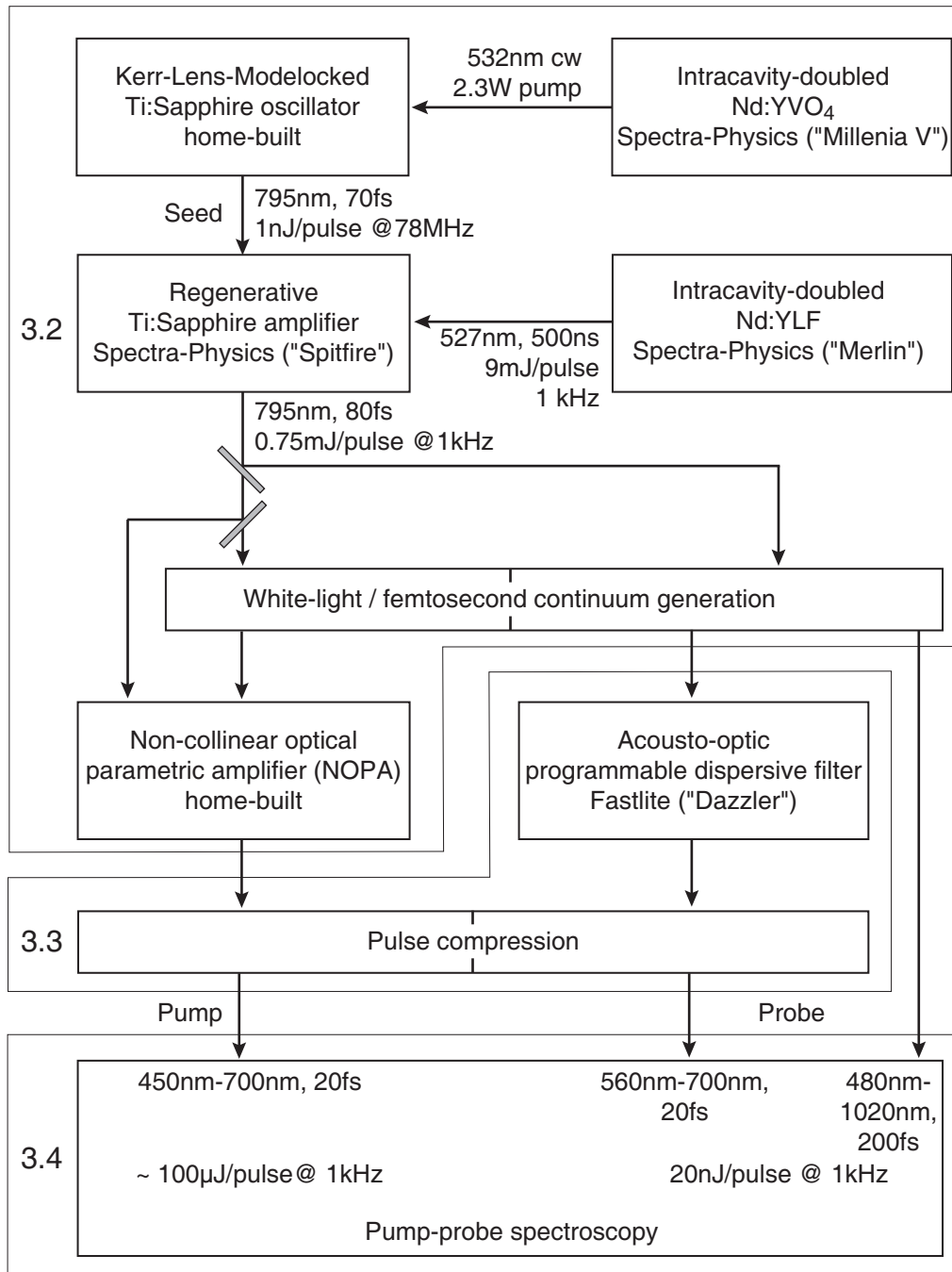


Figure 3.1.: Block diagram of the experimental setup. The fundamental light source is a femtosecond Ti:sapphire amplifier system. The high output energy per pulse is used to generate a broad spectrum from visible light to near infrared by nonlinear optical processes (white-light-generation, WLG). The pump-beam is amplified by non-collinear parametric interaction, and the probe pulses are manipulated with a pulse shaper ("Dazzler"). Pulse compressors in both beam paths allow to compensate for linear chirp. The probe beam may also be guided from the WLG directly to the experiment, providing an extraordinarily broad spectrum. The section numbers on the left hand side indicate the sections containing more detailed discussions of the framed components.

tion inversion is accomplished by synchronous pumping with a 1 kHz frequency-doubled Nd:YLF-laser (*Spectra-Physics*, model “Merlin”) at 527 nm. The final output pulses usually still have the same wavelength and bandwidth as the seed pulses, but an energy of 750 μJ /pulse, and they are thus amplified by almost six orders of magnitude. This extremely high peak intensity in the Gigawatt range facilitates nonlinear optical effects that are used for spectral broadening into the visible spectrum of the near-IR output as discussed in the next section.

3.2.2. Continuum generation

The major constraint of pulsed Ti:sapphire light sources is the fact that even with broadband mirror sets, their tunability is limited to the band width of the Ti:sapphire emission. However, nonlinear optical effects, especially *self-phase-modulation* (SPM), allow to convert the narrowband amplifier output into a continuous visible spectrum, which will be the topic of this section. The discussion of SPM is generally very complex, and here only the basic concepts are presented.

Nonlinear polarization

Firstly, we note that in case of very high light intensities the optical parameters and response of matter becomes a function of the incident light intensity. The induced macroscopic polarization \mathbf{P} of a given medium can thus be expanded in a power series expansion of higher orders of the electric field \mathbf{E} . For the i -th component P_i , we can write [67]⁴

$$P_i(\omega_p, \omega_q, \dots, t) = \sum_{n=1}^{\infty} P_i^{(n)} = \sum_{n=1}^{\infty} \underbrace{\chi_{ijk\dots}^{(n)}}_{1+n \text{ elements}}(\omega_p, \omega_q, \dots) \underbrace{E_j(\omega_p, t) E_k(\omega_q, t) \cdots}_{n \text{ components}}. \quad (3.25)$$

Here and in the following, the assumption is made that the medium reacts instantaneously to the incident electric field. In general, the nonlinear susceptibilities $\chi^{(n)}$ are tensors of $(1+n)$ -th rank. In the simple case that the $\chi^{(n)}$ are scalars – which is sufficient for the discussion to follow – the polarization can be expressed as:

$$P(t) = P(t)^{(1)} + P(t)^{(2)} + P(t)^{(3)} + \dots = \chi^{(1)} E(t) + \chi^{(2)} E(t)^2 + \chi^{(3)} E(t)^3 + \dots \quad (3.26)$$

Dependent on which order $P^{(n)}$ is responsible for a certain nonlinear effect, one talks of *n-th order effects*.

SPM and white-light-generation

The refractive index of many materials has been found to depend on the intensity of an incoming electromagnetic wave:

$$n(t) = n_0 + \frac{1}{2} n_2 I(t), \quad (3.27)$$

where n_0 is the usual weak-field refractive index and n_2 the nonlinear refractive index, which is usually positive. It can be shown that $n_2 \propto \chi^{(3)}$, i. e., the intensity-dependence of the refractive index in Eq. (3.27) is a *third-order* nonlinear optical effect [67].

⁴Eq. (3.25) obeys the summation convention for i, j, k, \dots and p, q, \dots . The electric fields involved may have different energy, as proposed.

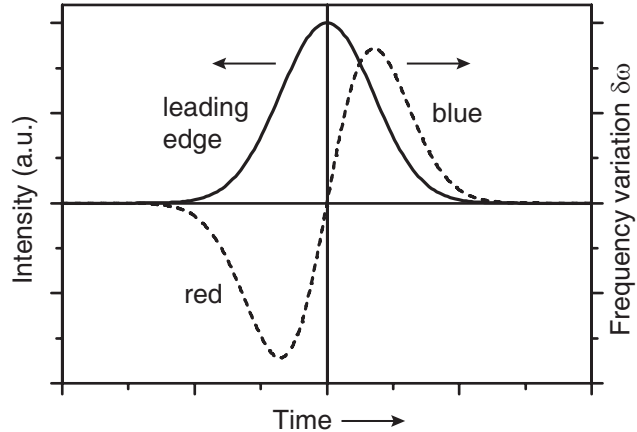


Figure 3.2.: Intensity envelope of a Gaussian light pulse. The earlier times lie on the left side of the graph. The dashed line shows the time-dependence of the central frequency for positive n_2 . $|\delta\omega|$ is maximal for the steepest slope $dI(t)/dt$.

If we consider a light pulse that traverses such a medium of thickness x , its temporal phase equals $\phi(t) = k(t)x = n(t)\omega x/c$. The instantaneous frequency as defined by Eq. (3.19) can then be written as

$$\omega(t) = \omega_0 - \frac{n_2 \omega x}{2c} \frac{dI(t)}{dt}, \quad (3.28)$$

where n_2 appears as the derivative of $n(t)$. For a Gaussian pulse envelope as used in Eq. (3.6), Eq. (3.28) becomes:

$$\omega(t) = \omega_0 + \frac{n_2 \omega x}{c} I_0 \beta t e^{-2\beta t^2}. \quad (3.29)$$

This corresponds to a frequency variation $\delta\omega(t) = \omega(t) - \omega_0$,

$$\delta\omega(t) = \frac{n_2 \omega x}{c} I_0 \beta t e^{-2\beta t^2}. \quad (3.30)$$

The concept presented here is known as *self-phase-modulation* (note that $\delta\omega(t) = -d\phi(t)/dt$) because a single pulse modifies its own characteristics by nonlinear interaction with the medium. Looking at Eq. (3.28), it can be seen that the pulse spectrum broadens with intensity. In particular, new “red” frequencies are created in the leading part of the pulse, whereas new “blue” frequencies are created in its trailing part. This behavior is sketched in Fig. 3.2, where the intensity envelope and also the symmetric spectral variation $\delta\omega$ are shown. FOURIER transformation of the self-phase-modulated electric field would then provide the new broadened spectrum.

As can be seen from Eq. (3.30), for small times $\delta\omega$ increases approximately linearly with t . In accordance with Eq. (3.20), this can be understood as linear chirp: The new frequencies are not synchronized inside the pulse envelope, and the pulse leaves the medium strongly chirped.

Besides, Eq. (3.30) demonstrates that the higher the pulse intensity, the broader the spectrum⁵. This phenomenon is called *supercontinuum generation* or *white-light-generation*. First continua have been reported already in 1970 [68], and the first femtosecond continua in the 1980’s [69]. Today, spectra with a hundreds of nanometers of

⁵Of course this statement is no longer valid when all the assumptions and simplifications made here break down.

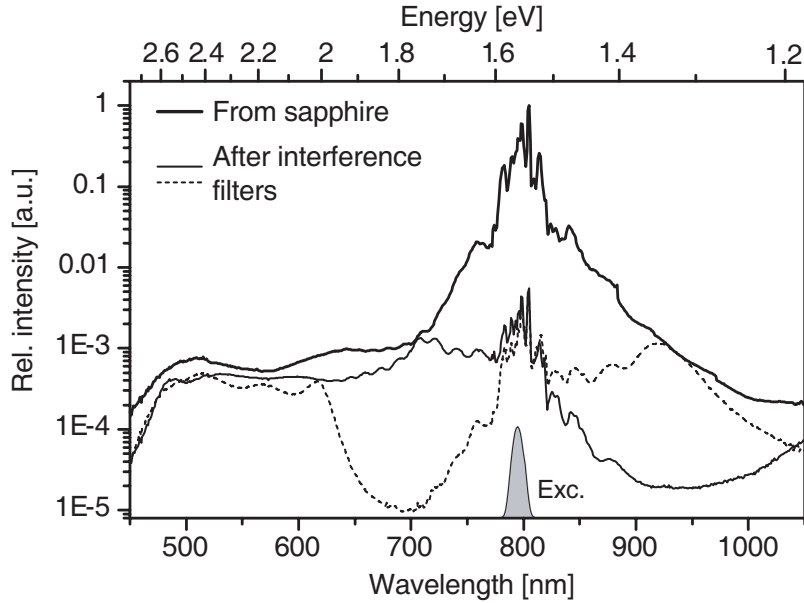


Figure 3.3.: Supercontinuum generated in a 2 mm thick sapphire disc (thick solid line). For immediate use in parametric amplification (Sect. 3.2.3) or the AOPDF pulse-shaper (Sect. 3.3.3), the flat pedestal between 500 nm and 750 nm can be used as is. For transient absorption experiments with broad spectra as presented in Chapter 4, two special interference filters (unknown manufacturer, models “WS-Filter 2252/2254”) allow to level the high dynamics around the fundamental pump from three orders of magnitude to one only (thin solid line and dashed line). Shaded area at the bottom: excitation spectrum (Ti:sapphire amplifier output).

bandwidth are routinely generated. In our experiment, this is accomplished by focusing a few $\mu\text{J}/\text{pulse}$ of the 795 nm amplifier output into high purity sapphire discs of 1–2 mm thickness. The resulting supercontinuum is shown in Fig. 3.3. The sapphire disc offers the advantages of broad spectra, high damage threshold, and ease of use.

As for the detailed mechanism and the limitations of the materials’ abilities to generate white-light continua, the discussion is still ongoing. On the one hand, more detailed examination of the $\chi^{(3)}$ –mechanism indicates that properties of the spatial beam intensity distribution must be mapped onto to the index change, which implies that in Eq. (3.27) $n(t) = n(\mathbf{r}, t)$. This leads to the formation of a KERR lens that triggers self-focusing⁶, an imperative for SPM [70, 71]. On the other hand, n_2 alone cannot account for supercontinuum generation: as an example, media such as LiF or CaF₂ feature extraordinary broad spectra in spite of a small n_2 . Additional phenomena such as multiphoton excitation and associated plasma generation in connection with chromatic dispersion [72, 73] have also been proven to accompany SPM.

⁶In fact, this is the mechanism for KERR-lens mode-locking in Ti:sapphire lasers.

3.2.3. Optical parametric amplification

Once the white-light continua have been generated, they may in principle be used directly for two-color pump-probe experiments, after possible subsequent pulse compression and shaping (Sect. 3.3). In the case of the pump beam for our experiment, however, the continuum is first amplified with a home-built *non-collinear optical parametric amplifier* (*N-OPA*).

In terms the definition in Eq. (3.25), the process of OPA can be written as [67]

$$P_i^{(2)}(\omega_i) = \sum_{j,k} \chi_{ijk}^{(2)}(\omega_i = \omega_p - \omega_s) E_j(\omega_p) E_k(\omega_s), \quad (3.31)$$

with so-called *pump*, *signal*, and *idler* photons of energy ω_p, ω_s , and ω_i , respectively. A high-energy photon with energy $\hbar\omega_p$ annihilates and amplifies a weak signal with energy $\hbar\omega_s$, whereas the idler ($\omega_i < \omega_p$) satisfies the conservation of energy and the phase-matching-condition, i. e. the conservation of momentum:

$$\omega_p = \omega_s + \omega_i \quad \text{energy conservation} \quad (3.32)$$

$$\hbar k_p = \hbar k_s + \hbar k_i \quad \text{phase-matching condition} \quad (3.33)$$

Hence, OPA is a *second-order* nonlinear process. To accomplish the phase-matching condition with sensible efficiency, typically birefringent crystals with high $\chi^{(2)}$ such as BBO (β -barium-borate, β -BaB₂O₄) are used [74]. Furthermore, the crystal is seeded with a weak signal wave of the correct frequency for high efficiency, namely the ensemble of signal waves present in the white-light continuum.

Yet, the collinear arrangement between pump and seed beam limits the temporal output and bandwidth, because after Eq. (3.33) only the phase velocities and not the group velocities are matched. This *group velocity mismatch* can be overcome by a non-collinear arrangement [75–77]. In this case, a broad spectral range can be phase-matched simultaneously, because only the projection of the idler group velocity onto the seed group velocity matters.

In our experiment, the pump beam is the second harmonic of a fraction of the amplifier output, which coincides in space and time in a 1 mm BBO crystal (type I-ooe-phaseshifting, $\theta = 32^\circ$) with the white-light continuum. The non-collinear angle between pump and seed is $\sim 4.5^\circ$. Since the incident continuum is chirped, the temporal delay between seed and pump allows to tune the maximum of the output. In combination with the tilt angle of the BBO crystal, the output is in principle tunable from 500 nm to 750 nm. For our samples, however, mainly the window between 500 nm and 600 nm is of interest. Output pulses usually have an energy of some $\mu\text{J}/\text{pulse}$ ⁷.

⁷Various methods have been employed to optimize or extend N-OPA functionality: The gain bandwidth is increased if the chirp of the white-light continuum is reduced [78, 79]. Pulse front-tilting improves spatial overlap of seed and pump and reduces the group velocity mismatch [80, 81], use of CaF₂ extends the output to the (near) UV [79, 82].

3.3. Pulse characterization and manipulation

The preceding section has discussed the generation of tunable and amplified ultrashort pulses from a “quasi-monochromatic” Ti:sapphire laser source. Yet, these pulses are usually heavily chirped and require temporal compression to rearrange the dephased frequencies inside the pulse envelope. Measurements of the pulse length are necessary to determine the success of pulse compression techniques. These concepts are subject of this section.

3.3.1. Optical correlation

At the beginning of this chapter, it was already pointed out that ultrashort pulses are the only means to measure ultrafast relaxation processes. For the same reason, of course, pulse lengths can only be determined by using other ultrashort reference pulses whose lengths define the time resolution. These all-optical techniques are generally called *cross-correlation (XC) techniques*. In case that a pulse is correlated with itself, we speak of *auto-correlation (AC)*.

For cross-correlation, the two beams overlap in space and time in a nonlinear medium with instantaneous response. The time delay τ between the pulses can be adjusted by a variable translation stage with a retroreflector in either of the beam paths that transforms spatial dependence into time information ($1 \text{ fs} \hat{=} 0.33 \mu\text{m}$). For full characterization of the output intensity I_{xc} of the nonlinear medium, all “ n -th order correlation-functions” have to be known, i. e., I_{xc} becomes [62]

$$I_{\text{xc}}(\tau) = \sum_n \int_{-\infty}^{\infty} dt \left| \chi^{(n)} \{E_1(t) + E_2(t - \tau)\}^n \right|^2, \quad (3.34)$$

with input fields $E_1(t)$ and $E_2(t - \tau)$. In practice, it is usually sufficient to stop at the second order in Eq. (3.34). For that purpose, our experiment is equipped with a crystal for sum-frequency generation (SFG) at the sample position, and the two beams impinge under a small but nonzero angle in order to generate an SFG signal in the crystal:

$$P_i^{(2)}(\omega_3) = \sum_{j,k} \chi_{ijk}^{(2)}(\omega_3 = \omega_1 + \omega_2) E_j(\omega_1) E_k(\omega_2). \quad (3.35)$$

This signal is detected in direction of the bisector of the incident beams. Eq. (3.34) then simplifies to:

$$I_{\text{xc},2}(\tau) \propto \int_{-\infty}^{\infty} dt I_1(t) I_2(t - \tau). \quad (3.36)$$

$I_{\text{xc},2}$ is called the *second-order background-free cross-correlation*. We define the cross-correlation width $\Delta\tau_{\text{xc}}$ as the FWHM of $I_{\text{xc},2}$. Practically, one pulse acts as (short) gate or reference pulse and the other one as pulse to be measured.

In the case of auto-correlations, the actual FWHM $\Delta\tau_p$ of the pulse intensity $I(t) = |E(t)|^2$ can only be extracted from $I_{\text{ac},2}$ under *assumption* of a certain envelope, because

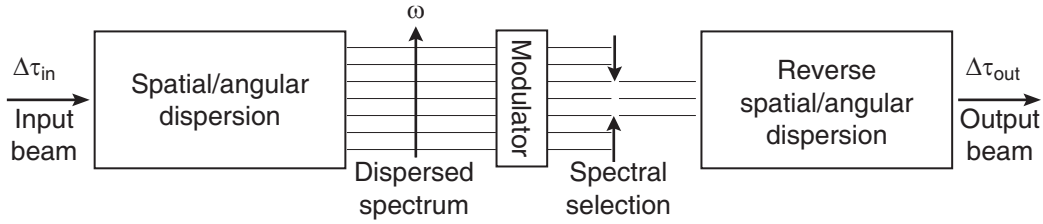


Figure 3.4.: Concept of a spatial pulse shaper. Spectral narrowing is of course optional and might be part of the modulator itself.

the pulse shape cannot be derived from $I_{ac,2}$, since the convolution Eq. (3.36) is symmetric. For a Gaussian pulse, $I_{ac,2}$ remains Gaussian and the original pulse width $\Delta\tau_p$ can be recovered from $\Delta\tau_{I_{ac,2}}$ by the relation $\Delta\tau_{I_{ac,2}} = \sqrt{2} \Delta\tau_p$ ⁸. What applies to the pulse envelope is also valid for the phase: $I_{ac,2}$ does not provide it either, and chirp-reduction is thus done solely by iterative changes of the amount of dispersive material in the beam path and comparison of pulse durations.

A key experimental issue is a sufficient conversion efficiency, motivating to use only thick crystals. Yet, thick crystals introduce additional chirp to the pulse. Moreover, their spectral acceptance bandwidth is limited [74], which mandatorily requires very thin crystals. In our experiment, we use type I-ooe-phasesmatching in a $25 \mu\text{m}$ BBO crystal cut at $\theta = 45^\circ$.

3.3.2. Pulse compression

It has been shown how the propagation through dispersive media introduce GVD, TOD, and even higher orders of chirp to a pulse. Although SPM in white-light generation creates new frequencies, the pulse is not compressed automatically. Spectral rephasing is necessary in both cases. As expected for the TAYLOR-expansion of the spectral phase in Eq. (3.11), the highest non-zero term has the most impact. To compress a pulse, it is therefore necessary to cancel GVD first, then TOD, and so on.

Various pulse compression methods have been developed, and most of them base on obvious concepts of spatial dispersion in connection with dispersive elements [83]. Figure 3.4 depicts the principle of operation: At first, the spectrum of the incident beam is spatially widened. A modulator introduces additional dispersion as a function of the angular frequency ω : For a positively chirped pulse, the red components then traverse a longer optical path than the blue components⁹. In this way, the dephasing between red and blue components inside a pulse envelope can be overcome. Afterwards, the frequencies are united in space again. Commonly used compressors of this kind are especially prism and grating compressors or programmable LCD arrays [84].

The advantage of prism compressors is the ease of use: four prisms¹⁰ (two of which are

⁸ I_1 cannot be employed because it only reveals the coherence length. For sech pulses, the ratio is $\Delta\tau_{I_{ac,2}} \approx 1.462 \Delta\tau_p$.

⁹In the frequency domain, the output spectrum is a product of the input spectrum and the modulator transfer function $M(\omega)$: $E_{out} = E_{in} \cdot M(\omega)$.

¹⁰Or two prisms in double-pass configuration.

responsible for angular dispersion, and the other two serve as the modulator) fully allow to cancel the GVD. However, as seen in Sect. 3.1.2, GVD is not independent of TOD or even higher orders or chirp. In fact, a prism compressor overcompensates the TOD, and therefore it does not allow the pulse to reach the FOURIER limit. This can only be done in combination with a grating compressor. As an example, a suitable configuration allowed to cancel dispersion up to the cubic chirp to produce 6 fs-pulses [85]. Yet, grating compressors heavily suffer from diffraction losses, produce a poor beam profile quality, and their alignment is a tedious task, especially in combination with a prism compressor. For this reason, the N-OPA output in our experiments is only compressed by means of two quartz prisms in double-pass configuration. Typical pump pulses as required for our pump-probe experiments have pulse lengths of $\sim 20\text{-}25$ fs and a bandwidth product of $\sim 0.55\text{-}0.60$.

To reduce the losses by gratings, dielectric “chirped mirrors” [86] can be employed alternatively. The penetration depth into the dielectric coating varies with frequency and allows for really custom-tailored dispersion. On the other hand, this makes the mirrors rather inflexible if the requirements change and different spectra are used. In summary, all proposed methods share the problem that the different orders of chirp cannot be changed independently of one another, so that complex and often also quite bulky combinations are required.

3.3.3. The acousto-optic programmable dispersive filter (AOPDF)

In contrast to the disadvantages of conventional pulse shapers mentioned in the previous section, a novel pulse shaping device that is part of our experimental setup can overcome these restrictions. One major task in the framework of this thesis was to integrate this *acousto-optic programmable dispersive filter (AOPDF)* [87] into the pump-probe setup and to explore its capabilities and limitations. The commercial device (*Fastlite*, model “Dazzler”) has been used successfully in many measurements presented later in this thesis. Usually, it is placed in the probe beam path (cf. Fig. 3.1) to shape the white-light continuum as necessary. Here, we shortly introduce its operating principle before we discuss an exemplary case of pulse compression.

Principle of operation

The AOPDF has been proposed by TOURNOIS [88] and is based on *collinear acousto-optic interaction*. Earlier acousto-optic transverse deflectors have already been used before [89] for pulse-shaping. At a glance, the special advantages of the AOPDF are as follows:

- It has the ability for simultaneous control of spectral envelope *and* spectral phase that allows (nearly) arbitrary shaping.
- In contrast to the above solutions, the user can access and modify the spectral phase up to the cubic chirp *separately* (FOD $\hat{=}$ “fourth order dispersion”, (cf. Eq. (3.21f.)). All control is done via a computer interface.
- The device needs not be placed in the FOURIER plane of the dispersion line as the modulator in Fig. 3.4.

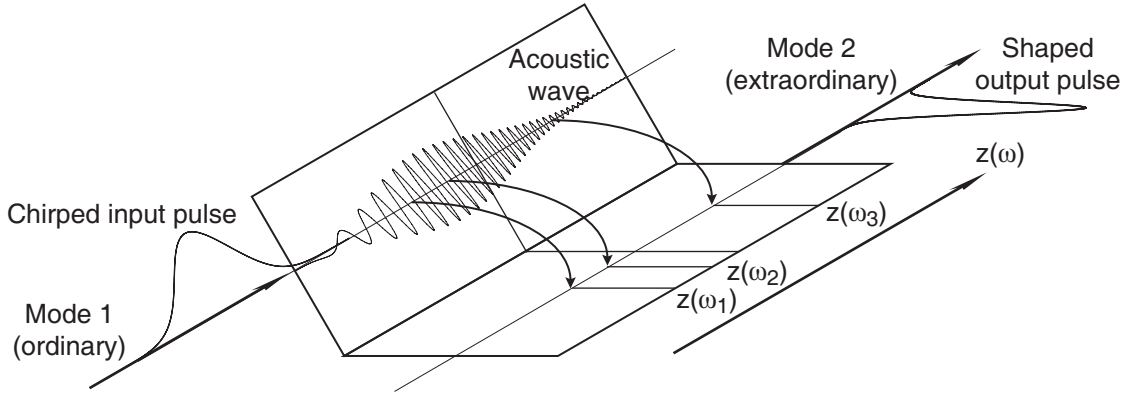


Figure 3.5.: Principle of operation of the AOPDF (after [90]): different frequencies ω_i of the input pulse interact with the ultrasonic wave at well-defined positions $z(\omega_i)$ inside the active medium and are diffracted from the ordinary to the extraordinary axis. With a custom-tailored acoustic wave, it becomes possible to rephase the spectral components with an arbitrary phase pattern.

- The dimensions of the active unit are very compact ($2'' \times 3''$), which facilitates integration into an optical setup.

Especially the first two points are of utmost importance and make the “Dazzler” a very flexible and powerful tool. Figure 3.5 depicts the basic layout and the operating principle, which has been described in detail in [88, 90, 91]: The significant part is an active medium. This is a birefringent crystal (TeO_2) of length L in which the optical wave interacts with an ultrasonic wave that propagates into the same direction. The ultrasonic wave is launched by a piezoelectric transducer attached to the crystal. The light pulses impinge along the ordinary axis of the birefringent medium. It is well known that the ordinary and extraordinary optical modes can be coupled efficiently by acousto-optical interaction [92]. The phase-matching condition in this case reads:

$$\hbar k_e(\omega) = \hbar k_o(\omega) + \hbar K(z(\omega)) . \quad (3.37)$$

Here, the k_i are the wave vectors along the (extra-)ordinary axes, K is the wave vector of the acoustic wave, and z the propagation direction. If K is monotonic, there is a distinct position $z(\omega)$ for every angular frequency ω where energy can be transferred from the ordinary to the extraordinary mode efficiently. The respective spectral component then travels $L - z(\omega)$ on the extraordinary axis. Because the phase and group velocities differ in both modes, each frequency will see a different time delay which depends on the shape of the acoustic wave. Consequently, the additional (spectral) phase imposed by the AOPDF as a function of ω can be written as

$$\varphi_{\text{AOPDF}}(\omega) = k(\omega) L = k_o(\omega) z(\omega) + k_e(\omega) (L - z(\omega)) + \psi(z(\omega)) , \quad (3.38)$$

where $\psi(z(\omega))$ is the acoustic phase.

Going back into the definition of the spectral phase in Eqs. (3.10, 3.11), we see that the phase is additive. Hence, we can compensate for the chirp of our input pulse if we

3. Techniques of ultrafast spectroscopy

zero the spectral phase:

$$\varphi_{\text{final}} = \varphi_{\text{initial}} + \varphi_{\text{AOPDF}} = 0. \quad (3.39)$$

If we can expand $\varphi_{\text{AOPDF}}(\omega)$ in a power series, this condition is fulfilled if all its coefficients are just the opposite of the coefficients of the FOURIER series for the spectral phase, i. e.,

$$\varphi^{(n)} := \left. \frac{\partial^n \varphi_{\text{AOPDF}}}{\partial \omega^n} \right|_{\omega_0} = -x \left. \frac{\partial^n k}{\partial \omega^n} \right|_{\omega_0} \quad \forall \quad n (\geq 2), \quad (3.40)$$

where the definition of (3.11f.) has been used¹¹. One of the key advantages of the AOPDF is that these coefficients $\varphi^{(n)}$ are accessible via the computer interface directly (up to the cubic chirp). Once the necessary coefficients to zero φ_{final} have been determined, the shape of the ultrasonic waveform $K(z(\omega))$ is calculated by the ‘‘Dazzler’’ software. The acoustic wave in the device can be launched by the operator upon request and runs in loop mode. The determination of the parameters for a particular experimental configuration is described further below.

Besides the phase, the AOPDF can also shape the amplitude of the spectrum: The diffraction efficiency from the ordinary to the extraordinary mode is defined by the power of the acoustic wave $S(t)$ at position $z(\omega)$. More precisely, the output spectrum is proportional to the product of the input spectrum (which the AOPDF assumes to be perfectly flat) with the spectral shape of the acoustic wave, $S(\alpha\omega)$:

$$E_{\text{out}}(\omega) = E_{\text{in}}(\omega) \cdot S(\alpha\omega). \quad (3.41)$$

Here, α is the ratio of the speed of sound to the speed of light inside the medium. In practice, however, the short-wavelength pedestal of the supercontinuum in Fig. 3.3 is not perfectly flat, which results in deviations from the desired spectral amplitude. In terms of pulse envelopes, this imperfectness eventually limits the minimum achievable bandwidth product in case of an asymmetric spectrum¹². Still, the ability to attenuate the power arbitrarily is handy and makes neutral density filters for attenuation dispensable.

Implementation and exploration

In our experimental setup, the common task for the AOPDF is to compensate for chirp introduced by dispersive elements and to provide custom-tailored ultrashort pulses with a flat spectral (and optical) phase *at the sample position*. If additional material like filters, waveplates, cryostat windows, or similar, are inserted in the beam path, the phase needs to be readjusted.

As already indicated in Sect. 3.1.2, the spectral phase is easier to access than the temporal phase. It can be determined by time-resolved optical gating [94]: One after another, spectral slices of the AOPDF output of about 6 nm width are cross-correlated in the BBO SFG crystal as described in Sect. 3.3.1. A N-OPA-pulse with about 22 fs pulse length, centered around 570 nm (as used as pump pulse in the experiment), serves as reference pulse. The maxima of the cross-correlations result in a representation for

¹¹Remember that only orders $n \geq 2$ are really relevant.

¹²Real-time deconvolution in loop mode with adjustable parameters would be desirable. Currently, no plans to implement this feature exist [93].

the group delay (cf. Eq. (3.24)) $\tau(\omega) = d\varphi(\omega) / d\omega$, the derivative of the spectral phase. If we fit a power series to the group delay,

$$\tau(\omega) = \sum_n a_n(\omega - \omega_0)^n, \quad (3.42)$$

the spectral phase $\varphi(\omega)$ can be recovered by the integration of Eq. (3.42):

$$\varphi(\omega) = \int d\omega \sum_n a_n(\omega - \omega_0)^n. \quad (3.43)$$

Comparison of Eq. (3.43) with Eq. (3.40) finally yields the representation of coefficients of the power series representation of the spectral phase:

$$\varphi^{(n)} = (n - 1)! a_{n-1}. \quad (3.44)$$

With this procedure, the operator obtains the coefficients $-\varphi^{(n)}$ to feed into the software of the AOPDF controller to eliminate the spectral phase as in Eq. (3.39).

Figure 3.6 shows examples of the effectiveness of the AOPDF. Before its implementation, a conventional quartz prism compressor in double-pass configurations was used. The group delay over the relevant interval amounted up to 200 fs (with a TOD of $\sim 3 \times 10^3 \text{ fs}^2$) [35]. With the AOPDF, the remaining group delay throughout the same interval was on the order of only 25 fs after correction, which is a clear improvement. Furthermore, the phase does not need to be readjusted if the spectrum is changed, in contrast to the prism compressor, which is only optimized for one center frequency ω_0 . On a day-to-day basis, the AOPDF operation is uncritical and does not require further adjustment. This is advantageous because the phase determination is a time-consuming process.

Despite all obvious benefits, the user has to do the splits to achieve minimum pulse lengths, because of *self-dispersion* of the AOPDF. As can be seen from Table 3.1, the active unit (TeO_2) introduces an extraordinary large chirp. The 25 mm length of the TeO_2 -crystal results in a GVD of $\sim 2 \times 10^4 \text{ fs}^2$, exceeding the maximum possible compensation of 10^4 fs^2 of the device. The only way to overcome this limitation with a reasonable optical layout is to use a prism compressor of highly dispersive ‘‘Schwerflint’’ glass (SF10). Table 3.1 indicates that in order to compensate 10^4 fs^2 , more than 40 mm of SF10 are necessary¹³.

Still, the finite prism size reduces the available theoretical bandwidth to about 120 nm, since a part of the dispersed spectrum misses the second prism. As seen in Sect. 3.1, the 120 nm convert to a $\Delta\tau_p$ of 5 fs. Owing to the limited length of the acousto-optic interaction, however, the ultrasonic wave does not fit into the active unit in this particular case, so that the phase-matching condition is not fulfilled. In reality, the available bandwidth amounts to 35 nm (Gaussian FWHM), yielding a $\Delta\tau_{p,\min}$ of ~ 15 fs, which has been realized in test runs in our laboratory.

Recently, a new design of the AOPDF has been presented that allows direct shaping of a N-OPA output [95] where the TeO_2 -crystal is cut differently. This enables the device

¹³The prism distance for our SF10 compressor is 70 cm only. For BK7, about 5 m would be required.

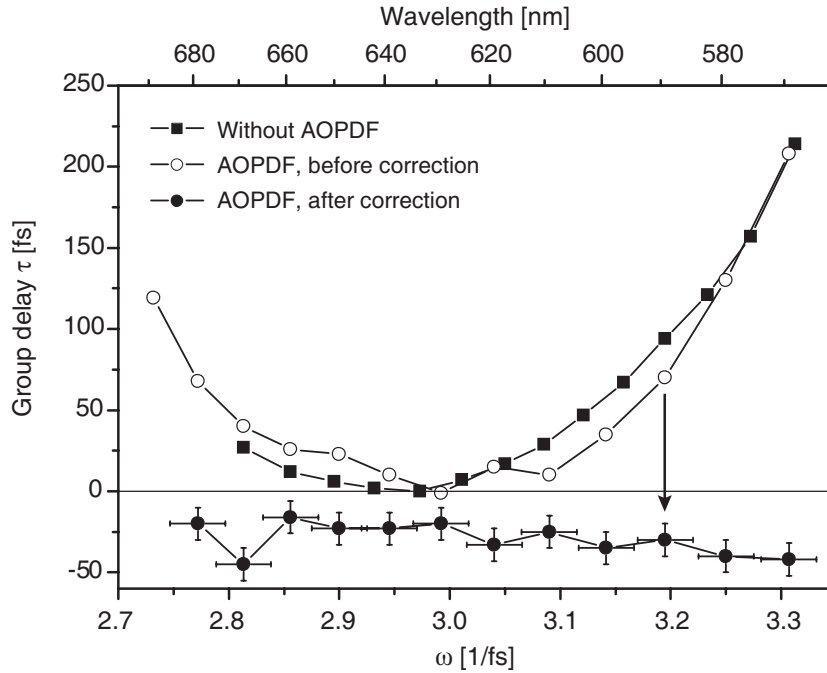


Figure 3.6.: Minimum group delay for two different configurations: Solid squares are without AOPDF (from [35]), but with a conventional prism compressor. Open circles are with AOPDF after major changes in the previously optimized optical layout, but without phase correction. Solid circles corresponds to the open circles' layout, after phase correction with the AOPDF (shifted by -25 fs for clarity). Error bars in result from the finite length of the reference pulse (vertical) and the uncertainty in the phase-matching angle (horizontal) for SFG.

to fully compensate for its own chirp, and there is no need for an additional prism compressor. Unfortunately, it is not possible to upgrade from the existing version by a mere replacement of the crystal unit [93].

3.4. Spectroscopic methods

3.4.1. Transient transmittance spectroscopy

Our primary interest lies in the relaxation of populations of the optically excited states in our systems on a femtosecond and picosecond time scale. These investigations are addressed by the technique of nonlinear *transient absorption spectroscopy* (TA) with ultrashort laser pulses. TA is a so-called *pump-probe technique* in which the sample is perturbed at $t = 0$ by an intense pump pulse $E_{\text{pu}}(\mathbf{k}_1, t)$ that propagates into direction \mathbf{k}_1 . A macroscopic polarization $\mathbf{P}(t)$ is created that decays with time. The delayed (comparatively weak) probe pulse $E_{\text{pr}}(\mathbf{k}_2, t)$ at $t = \tau$ with propagation direction \mathbf{k}_2 interrogates the dynamics of the non-equilibrium state. The pump-probe signal can then

generally be described as (e. g. [96])

$$I_{\text{pp}}(\tau) = 2 \text{Im} \omega_{\text{pr}} \int_{-\infty}^{\infty} dt E_{\text{pr}}(t) P^{(3)*}(t), \quad (3.45)$$

i. e. the time-dependent response of the system enters the formulation through an induced *third-order* polarization effect or $\chi^{(3)}$ -*effect*. In the case of the impulsive limit, where $\mathbf{E}_{\text{pr}}(\mathbf{k}_2, t) = \delta(\tau)$, Eq. (3.45) becomes:

$$I_{\text{pp}}(\tau) \propto \text{Im} P^{(3)*}(\tau). \quad (3.46)$$

It has been shown that the third-order polarization $P^{(3)}$ can be described as [97]

$$P^{(3)}(\mathbf{k}_2) = \chi^{(3)} E_{\text{pu}}(\mathbf{k}_1) E_{\text{pu}}(\mathbf{k}_1) E_{\text{pr}}(\mathbf{k}_2), \quad (3.47)$$

which means that the pump pulse creates a third-order polarization which radiates into the direction \mathbf{k}_2 of the probe beam¹⁴.

The variation of intensity in probe direction motivates to measure the pump-probe signal as pump-induced transmission change of the probe beam:

$$\frac{\Delta T}{T} = \frac{T_{\text{pumped}} - T_0}{T_0}, \quad (3.48)$$

where T_{pumped} is the transmission of the probe beam in presence of the pump and T_0 the transmission of the unpumped sample. In this context, it is worth mentioning that although we might talk of transient absorption, we always measure it as transient transmittance or differential transmission $\Delta T/T$. ΔT can be measured directly if a reference beam is employed that balances the probe beam in the unpumped state. For this purpose, the reference beam can be attenuated with a variable neutral density filter. Since the reference is only a power calibration, it need not traverse the sample. T_0 can be determined by blocking both the reference and the pump beam. The general concept is depicted in the schematic of the experiment in Fig. 3.7.

It can be shown that as a first approximation the differential transmission is proportional to the pump intensity:

$$\frac{\Delta T}{T} \approx \frac{2\chi^{(3)}}{\chi^{(1)}} I_{\text{pu}}. \quad (3.49)$$

¹⁴At this point, it is very important to note that this is only a very rudimentary discussion. The concept that I_{pp} is the diffraction of the pump beam in the probe direction is in fact general. A more profound description of the pump-probe signal should be made completely in the density-matrix formalism which includes both coherent (non-diagonal elements) and incoherent (diagonal elements) processes. If the time scale of the experiment is long compared to the excitonic dephasing time, only incoherent processes are measured. Four-wave-mixing experiments in the work of CANZLER [35] showed that the excitonic dephasing time T_2 was found to be ~ 20 fs, which is just below our time resolution. Therefore, we only discuss the *incoherent* processes, i. e., the dynamics of excited state *populations* and their lifetimes T_1 . In density-matrix formalism, this means that the off-diagonal elements of the density operator can be ignored.

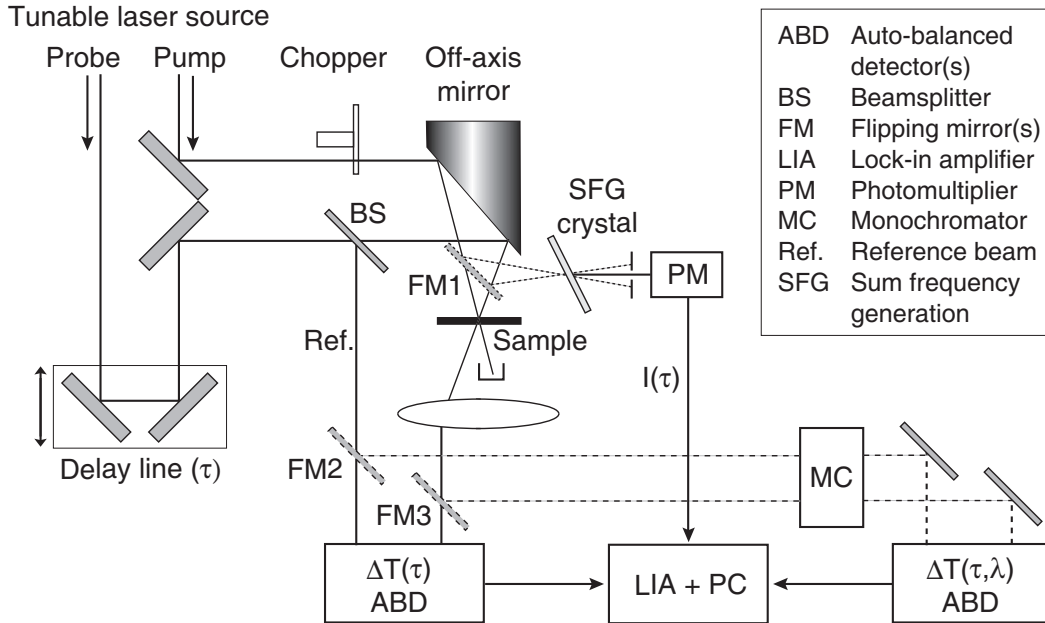


Figure 3.7.: Schematic of the experimental setup (detail of Fig. 3.1). Pump-beam: from N-OPA. Probe beam: unshaped white light continuum (Sect. 3.2.2) or shaped with the AOPDF (Sect. 3.3.3). Detection is differential: the probe beam and a reference beam illuminate two SI-PIN photodiodes (*Hamamatsu*, type “G-7830”), and only the difference signal ΔT is output and amplified (*HMS Elektronik*, model “564”) before the lock-in amplifier input (*Stanford Research Systems*, model “SR 850”). Flipping mirrors FM2 and FM3 allow to send the probe and reference beams through a monochromator (*Acton research*, model “Spectra Pro 750”) for spectral dispersion and an energy-resolved pump-probe signal. Flipping mirror FM1 is used for auto- and cross-correlation measurements (cf. Sect. 3.3.1) at the sample position. The SFG signal is detected with a photomultiplier (*Hamamatsu*, type “R 212”).

When it comes to the determination and comparison of absolute exciton densities, this relation is of importance. On the one hand, the exciton density is proportional to the pump intensity I_{pu} . On the other hand, $\Delta T/T$ is related to the exciton density via a detection efficiency factor η . This mutual dependence allows to control if a signal contribution stems from the correct nonlinear effect.

Actual exciton densities can be computed by the following relation:

$$n_0 = \frac{\lambda_0}{hc} \frac{1}{A} \frac{P_{\text{cw}}}{\nu_{\text{Rep}}} \alpha \quad (3.50)$$

Here, λ_0 is the center wavelength of the pulse spectrum, A the size of the focal spot on the sample, P_{cw} the time-integrated (cw equivalent) beam power, ν_{Rep} the laser repetition frequency ($P_{\text{cw}}/\nu_{\text{Rep}}$ the energy per pulse), and α the absorption coefficient of the sample for λ_0 . Eq. (3.50) is valid for linear absorption. Due to the small sample thickness of a few nanometers, we consider homogenous excitation along the beam path. The focal size A has been estimated to be circular with $\sim 50 \mu\text{m}$ in diameter, measured by the FWHM of a Gaussian spot.

Because the changes in absorption (or transmission) are small (down to 10^{-5}) the differential detection is used in combination with phase-sensitive detection. This means that the periodic pump-probe signal, whose frequency is determined by the 1 kHz repetition rate of the laser system, is filtered by means of a lock-in amplifier to increase the signal-to-noise ratio. A laser-synchronized chopper in the pump beam blocks every other pump pulse, so that the detection frequency is half the laser frequency.

3.4.2. CW absorption and emission, time-resolved luminescence

In addition to the pump-probe setup, other experimental units have been employed for sample characterization and for measurements of data presented in the framework of this thesis.

- CW absorption spectra were measured by a commercial spectrophotometer (*Shimadzu*, model “UV 3100”).
- A commercial fluorescence spectrometer (*SPEX*, model “FluoroMax”) was used for measurements of CW emission and fluorescence excitation spectra.
- Time-resolved luminescence measurements were performed with a streak camera (*Hamamatsu*, model “C4880”). In the time-resolved luminescence measurements, the samples were excited with the second harmonic of the 880 nm output of a commercial Ti:sapphire-laser (*Spectra-Physics*, model “Tsunami”, ps-version) which was pumped by an Ar⁺- laser (*Spectra-Physics*, model “BeamLok 2060”). Time resolution for this setup was 10 ps, limited by the synchronization jitter of the laser pulses with the detection system.

Whenever required, all these devices have been corrected for spectral dependencies, i. e., for the instrument response and detector efficiencies. For the discussion of luminescence and pump-probe anisotropies, it was necessary to characterize the intrinsic anisotropy of the samples, which was done by polarization-dependent detection. To account for the polarization dependence of the instruments (in particular, “FluoroMax” and streak camera setup), we have employed an ideal unpolarized halogen light source (*Mikropack*, model “HL 2000”) and a scattering standard (*Labsphere*, model “SRS-99-010”).

4. Transient absorption spectra of PTCDA and MePTCDI matrix-isolated systems and thin films

This chapter presents the transient absorption spectra of MePTCDI and PTCDA. In the introduction of our model systems in Chapter 2, we already pointed out that the understanding of single or isolated molecules are key prerequisites for the clarification of crystalline material. In our time-resolved transient absorption (TA) experiments, the population dynamics of the lowest excited exciton state S_1 are of interest¹, monitored by the probe beam, exciting the sample into unknown higher states S_n . Knowledge about the energy of these excited states S_n and the allowed optical transitions $S_1 \rightarrow S_n$ (or also $S_0 \rightarrow S_n$) and their polarization is crucial for the interpretation of experimental results. For this reason, we first discuss the properties of matrix-isolated molecules of MePTCDI and PTCDA in Sect. 4.2. The advantage of single molecules lies with the possibility to compare experimental results with quantum-chemical computational methods providing excited states energies and transition dipole moments between them.

For the remainder of this thesis, we then turn our attention towards the investigations of thin polycrystalline films. As for this chapter, of course, the focus is on transient spectra of thin polycrystalline films in Sect. 4.3. Predictions of quantum-chemical calculations for such complex systems are limited. Yet, dimer calculations will help us to understand qualitatively the changes from isolated molecules to the thin film.

In order to have all characteristics of the samples at hand before discussing the pump-probe results, the following section presents linear cw absorption and emission spectra of the samples that have been used throughout this work. We elaborate on their preparation, and, in the case of the matrix systems, their degree of monomericity, in comparison with thin film spectra and spectra of molecules in solution.

4.1. Linear absorption and emission spectra

4.1.1. Matrix-isolated molecules

Transient pump-probe spectroscopy measures nonlinear properties ($\chi^{(3)}$ -effects) of the sample. As indicated in the preceding chapter, only the excitation with a high pulse energy deposited in a strongly confined focus allows to access higher orders of the nonlinear polarization and reveals nonlinearities of the sample, provided that the concentration of molecules in the focus is high enough. Of course, the easiest and most commonly applied way to study isolated molecules is in solution. In case of the perylene derivatives MePTCDI and PTCDA, however, the particular challenge is their very poor solubility.

¹Recall that S_1 denotes the lowest excited exciton state, including its vibrational progression, which we will not consider in this work. This also applies to the other S_n .

For example, BULOVIĆ et al. [37] showed that for solutions of PTCDA in dimethyl sulfoxide (DMSO), aggregate formation occurs already at concentrations less than $1 \mu\text{mol/l}$. The same holds for MePTCDI: monomer-like behavior was only reported for typical concentrations of smaller than $1 \mu\text{mol/l}$ by HOFFMANN et al. [23].

For a $1 \mu\text{M}$ -solution, the mean molecular distance in 3D amounts to $\sim 110 \text{ nm}$, which results in molecular densities so small that measurements of nonlinear properties are extremely difficult or even impossible. One way to overcome this limitation is to add suitable functional substituents to increase their solubility. In fact, OLIVEIRA et al. [98, 99] have reported on successful measurements of two-photon absorption cross sections of several perylene derivatives in solution², with typical concentrations of about 10^{-3} mol/l . Of course, any functional group attached to the molecule alters its character: electronic and therefore also optical properties are modified.

Another way to increase the concentration and still to avoid aggregation is to embed the molecules into a rigid matrix without any intermediate solution step. This new technique has been introduced by FRÖB and co-workers. Our samples were used by courtesy of FRÖB et al., who produced such “solid solutions”, where the dye was co-evaporated onto room-temperature glass substrates under high vacuum (10^{-6} mbar) together with silicon oxide (SiO_2) acting as the matrix. The dyes, purified by gradient sublimation, were evaporated from indirectly heated ceramic crucibles, and SiO_2 was deposited by electron beam evaporation. The total sample thicknesses amounted to $1.65 \mu\text{m}$ with a dye volume concentration of 1%. This concentration results in an average molecular distance of about 3 nm , which is only 4.5 times larger than the mean distance in a polycrystalline film, and 9 times larger than the distance of adjacent molecules in the stacking direction [14, 24]. In comparison to a $1 \mu\text{mol/l}$ -solution, the volume density is thus increased by about 5×10^4 , which is sufficient for pump-probe experiments.

4.1.2. Thin polycrystalline films and monomers in solution

Like the matrix-isolated systems, the thin films have been produced by physical vapor deposition. Earlier works [100, 101] and routine measurements with atomic force microscopy (AFM) have proven that under the given conditions, the films are polycrystalline, with the size of the crystallites being on the order of $50\text{-}100 \text{ nm}$. As substrates for the films, *c*-oriented sapphire discs have been used because of their high thermal conductivity ($1.6 \times 10^4 \text{ W(mK)}^{-1}$ at 10 K [102]), an advantage that becomes important during measurements at helium temperature presented in the following chapters. Sample thicknesses ($\sim 35 \text{ nm}$) were estimated from cw absorption spectra, in combination with absolute values of the absorption coefficients α as published for MePTCDI [103] and PTCDA [104].

Linear absorption and emission spectra of dye molecules in solution are shown for comparison with the spectra of the matrix-isolated systems. In order to obtain well-defined concentrations, the material was dissolved from vapor-deposited thin films as described in [23].

²(*n*-butylimido) perylene (BuPTCD), bis-(benzimidazo) perylene (AzoPTCD), bis-(benzimidazo) thiopyrene (Monothio BZP), bis-(phenethylimido) and *n*-pentylimido-benzimidazo perylene (PAzoPTCD)

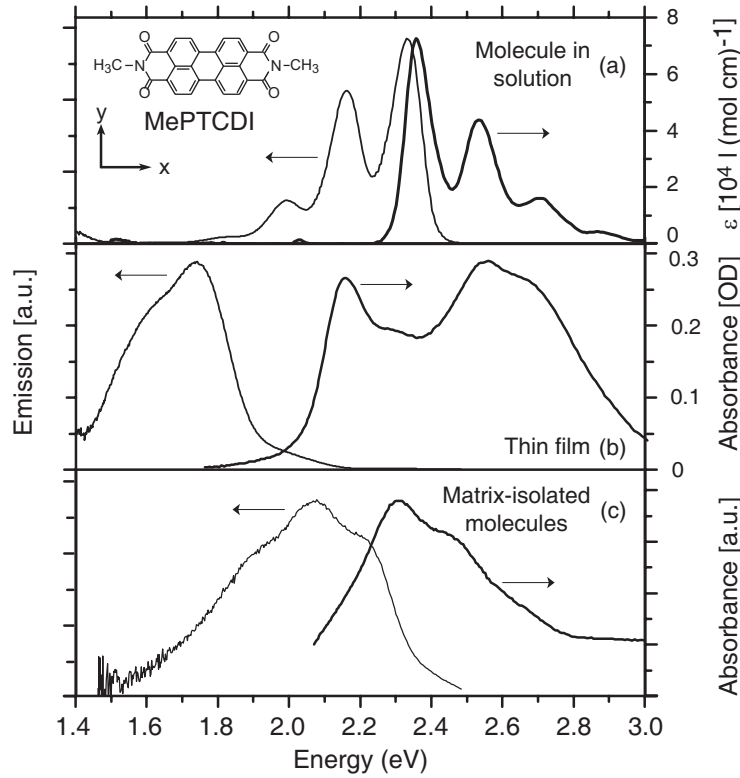


Figure 4.1.: Absorption and emission spectra of MePTCDI solution, thin film, and the matrix-isolated samples in comparison. Thick lines in all panels show the absorbance: (a) molar extinction coefficient ε of MePTCDI in chloroform ($0.3 \mu\text{mol/l}$) [23], (b) absorbance of a thin polycrystalline film ($\sim 35 \text{ nm}$ on sapphire), (c) 1% MePTCDI/SiO₂ matrix sample, measured as cw fluorescence excitation. Thin lines are normalized emission spectra (in (a), MePTCDI dissolved in chloroform ($0.4 \mu\text{mol/l}$)). All data were taken at room temperature. The inset depicts the molecular structure and the molecular coordinate system.

4.1.3. Comparison of linear spectra

Figure 4.1 shows the linear absorption and emission spectra of all three MePTCDI samples at a glance. Thick lines are absorption spectra and thin lines emission spectra. Emission spectra have been measured as photons per time and wavelength interval $I(\lambda) d\lambda$ and have been converted to illustrate *photons per time and frequency interval* $I(\nu) d\nu$ [105]:

$$I(\nu) d\nu \propto I(\lambda) \frac{1}{\nu^2} . \quad (4.1)$$

The range 2.2–3.0 eV for the molecule in solution is referred to as S_1 manifold, and it has been well investigated theoretically [27–30] for the case of the PTCDA molecule. The transition dipole for the $S_0 \rightarrow S_1$ absorption was found to be oriented along the long axis of the molecule, which in our coordinate system corresponds to the x-axis (inset in Fig. 4.1). The vibrational progression of the absorbance in (a) exhibits three distinct peaks with separations of 170 meV, which are often treated as one effective internal vi-

brational mode [38], and they can be explained by an ensemble of broadened vibrational substructures [29, 33, 106].

Since the small signal was disturbed by thin-film interferences from the SiO_2 matrix, the absorbance of the matrix-isolated sample was measured as fluorescence excitation. For MePTCDI in Fig. 4.1 (c), the fluorescence excitation clearly resembles the absorption spectrum of the molecule in solution, while it differs enormously from the thin film spectrum. In particular, its peak at 2.30 eV and the shoulder at 2.47 eV are also 170 meV apart. Similarly, the emission spectrum also shows a substructure pointing towards single molecule behavior with the $S_{1,0} \rightarrow S_{0,0}$ transition³ lying at 2.21 eV and a $S_{1,0} \rightarrow S_{0,1}$ transition at 2.07 eV. The spectral broadening and the moderate energetic shift of 60 meV of the highest peak in comparison with the monomer in solution may be caused by interaction with the solvent environment⁴.

As for the absorption and emission spectra of the PTCDA matrix system in Fig. 4.2 (c), these distinct features are still visible, but much less pronounced. The fluorescence excitation now peaks at 2.39 eV, and a small shoulder at 2.54 eV can be just be recognized. For the emission, the $S_{1,0} \rightarrow S_{0,0}$ transition now appears at 2.29 eV and the $S_{1,0} \rightarrow S_{0,1}$ transition at 2.14 eV, and the relative separations of 150 meV are still in reasonable accordance with the values for the molecules in solution. The broadened shape might be ascribed to *beginning aggregation*. Still, the shape is obviously much closer to the solvent spectrum than to the thin film spectrum. PROEHL et al. [107] have demonstrated in OMBE-grown films that already the in-stack interaction of two molecules leads to absorption spectra similar to the film spectrum. A similar conclusion has been drawn by WEWER et al. [33], who have shown that already small oligomers of MePTCDI and PTCDA in helium nanodroplets alter the spectrum towards film spectra. Obviously, our PTCDA/ SiO_2 -samples predominantly exhibit monomer spectra, and we thus conclude that the monomer character predominates.

4.2. Transient absorption spectra of matrix-isolated systems

We now turn to the presentation of the transient spectra, which have been recorded by spectrally resolving the probe beam spectrum behind the sample with a monochromator (cf. Fig. 3.7). For the probe beam spectrum, the complete white light continuum (range 1.20–2.60 eV) as shown in Fig. 3.3 has been employed, without any subsequent compensation of group velocity dispersion. As a consequence of the chirp, the group delay, i. e., the time of arrival $\tau_0(E)$ for the separate spectral components, is not constant, which results in a distorted spectrum because different spectral components are probed at different time delays.

For this reason, we have initially recorded spectrally resolved TA signals as a function of time for several selected probe energies. Three representative traces from a 1% MePTCDI/ SiO_2 sample are depicted in Fig. 4.3.

³ $S_{m,n}$ denotes the n -th vibrational level of the m -th electronic state.

⁴In fact, WEWER et al. [32, 33], who measured high-resolution absorption spectra of MePTCDI and PTCDA molecules in a weakly perturbing helium nanodroplet matrix, have underlined that solvent interaction may dramatically shift solution spectra by more than ~ 200 meV. However, an extended discussion of solvent interaction is beyond the scope of this thesis.

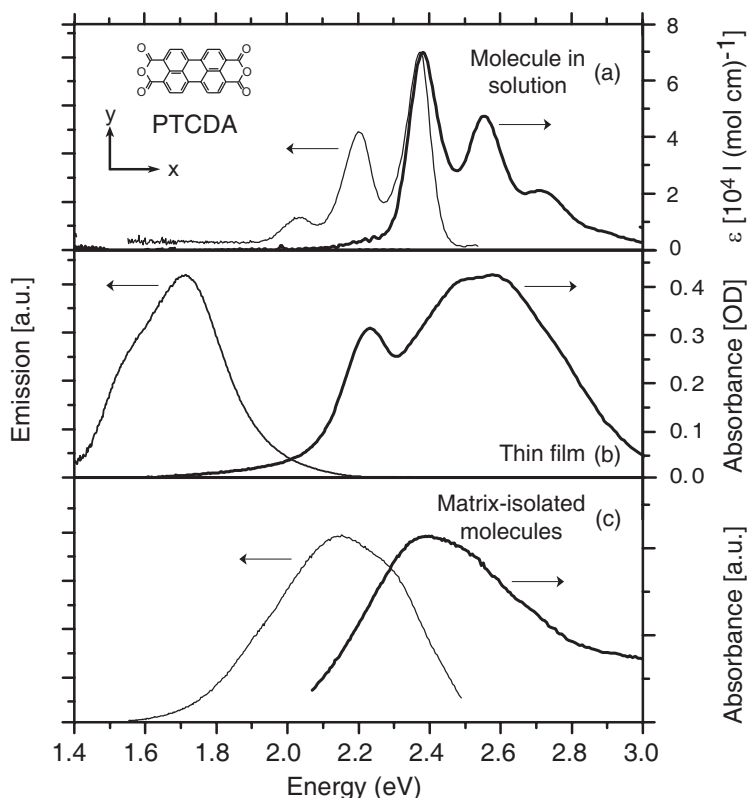


Figure 4.2.: Comparison of spectra as in Fig. 4.1, but for PTCDA. Molar extinction coefficient ϵ of PTCDA in (a) was evaluated from a 1.1 $\mu\text{mol/l}$ -solution in dimethyl sulfoxide (DMSO). Monomer emission in solution stems from a 0.4 $\mu\text{mol/l}$ -solution in chloroform. Film spectra in (b) are from a ~ 35 nm film on sapphire. Spectra of the 1% PTCDA/SiO₂ matrix sample are shown in (c).

It can be clearly seen that the $|\Delta T/T|$ signals for 2.30 eV, 2.00 eV, and 1.80 eV are shifted in time, with respect to their onsets. Interestingly, the curve for 2.00 eV exhibits two spikes in the first 200–300 fs, even though the actual $\Delta T/T$ signal remains zero. These spikes stem from a coherent artifact that can occur during pulse overlap, if pump and probe electric fields interact in the sample coherently to form a polarization grating⁵. A similar coherence spike can even be detected in a neat SiO₂ matrix, which has then been used as a reference sample for the characterization of the group delay $\tau_0(E)$. The group delay is also shown in Fig. 4.3, symbolized by open triangles⁶.

Let $S(\tau_i, E_j) = (s_{ij})$ be the $\Delta T/T$ signal matrix of multiple transient spectra as lines, each of them at different pump-probe delays τ_i . Energetic (wavelength) information thus

⁵For a discussion of the coherent artifact, see [62] and references therein.

⁶In Fig. 4.3, the complete group delay throughout the range of the white light spectrum in Fig. is about 1 ps. White light generation was performed in a 2 mm thick sapphire plate, as described in the last chapter. Looking at the GVD from sapphire in Table 3.1, it is evident that additional media such as filters and beamsplitters strongly contribute to GVD, underlining the common need for pulse recompression.

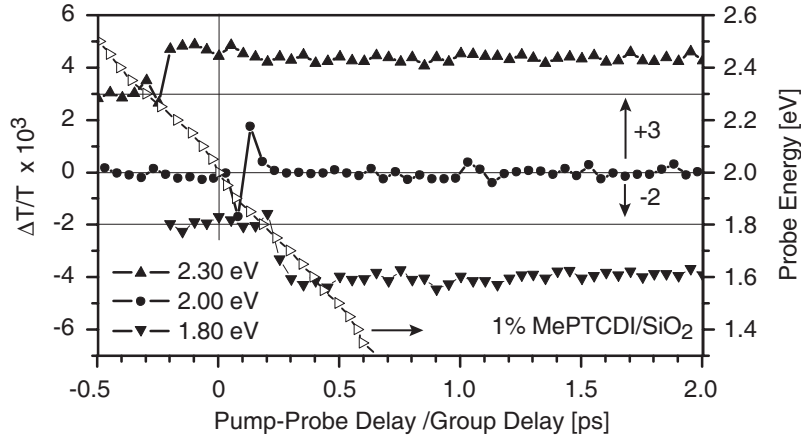


Figure 4.3.: Pump-probe traces from a 1% MePTCDI/SiO₂ matrix sample as a function of delay for probe energies of 2.30 eV, 2.00 eV, and 1.80 eV (left axis). Curves for 2.30 eV and 1.80 eV have been shifted vertically by 3×10^{-3} and -2×10^{-3} , respectively. Open triangles pointing towards the right demonstrate the group delay τ_{Gr} (cf. Eq. (3.24)) for the relative spectral component of the probe beam (right axis). Calibration was done with a neat SiO₂ matrix sample. See text for details.

is in columns E_j . If Δi is a vector of length $\max(j)$ containing the temporal calibration at every energy E_j , then the corrected transient spectrum matrix can be computed by

$$s_{i,j} \rightarrow s_{i+\Delta i,j} \quad (4.2)$$

All transient spectra in this section have undergone this mandatory correction, whose accuracy is about 200 fs.

4.2.1. MePTCDI transient absorption

Figure 4.4 depicts the transient spectrum of MePTCDI as a function of the probe energy in the range between 1.2 eV and 2.6 eV. The samples were excited into the lowest S_1 state with 22 fs pulses centered around 2.33 eV (532 nm, with FWHM 28 nm). The resolution of all transient spectra in this chapter is 3 nm (defined by a constant monochromator slit width), and the sampling step width was 4 nm. In order to avoid artifacts from possible signal contributions from a coherence regime during pulse overlap, and because of the uncertainty in the temporal calibration, we only present spectra at delays of 500 fs or larger. By this time, the $|\Delta T/T|$ signals in Fig. 4.3 have already surpassed their maxima and decay thereafter. Because of the high frequency of phonon oscillations in perylene-derived molecules [29, 108], we assume that by 500 fs the geometry of the excited molecule has already relaxed into some equilibrated state. Vibrational relaxation times below 400 fs have also been confirmed for similar perylene derivatives by VAN DIJK et al. [109, 110].

No significant changes in the shape of the spectra in Fig. 4.4 can be recognized, which implies that we look at a single state only, i. e., the excitons do not cross over multiple states probed simultaneously in the period observed. The transient transmittance signal can generally be explained by a sum of three contributions:

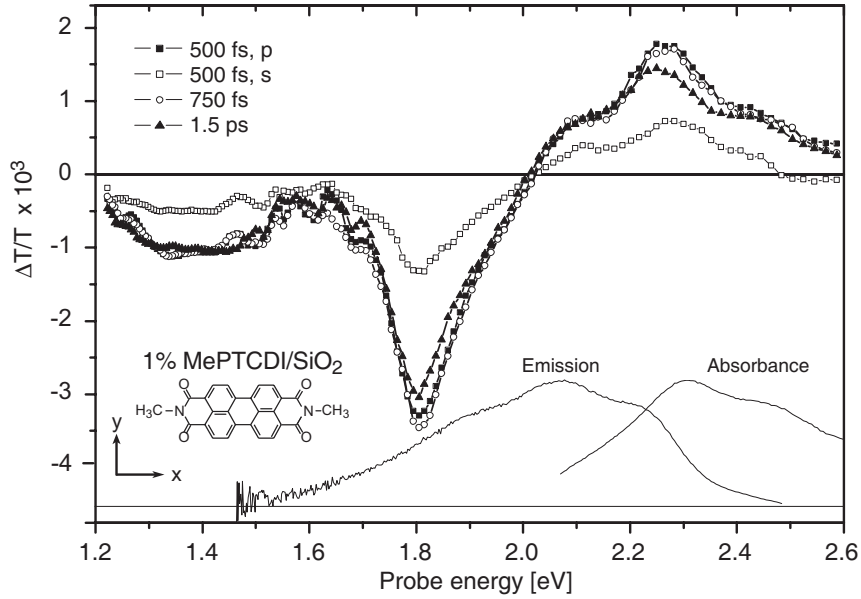


Figure 4.4.: Transient spectra of 1% MePTCDI/SiO₂ matrix sample for probe pulse delays of 500 fs, 750 fs, and 1.5 ps. Probe polarization was parallel to the pump polarization, except for open squares (probe and pump polarization perpendicular). Excitation was at 2.33 eV. Thin solid lines are fluorescence excitation and emission spectra as in Fig. 4.1 (c). Data taken at room temperature.

Ground state bleaching (GSB): GSB, also called *nonlinear absorption (NLA)*, is a consequence of the change of the linear absorption coefficient α because of depopulation of the ground state S_0 . Therefore, the transmission of the probe beam is increased compared to the unpumped sample, and $\Delta T/T$ is positive.

Stimulated emission (SE): If the probe energy is resonant with a transition from the relaxed excited state $S_{1,0}$ to the ground state $S_{0,0}$ or one of its vibrational levels $S_{0,n}$, the probe pulse can trigger stimulated emission into the direction of the probe beam, which results in a positive $\Delta T/T$ -contribution.

Excited state absorption (ESA): In case that the probe energy matches the difference $S_n - S_1$ between a higher excited state S_n and the S_1 state, energy from the probe beam is absorbed, provided that the optical transition is dipole-allowed. This is one of the reasons why TA is a useful tool in spectroscopy: excited states that cannot be accessed with conventional linear spectroscopy can be populated with a pump-probe technique⁷. Since the transmission of the probe beam is reduced by ESA, $\Delta T/T$ is negative.

In Fig. 4.4, it can be clearly seen that above 2.20 eV, the shape of the $\Delta T/T$ signal closely resembles the shape of the linear absorbance, which is shown again at the bottom

⁷Of course, multi-photon processes, like in a one-beam two-photon absorption experiment, must also be considered.

of the panel. Therefore, we attribute the major signal contribution in this region to GSB. A closer look reveals that the maximum of the differential transmittance $\Delta T/T$ lies at 2.26 eV, whereas the maximum of the absorbance is at 2.30 eV. This energetic shift can be interpreted under consideration that SE is also present in the signal: Due to the STOKES shift, the $S_{1,0} \rightarrow S_{0,0}$ transition between the excited zero phonon state $S_{1,0}$ and the zero-phonon ground state $S_{0,0}$ lies at 2.21 eV and is clearly visible as a shoulder in the emission spectrum. The spectrum for SE corresponds to the spectrum of spontaneous emission. This transition will also be probed as stimulated emission, and the SE contribution should appear in the $\Delta T/T$ -signal with its maximum at 2.21 eV. The observed peak at 2.26 eV thus arises from the fact that we see a superposition of both GSB and SE. Additionally, a shoulder in the transient transmittance shows up at 2.07 eV which clearly corresponds to the $S_{1,0} \rightarrow S_{0,1}$ peak of the emission spectrum. Hence, we assign this feature to SE back to the one-phonon ground state $S_{0,1}$.

The presence of SE is an indication that the transient transmittance signal stems mainly from isolated molecules: In case of an aggregated crystalline sample, MePTCDI has a negative exciton dispersion in k -space [34, 111], cf. Chapter 2. The intraband relaxation time for the depopulation of the initially prepared absorbing state at the Γ -point towards the border of the Brillouin zone is on the order of 100 fs [112, 113]. In this case, no stimulated emission would be observable, since then the cross-section for the indirect transition is much smaller. Intraband relaxation in MePTCDI and PTCDA will be the topic of the next chapter of this thesis. At energies below ~ 2.0 eV, the spectrum exhibits one pronounced peak around 1.81 eV and a broad structure around 1.38 eV, both with negative $\Delta T/T$, and with a peak ratio of about 3.1 : 1. This can be interpreted as ESA from S_1 into higher states of even symmetry, which are dipole-forbidden from the ground state S_0 . The main peak at 1.81 eV is rather narrow, whereas the second feature is broad. Around the fundamental amplifier output of ~ 1.56 eV, the spectrum may be distorted due to the heavily self-phase-modulated white light continuum (cf. Fig. 3.3). We will therefore not discuss any features in this range.

4.2.2. PTCDA transient absorption

The transient absorption spectrum $\Delta T/T$ for the PTCDA/SiO₂ matrix sample in Fig. 4.5 looks very similar to that of MePTCDI, with two large ESA bands and a broad GSB/SE feature. Again, the general shape of the spectra does not vary with time, except for slight variations, which can be explained by the overall reduced signal-to-noise ratio. The signal-to-noise ratio did not allow a determination of the perpendicular orientation below 1.5 eV.

In accordance with MePTCDI, the maxima of the absorbance at 2.39 eV and of the transient transmittance at 2.35 eV do not coincide. The $S_{1,0} \rightarrow S_{0,0}$ transition in emission now lies at 2.29 eV, i. e., the STOKES shift is of the same order as for MePTCDI. A SE contribution $S_{1,0} \rightarrow S_{0,0}$ also explains the shift between the maxima of $\Delta T/T$ and the absorbance, as in the case of MePTCDI. However, no distinct shoulder for stimulated emission from the $S_{1,0} \rightarrow S_{0,1}$ transition is visible.

In general, the transient absorption spectra of our PTCDA matrix sample somewhat resemble thin film spectra as presented in Sect. 4.3 later in this chapter: In contrast to

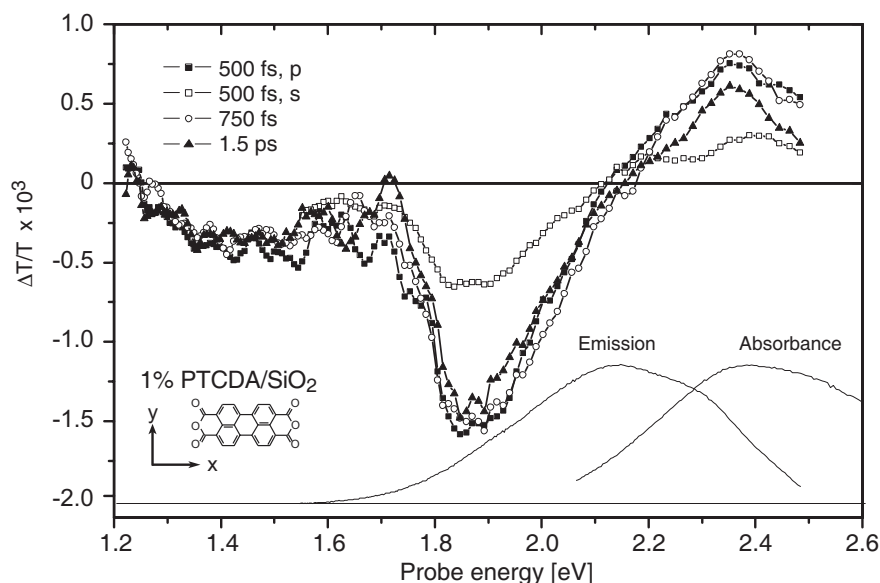


Figure 4.5.: Transient spectra of 1% PTCDA/SiO₂ matrix sample for probe pulse delays of 500 fs, 750 fs, and 1.5 ps. Open squares: perpendicular polarization at 500 fs. Excitation was at 2.39 eV (518 nm). Thin solid lines are fluorescence excitation and emission spectra as in Fig. 4.2(c). Data taken at room temperature.

MePTCDI, the peaks are broader, which might be related to *beginning* aggregation in the sample, as already considered in Sect. 4.1.3. This fact also holds for the main ESA peak $S_1 \rightarrow S_n$, which now lies around 1.87 eV, and there is also a broad feature around 1.43 eV with a small ESA contribution. The peak ratio, 3.2 : 1, is nearly the same as for MePTCDI.

4.2.3. Anisotropy and transition dipole moments

In addition to the energy of the excited states, we can evaluate the polarization of the transition dipole moments from the data in Figs. 4.4 and 4.5, using the concept of *polarization anisotropy*. Inserting a $\lambda/2$ -waveplate into the pump beam under an angle of 45° rotates the pump polarization by 90° and makes it perpendicular to the probe polarization. In Figs. 4.4 and 4.5, only the results for a delay of 500 fs are shown as open squares, corresponding to the solid squares for mutually parallel pump and probe polarizations.

In the context of luminescence, the anisotropy on the one hand provides information about the *dynamics of transition dipole moments*, e. g., the rotation of excited molecules in solution emitting fluorescence with a polarization being different from the polarization of excitation (but with the same transition dipole moment). On the other hand, polarization anisotropy helps to detect energy transfer *between states*, if absorbing and emitting dipoles actually differ.

For a pump-probe experiment, the *emitting* dipole is to be replaced by the *probed* transition dipole. In full accordance with the luminescence anisotropy [114], the pump-

4. Transient absorption spectra of PTCDA and MePTCDI

probe anisotropy can then be defined as

$$r(t) = \frac{I_{\parallel}(t) - I_{\perp}(t)}{I_{\parallel}(t) + 2I_{\perp}(t)}, \quad (4.3)$$

where I_{\parallel} and I_{\perp} are pump-probe signals $\Delta T/T$ parallel and perpendicular to the linearly polarized excitation, respectively. In pump-probe, we first create a population in S_1 being proportional to the square of the projection of the transition dipole moment \mathbf{p}_1 for absorption onto the pump electric field $\mathbf{E}_{P,u}$. The probe beam probes either the same transition dipole (GSB and SE) or any transition dipole to higher states (ESA). Again, the signal is proportional to the square of the projection of the relevant transition dipole moment \mathbf{p}_2 to the probe polarization ($\mathbf{E}_{P,\parallel}$ or $\mathbf{E}_{P,r,\perp}$)⁸. Averaging over an isotropic ensemble of molecules – like in our case of randomly oriented molecules inside the SiO₂ matrix –, Eq. (4.3) can be rewritten as

$$r(\theta) = \frac{1}{5}(3 \cos^2 \theta - 1), \quad (4.4)$$

where θ is the angle between the pumped and the probed dipole. Upper and lower limits of Eq. (4.4) are $r = 0.4$ or $r = -0.2$ for mutually parallel and perpendicular dipoles, respectively.

MePTCDI It has already been pointed out that the transition dipole moment for the $S_0 \rightarrow S_1$ -transition for PTCDA is oriented parallel to the long molecular axis, i. e., x-polarized. Of course, the same holds for MePTCDI for symmetry reasons. For the GSB/SE peak at 2.26 eV in Fig. 4.4, we obtain from Eq. (4.3) $r = 0.32 \pm 0.03$. In the case of GSB and SE, pump and probe transition dipoles have the same orientation, and we would rather expect $r = 0.4$. Nevertheless, the experimental value is clearly *not* $r = -0.2$. The D_{2h} symmetry of the molecular backbone limits the orientation for any probe transition dipole \mathbf{p}_2 either to $\mathbf{p}_2 \parallel \mathbf{p}_1$ or to $\mathbf{p}_2 \perp \mathbf{p}_1$. Therefore, we can state with confidence that even though the measured value does not fully coincide with the expected one, the transition dipoles in fact have the same polarization (x), i. e., they are oriented parallel the long axis of the MePTCDI molecule in agreement with the assumption of GSB and SE. The ESA peak at 1.81 eV has an anisotropy of $r = 0.33 \pm 0.02$, which means that the transition $S_1 \rightarrow S_n$ (where S_n is the state in question) is also x-polarized.

PTCDA For PTCDA, the pump-probe anisotropies evaluate to $r = 0.35 \pm 0.13$ for the GSB/SE-peak at 2.35 eV and $r = 0.35 \pm 0.07$ for the main ESA peak at 1.87 eV. This result gives evidence that this prominent $S_1 \rightarrow S_n$ transition is also x-polarized, in consistence with MePTCDI. All anisotropies reported here do not change considerably with time.

⁸We will elaborate more on this subject in Sect. 5.1.2, where fluorescence anisotropy is used to explain the coupling between inequivalent stacks of molecules.

4.2.4. Assignment by means of quantum-chemical calculations

In order to understand the nature of the excited states and the transition dipole moments between them, we now compare the experimental results with results from highly correlated quantum-chemical calculations. As already underlined, our main interest lies in transitions $S_1 \rightarrow S_n$ giving rise to excited state absorption, allowing us to probe the dynamics in the excited S_1 manifold.

The calculations have been carried out by K. SCHMIDT, D. BELJONNE, and J.-L. BRÉDAS⁹. Results have initially been reported in [115]. In this thesis, we focus on the major results required for the assignment of experimentally observed transitions. Here, we only outline the computational methods, and more details can be found in Appendix A.

SCHMIDT et al. have applied the *intermediate neglect of differential overlap (INDO)* method [116] with the *Coupled Cluster singles and doubles model (CCSD)* [117] and the *multireference determinant single and double configuration-interaction technique (MRD-CI)* [118]. The ground state S_0 was optimized with density functional theory (*DFT*), and the first excited singlet state S_1 with time-dependent density functional theory (*TD-DFT*). To account for possible geometrical relaxation of the molecule after excitation by the pump, calculations have been done for both the ground state (S_0) and first excited state (S_1) geometry. In the first case, the probe pulse would be absorbed before the structure of the excited molecule were able to relax. In the latter case, the molecule would rearrange and lower its energy first before absorption of the probe pulse.

MePTCDI The result for the MePTCDI molecule is shown in Fig. 4.6 for the CCSD method only. Since the result for the MRD-CI technique is qualitatively very similar to it, we do not draw the MRD-CI result, but numerical data for both methods are listed in Table A.1 in Appendix A. The short vertical bars in the center panel illustrate the energetic levels for the calculation in S_1 -optimized geometry, either with respect to the ground state (top tickmarks), or with respect to the lowest excited S_1 state $1B_{3u}$ (bottom tickmarks), and the long vertical bars display the oscillator strength of the respective transition. This illustration allows to recognize the states' symmetries immediately: Odd symmetry (ungerade) states are dipole-allowed from the even symmetry (gerade) ground state S_0 , whereas even symmetry (gerade) states are dipole-allowed from the odd symmetry (ungerade) S_1 state.

All lines are convolutions of the states with Gaussians of 175 meV FWHM. For comparison and completeness, the thin lines represent convolutions of the respective states for the S_0 -optimized geometry. As the order of the states and the oscillator strengths associated to them is essentially independent of either S_1 - or S_0 -optimized geometry, no distinction is possible between the excited state absorption $S_1 \rightarrow S_n$ taking place from the structurally unrelaxed or fully relaxed S_1 state. Concerning ground state absorption $S_0 \rightarrow S_n$, it is evident that the above a priori assumption to pump only the S_1 state is justified, because the higher states starting with $1B_{2u}$ at 3.58 eV (referred to as S_2 level

⁹Address: School of Chemistry and Biochemistry and Center for Organic Photonics and Electronics, Georgia Institute of Technology, Atlanta, Georgia 30332-0400, USA.

D. BELJONNE'S additional address: Service de Chimie des Matériaux Nouveaux, Centre de Recherche en Electronique et Photonique Moléculaires, Université de Mons-Hainaut, B-7000 Mons, Belgium.

4. Transient absorption spectra of PTCDA and MePTCDI

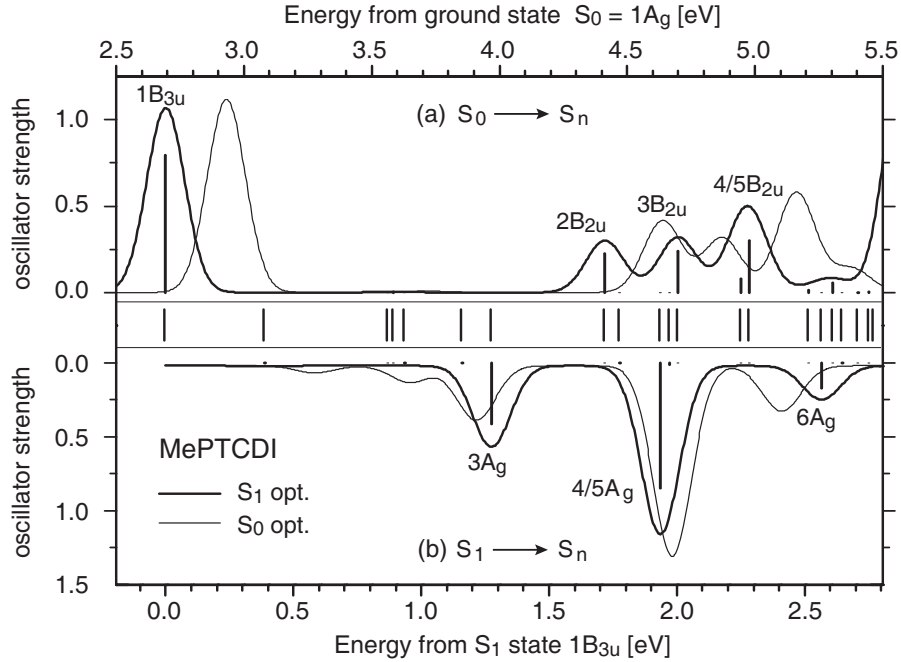


Figure 4.6.: Quantum-chemical calculations of the MePTCDI single molecule (CCSD method). The upper frame (a) shows the absorption from the ground state S_0 ($1A_g$) and the lower frame (b) the absorption from the lowest excited state $1B_{3u}$ (S_1). All lines are convolutions with Gaussians of 175 meV FWHM. Thick lines: S_1 -geometry, thin lines for comparison: S_0 -geometry. All labels refer to the D_{2h} symmetry of the MePTCDI backbone. Note that for the $S_1 \rightarrow S_n$ transitions, the axis for the energy from the ground state (top tickmarks) is only valid for the S_1 -optimized result.

in [23]) are very well separated in energy.

For ESA, the CCSD-calculation for MePTCDI exhibits three distinct peaks with energies 1.27 eV ($3A_g$), 1.93 eV ($4A_g$), and 2.57 eV ($6A_g$) with respect to $1B_{3u}$. The $4A_g$ state is accompanied by a small satellite, $5A_g$, at 1.97 eV¹⁰. All four transitions are x-polarized, i. e., the relevant transition dipole moment is parallel to the absorbing transition dipole for $S_0 \rightarrow S_1$ ¹¹. After Eq. (4.4), this result implies a pump-probe anisotropy of $r = 0.4$. Thus, it is obvious to assign the $4A_g$ state to the experimentally observed peak at 1.81 eV; in either case, no “competing” states are available.

Since the computational energetic separation between the $3A_g$ and the $4A_g$ equals 0.66 eV, we would expect the $3A_g$ state at about 1.14 eV, which is unfortunately just beyond the range experimentally accessible with white light from sapphire and silicon photodetectors. The experimentally observed broad structure around 1.38 eV can thus not clearly be correlated to the calculation. However, it might be attributed to the beginning formation of aggregates, because a similar peak shows up in the transient thin film spectra [113, 119] as illustrated in the following section. Considering the distance

¹⁰Full result in Table A.1, also for MRD-CI. Values for CCSD are in better agreement with the experiment.

¹¹MRD-CI results have the same polarizations.

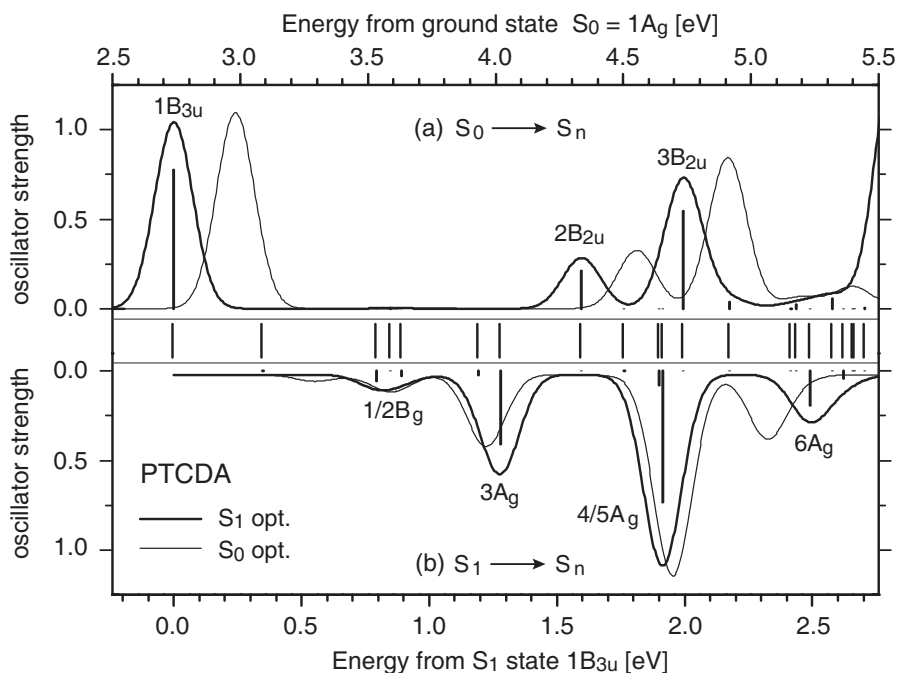


Figure 4.7.: Same as in Fig. 4.6, but for the PTCDA molecule (CCSD method). Again, ground state absorption is in (a), and absorption from S_1 in (b). All labels refer to the D_{2h} symmetry of the PTCDA molecule.

of 0.64 eV between the $4A_g$ and the $6A_g$ state, we would expect to find the latter in the experiment at 2.45 eV. The transient spectra in Fig. 4.4 give no clear indication of an ESA peak in the accessible region up to 2.6 eV. Thus, the $6A_g$ state is either at higher energies or its oscillator strength is significantly smaller than calculated.

PTCDA Figure 4.7 displays the result of the CCSD calculations for the PTCDA molecule. As for MePTCDI, the $S_1 \rightarrow S_n$ absorption in the CCSD calculation is dominated by three major peaks $3A_g$ (1.28 eV), $5A_g$ (1.91 eV, with satellite $4A_g$, 1.90 eV), and $6A_g$ (2.49 eV), with energies from $1B_{3u}$. Again, all these transitions are also x-polarized, and the experimental results are in full consistence with the calculation: We can assign the prominent experimental feature around 1.87 eV to the $5A_g$ peak. The broad peak around 1.43 eV is again most likely related to beginning aggregation (cf. Sect. 4.3), and the expected $6A_g$ is out of range on the high-energy flank. For a complete overview, energies, oscillator strengths and polarizations of the first 20 energy levels above the ground state are listed in Table A.2 for PTCDA, for both CCSD and MRD-CI calculations.

It is worth questioning whether the nature of the pronounced ESA peaks in MePTCDI and PTCDA might actually not be of excitonic character, but instead rather due to pump-induced charge carrier generation. For example, BULOVIĆ et al. [37] already reported on a peak around 1.85 eV for a PTCDA solution in the strongly polar *N*-methylpyrrolidone (NMP) that they attributed to charges. PROEHL and co-workers [120] also detected a peak in this range when growing PTCDA monolayers on charged mica substrates. From

the quantum-chemical point of view, both the absorption of the charged molecule and the excitonic $S_1 \rightarrow S_n$ transition are expected to have similar energies [121].

Compared to the PTCDA molecule in solution, where the room-temperature lifetime amounts to 4 ns [37], the lifetimes of the pump-probe signals as shown in Fig. 4.3 are very short, since they are on the order of ~ 55 ps for the peak at 1.81 eV and ~ 45 ps for the peak at 2.27 eV. Hence, we certainly do not deal with charges, as for them the expected lifetime is very long.

Another, albeit indirect indication, are recent results from OLIVEIRA et al., who measured two photon absorption (TPA) cross sections on various perylene derivatives [98, 99]. Their experiments reveal TPA resonances at energies that can be correlated to the $4A_g/5A_g$ states in our experiment, being confirmed by first TPA calculations on these materials [122].

4.3. Transient absorption spectra of thin films

4.3.1. MePTCDI and PTCDA transient absorption

A pronounced excited state absorption band is mandatory for the investigation of ultrafast excited state relaxation dynamics in our samples. Ideally, it lies within the pedestal of the white light supercontinuum (cf. Fig. 3.3) between 700–500 nm (1.77–2.48 eV) being shapeable with the AOPDF pulse shaper (Sect. 3.3.3), and it is wide enough to absorb even the broad spectrum of an ultrafast probe pulse. From the results of the preceding sections on isolated molecules, we have seen that the dominant ESA peaks in the range of 1.80–1.90 eV satisfy this constraint. Besides, their separation from the ranges where ground state bleaching occurs is sufficiently large to rule out the latter, which facilitates the discussion of the composition of the transient transmittance signal. Here, we show that thin films of MePTCDI and PTCDA, which are the main subject of our attention, behave similarly.

The transient absorption spectra of two thin films of MePTCDI and PTCDA are depicted in Figs. 4.8 and 4.9, respectively, together with the linear absorption spectra. Transient spectra have been obtained in the same manner as the ones for the matrix-isolated systems. The samples were pumped resonantly with 25 fs pump pulses into the lowest S_1 state as indicated by the pump spectra. Despite obvious similarities, the difference between the two materials is surprisingly much more pronounced than for the matrix-isolated systems shown in Figs. 4.4 and 4.5.

Again, the spectral shape remains mainly unchanged for both samples for different delays. In contrast to the matrix-isolated samples, where the signal-to-noise ratio is limited due to the small nominal thickness, thin film spectra can be recorded even at large delays¹². From the experimental results, three main trends can be extracted:

- The most prominent feature is still the main ESA peak in the range 1.80–2.00 eV, and it became visibly broader. However, whereas its shape and position in PTCDA

¹²As can be seen, the relaxation in MePTCDI is faster than in PTCDA, despite the fact that the experimental conditions were comparable. We will discuss this more quantitatively in the framework of exciton-exciton annihilation and diffusion in Chapter 6.

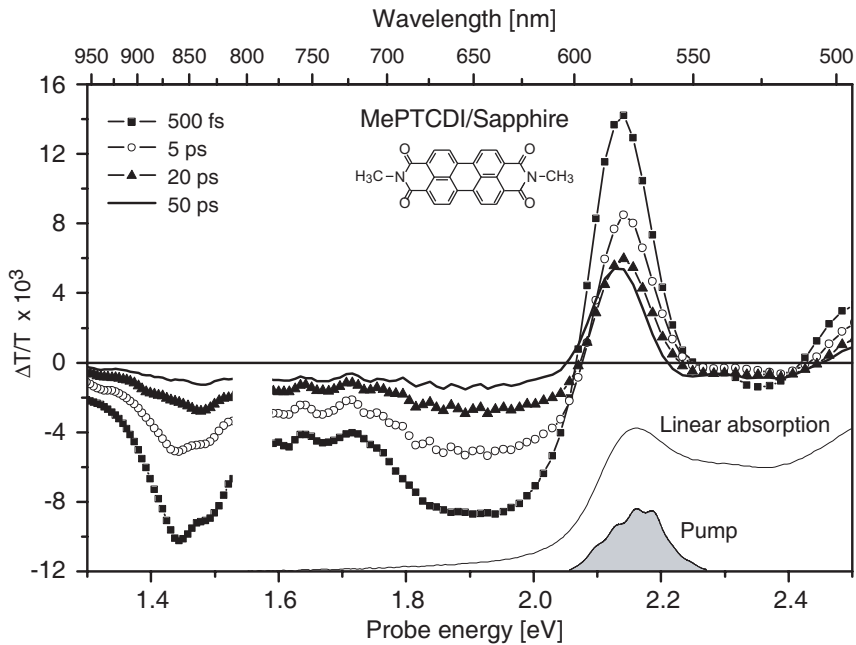


Figure 4.8.: Transient spectra of thin polycrystalline film (~ 35 nm) of MePTCDI on sapphire for various probe delays. Pump and probe polarizations were parallel. Excitation was at 2.16 eV (573 nm). The spectra around the fundamental amplifier output of 1.56 eV are distorted and have been suppressed. The thin line is the absorbance from Fig. 4.1 (b). Data were taken at room temperature.

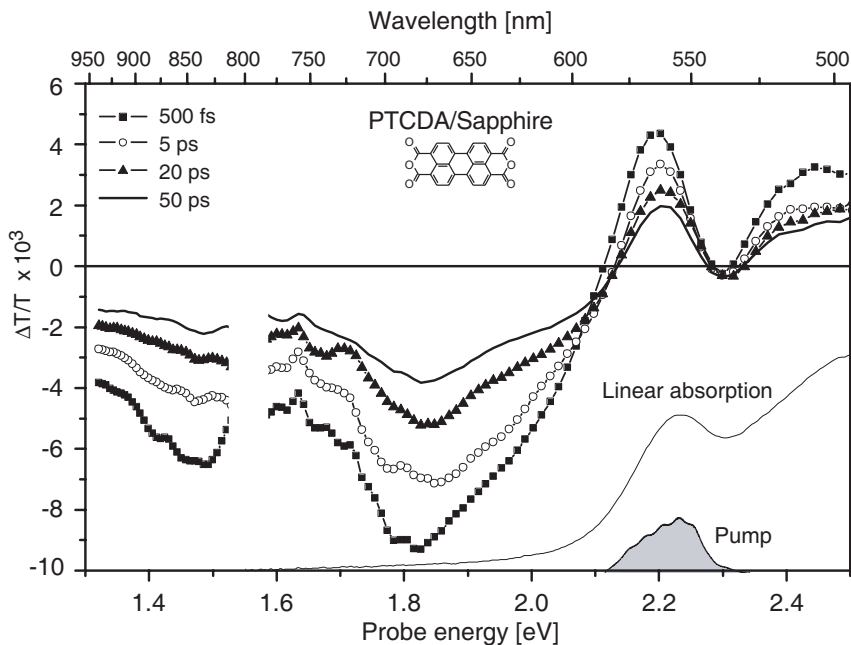


Figure 4.9.: As in Fig. 4.8, but for a PTCDA film (~ 35 nm) on sapphire. Excitation was at 2.22 eV (558 nm). Linear absorption is taken from Fig. 4.2 (b).

remains nearly unchanged, it has shifted in MePTCDI by 100 meV into the blue and has become plateau-like.

- In both cases, the small feature around 1.40 eV has increased strongly. For the MePTCDI thin film, it has even caught up with the main peak at 1.91 eV, and – except for very early times – the peak ratio is close to one. Besides, the energetic shift (80 meV) is again much larger than for the PTCDA sample, where the peak around 1.82 eV still predominates.
- As in the case of the matrix samples, the film spectra exhibit strong ground state bleaching contributions above ~ 2.05 eV, whose shapes compare favorably well with the shapes of the linear absorption spectra. Maxima of the transient transmittance $\Delta T/T$ and of the absorbance are separated in both samples by about 30 meV. As already mentioned above, stimulated emission cannot be held responsible for this shift here, because by 500 fs, the intraband relaxation in MePTCDI and PTCDA is already completed (cf. Sect. 5.2, [112, 113]), and the SE cross section is very small at the border of the Brillouin zone. However, $\Delta T/T$ becomes negative around 2.30–2.35 eV, which without doubt is caused by superposition of an additional significant ESA contribution. This contribution is stronger in MePTCDI, as can be seen by the peak ratios of the linear absorbance compared to the ones in the $\Delta T/T$ -signal.

4.3.2. From monomer to thin film

Unfortunately, a full quantum-chemical description of the thin film is not possible, due to the increasing complexity of the problem¹³. Yet, already dimer calculations allow conclusions in what manner the energetic states behave when more than one molecule is considered. Again, the calculations presented here were done by K. SCHMIDT, D. BELJONNE, and J.-L. BRÉDAS. They applied the INDO/S-method in combination with the CCSD technique to both MePTCDI and PTCDA stack dimers in the respective crystal geometry (cf. Sect. 2.2). More details about the computational methods used are again given in Appendix A.

In Figs. 4.10 and 4.11, all experimental results (top panels) and computational results (bottom panels) for the excited state absorption $S_1 \rightarrow S_n$ are displayed. In general, the correlation between experiment and calculation is better for MePTCDI. As the dimer calculation was performed in S_0 -optimized geometry, only the S_0 -optimized results for the monomer calculation are depicted.

One important remark should be made at this point about the electronic states involved: For the single molecules, we have seen in Sect. 4.2.4 that the lowest excited S_1 state is $1B_{3u}$ with odd symmetry, from which the probe beam excites into higher gerade states. In the case of a dimer, the mixing between the FRENKEL excitons (FE) and Charge-transfer states (CT) leads to a total of four supermolecular dimer states instead of the single $1B_{3u}$ state, as noted in Sect. 2.3.1. Either two are of even or odd symmetry. The lowest of these four states is $2A_g$ [100], being populated by excitation into either $1A_u$ or $2A_u$ and subsequent ultrafast relaxation. The probe pulse then excites into higher states

¹³Besides, it would also be beyond the scope of this (experimental) work.

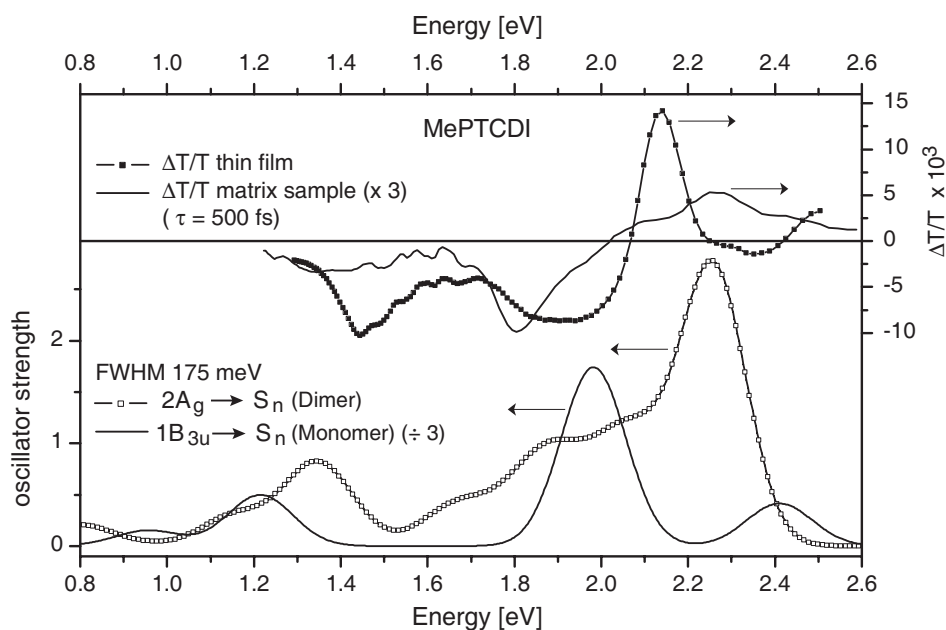


Figure 4.10.: Comparison of experimental spectra and quantum-chemical results at a glance. Top panel with right axis: Experimental transient spectra for a MePTCDI thin film (solid squares) and the matrix-isolated molecules (multiplied by 3, solid line). Lower panel with left axis: Oscillator strength for convoluted ESA spectra (Gaussian, 175 meV FWHM) for the MePTCDI dimer (open squares) and monomer (divided by 3, thin line, CCSD S_0 -optimized geometry) for transitions from the lowest excited state ($2A_g$ or $1B_{3u}$, respectively).

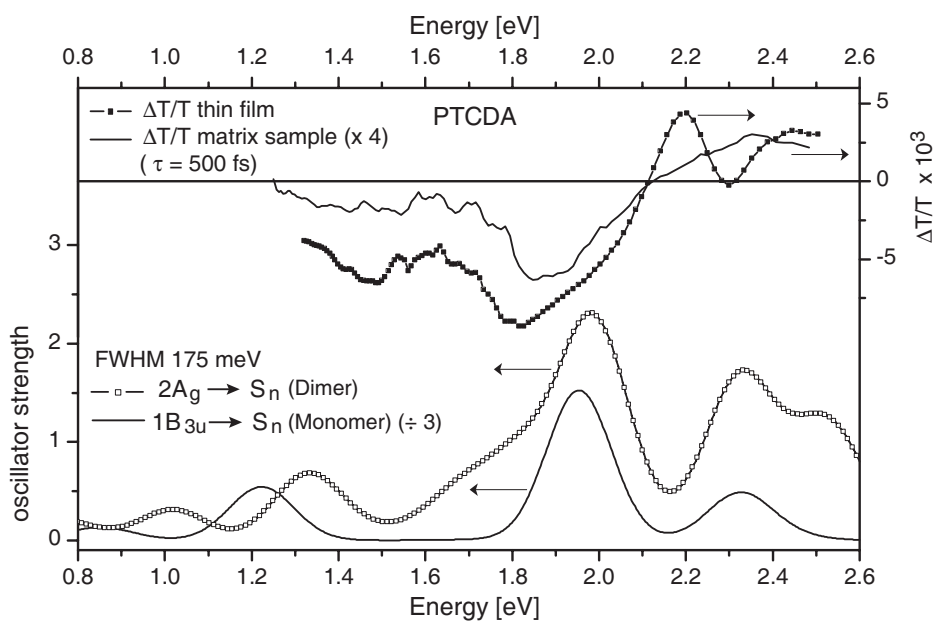


Figure 4.11.: Comparison of experiment and calculations as in Fig. 4.10, but for PTCDA. Experimental data for the matrix samples have been multiplied by 4, the curve for the monomer calculations has been divided by 3.

of odd symmetry. For this reason, Figs. 4.10 and 4.10 depict the transitions $2A_g \rightarrow S_n$ for the dimer calculations. From an experimental point of view, we omit an extensive discussion of the nature of the experimentally probed state at this stage, because this question will be addressed in the next chapter.

Obviously, Figs. 4.10 and 4.11 show that the development from the monomer to the dimer agrees reasonably well with the experimental data. Despite the very similar result for single molecules, the dimer spectra exhibit fundamental differences between MePTCDI and PTCDA in terms of the two ESA peaks around 1.85 eV and 2.35 eV: In MePTCDI, the latter gains a lot of oscillator strength at the expense of the former, while in PTCDA their ratio essentially remains constant. Furthermore, the inequality in the ratio between the peaks around 1.85 eV and 1.45 eV is also reflected very well in the calculations, and the shift of the 1.45 eV peak with respect to the small monomer features in this spectral region is reproduced by the calculations. As for the polarizations of the transitions $2A_g \rightarrow S_n$ to higher states – in comparison to the monomer with its isolated states –, the manifold number of close contributing states would necessitate an extensive discussion, which we want to avoid here. An overview of the polarizations and states involved in $2A_g \rightarrow S_n$ absorption is given in Appendix A.

In conclusion, we have presented transient absorption spectra of matrix-isolated molecules and thin films of MePTCDI and PTCDA, measured by pump-probe spectroscopy. The transient spectra of the matrix-isolated molecules were consistently explained and understood with help of quantum-chemical calculations. We were able to assign major excited state absorption transitions observed in the experiment. Signal contributions from ground state bleaching and stimulated emission are in accordance with the expectation towards isolated molecules. Polarization anisotropy allowed us to deduce the polarizations of the optical transitions, which could be confirmed by the calculations. In contrast to the similarity of the spectra of the matrix-isolated molecules, thin-film spectra of MePTCDI and PTCDA look distinctly different. The observed changes between the monomers and the films can be explained qualitatively by means of stack dimer calculations. In all experiments, the most prominent feature is a broad excited state absorption band in the range 1.80–2.00 eV, enabling us to use it for further investigation of the excited states relaxation dynamics as presented in the next chapters.

5. Exciton dynamics: Photoluminescence and intraband relaxation

We now turn towards intraband relaxation, i. e., the relaxation of excitons in k -space subsequent to optical excitation. For the remainder of this thesis, we will look at thin polycrystalline films of PTCDA and MePTCDI. As outlined in Chapter 2, MePTCDI and PTCDA share a negative exciton dispersion in the lowest excited state, leading to a very rapid depopulation of the absorbing state at the Γ -point. In this chapter, we address and discuss in detail this particular relaxation process and its dependence on temperature and excitation intensity.

Time-resolved luminescence measurements presented in Sect. 5.1 are the easiest and most obvious possible access to this relaxation. In the framework of this section, we also develop a model for the luminescence anisotropy being fundamentally different for MePTCDI and PTCDA. Our model is based on the accepted existence of DAVYDOV-split states due to the coupling between inequivalent stacks of molecules.

In the succeeding Sect. 5.2, we move in reverse time direction towards excitation, looking in detail at the intraband relaxation with the 300-fold higher time resolution of the pump-probe setup. By variation of exciton densities and temperature, we can demonstrate that the absorbing state is depopulated by assistance of phonons on a 100 fs time scale. Besides, we also discuss the pump-probe anisotropies and show that its full understanding calls for more sophisticated theoretical models.

5.1. Time-resolved photoluminescence

5.1.1. Relaxation into the emitting states

We consider time-resolved photoluminescence (PL) as the most straightforward starting point for the time-resolved investigation of relaxation after optical excitation. Luckily, there is a large temporal overlap between time-resolved PL (usable from 5 ps to the ns-regime) and our preferentially employed pump-probe techniques (which can be used between 20 fs and 500 ps). Both techniques provide complementary information: While PL probes the relaxed excited states, pump-probe can monitor both the absorption and the emission process, also including information about the higher excited states. The apparent advantage of PL lies in its moderate experimental effort¹, allowing to extract the following information:

- From the *rise of the luminescence signal*, we can evaluate the time necessary to complete excited-state relaxation, i. e. the time required for the population of the emitting state(s).

¹In comparison to pump-probe techniques.

- The *decay of luminescence* provides information about the relaxation of the emitting state(s) themselves and their lifetimes.
- *Spectral information* directly converts to energetic information. Especially in combination with the previous point, the character of the emitting state(s) may be clarified.

Of course, different materials are expected to show distinctly different PL signatures. Our specific interest lies in the difference between PTCDA and MePTCDI. This is not related or limited to PL only. Clearly, for a profound description, none of the three items listed above should be considered alone, and only a combination of all points allows full understanding. We mainly focus on the first point, the population of the emitting state(s) and we will touch the other two only if required for the interpretation.

The discussion about the nature of the emitting states in PTCDA-like material is controversial and still ongoing. Numerous experimental efforts have been undertaken to elucidate this contentious point: *Time-resolved* works on PTCDA heterostructures [123], ultrathin amorphous films [25], thin polycrystalline films [46], and single crystals [47] have left open questions. For MePTCDI, the knowledge is even scarcer, despite similar efforts on ultrathin films [25, 124], thin polycrystalline films [35, 43], and single crystals [35]. However, a detailed investigation of the emitting states is beyond the scope of this thesis.

The basic principle of the population of the emitting state has already been sketched in the introduction of the bandstructure scheme in Fig. (2.5). Excitons created at the Γ -point at $k = 0$ relax towards the border of the Brillouin zone (BZ) because of the negative exciton dispersion in k -space. Luminescence is an indirect process to vibrational levels of the ground state and therefore only possible with the aid of appropriate phonons.

Figure 5.1 shows the transient photoluminescence for MePTCDI and PTCDA thin films (35 and 25 nm) at room temperature and at 10 K. The samples have been excited with the second harmonic of a Ti:sapphire oscillator at 2.80 eV, creating exciton densities of $\sim 10^{17} \text{cm}^{-3}$. We have ensured a linear dependence of photoluminescence on the excitation density to exclude possible exciton-exciton interaction². For illustration of absorption and emission properties, Fig. 5.1 (b) and (d) also depict low-temperature absorption and emission spectra. In particular, polarized MePTCDI absorption spectra reveal DAVYDOV splitting, which has already been introduced in Chapter 2 and which we will discuss in detail in the following section 5.1.2.

Because our major interest is the temporal evolution, the PL for both samples has been spectrally integrated over the major (central) emission peak. We note that in all cases, the PL traces do not decay with a single exponential because of the interplay of several states. For a more detailed discussion on the nature of the emitting states, we refer the reader to [46, 47] for PTCDA and [35] for MePTCDI. The rise of luminescence can be fitted by an exponential function with a rise time of 10 ps, limited by the time resolution of the streak camera setup. In other words, *the upper limit for the population of the emitting states and therefore also the upper limit for the intraband relaxation time*

²In Sect. 5.2.2 and Chapter 6, we will quantify limits for the exciton densities above which exciton-exciton interaction and annihilation must be taken into account.

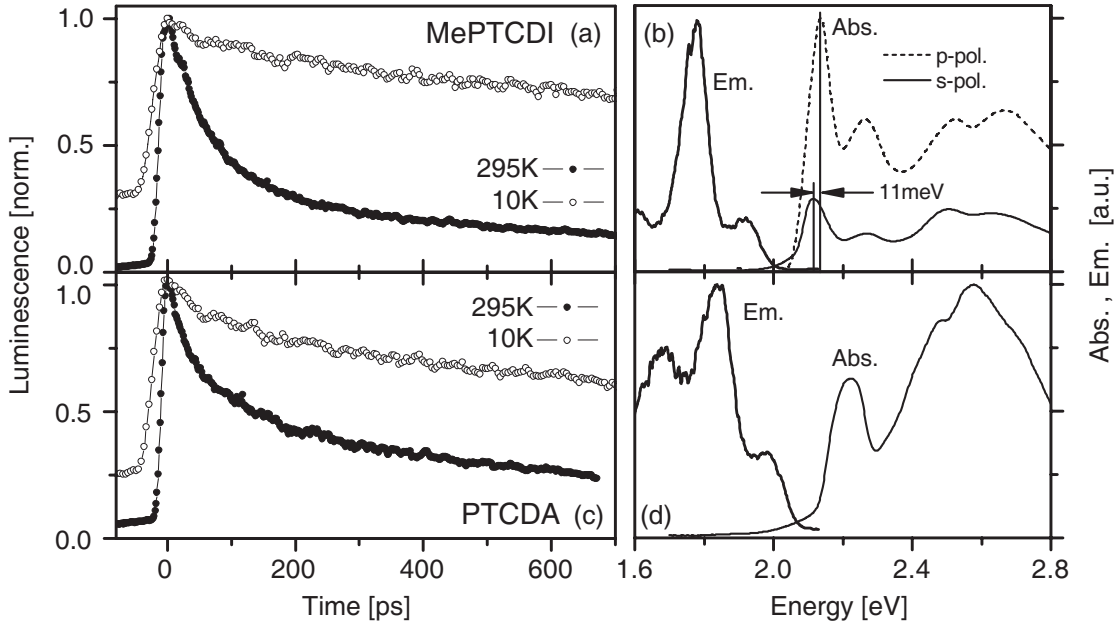


Figure 5.1.: Left panels: Normalized time-resolved photoluminescence for MePTCDI (a) and PTCDA (c) thin films at room temperature (solid circles) and at 10 K (open circles). In all cases, luminescence was spectrally integrated over the major (central) emission peak (MePTCDI 1.78 eV, PTCDA 1.84 eV). For illustration, the transient luminescence spectra (0..50 ps) at 10 K are depicted in (b) for MePTCDI and (d) for PTCDA. The panels on the right also show low-temperature absorption spectra of thin films (adapted from [23]). The highly ordered MePTCDI film in (b) exhibits a small DAVYDOV splitting of 11 meV in absorption (b), whereas the absorbance of the PTCDA film is independent of polarization.

constant is 10 ps, but the relaxation process might actually be much faster. Moreover, no conclusion about temperature dependence can be drawn. The limit of 10 ps is already one very important result from the PL measurements, and, in comparison to the values reported in the literature ([46, 47], for PTCDA), equal to a five fold improvement. Still, the relaxation process is not time-resolved, and therefore higher time resolution with the pump-probe technique, presented in Sect. 5.2, is mandatory.

5.1.2. Davydov splitting and luminescence anisotropy

We leave aside the question of intraband relaxation time constants for a moment and turn towards the “fingerprints” of our two different systems becoming manifest in photoluminescence. As in the previous chapter, anisotropy measurements enable us to provide information about the distribution and the dynamics of transition dipole moments in our samples. Furthermore, they can be employed to detect population changes between different energetic levels being sensitive to different optical transitions, i. e., with different transition dipole moments. We remark that in contrast to Sect. 4.2.3, we now consider the *luminescence anisotropy* and not the pump-probe anisotropy. Of course, the definition

from Eq. (4.3) still holds:

$$r(t) = \frac{I_{\parallel}(t) - I_{\perp}(t)}{I_{\parallel}(t) + 2I_{\perp}(t)}. \quad (5.1)$$

To investigate the population dynamics of the excited state, we recall that DAVYDOV splitting (DS) of all energetic levels is a result of the coherent superposition of molecular levels, due to the fact that there are two molecules in the unit cell. If we discuss it in the framework of quasi-one-dimensional systems, we consider two stacks of two translationally inequivalent classes of molecules. In this case, “quasi-1D-states” coherently couple³. DS has been verified in MePTCDI by polarized absorption ([23], depicted in Fig. 5.1 (b)) and in α -PTCDA by ellipsometry [48]. Values of $\Delta E = 11$ meV for the former and $\Delta E = 37$ meV in the latter case have been reported at the Γ -point. However, calculations predict a drastically reduced splitting of $\Delta E = 1$ meV [40] or even less [100] for the border of the Brillouin zone, where DS has not yet been observed directly in luminescence, employing high spectral resolution. The concept of luminescence anisotropy developed in this section uses a different approach. We first have to introduce the theoretical background for further discussion of the luminescence anisotropy for a system of coupled dipoles.

Luminescence anisotropy model

According to the superposition of DAVYDOV-split band states, the transition dipole moments to these split states can be regarded as a coherent superposition of molecular transition dipole moments. In Fig. 2.6, this has already been sketched for the unit cells of MePTCDI and PTCDA.

We now consider a single unit cell containing two molecules, oriented arbitrarily with respect to our laboratory coordinate system. For simplicity, the treatment is done in a 2D isotropic model⁴. Fig. 5.2 (a) depicts the laboratory system (coordinates x and y), the two molecular transition dipole moments \mathbf{P}_A and \mathbf{P}_B , as well as their sum $\mathbf{P}_A + \mathbf{P}_B$ and their difference $\mathbf{P}_A - \mathbf{P}_B$. Let θ be the angle between the x -axis and the dipole $\mathbf{P}_A + \mathbf{P}_B$. The normalized vectors

$$\mathbf{P}_{\pm} = \frac{\mathbf{P}_A \pm \mathbf{P}_B}{\sqrt{2}} \quad (5.2)$$

are called DAVYDOV components (DCs). Obviously, the ratio $\xi = |\mathbf{P}_-|/|\mathbf{P}_+|$ of their absolute values is determined by the mutual orientation of the molecules in the unit cell. In case of absorption for a crystal with N molecules, this superposition yields for the total transition dipole [40]

$$\mathbf{P}_{\pm,N} = \sqrt{N} s_a \frac{\mathbf{P}_A \pm \mathbf{P}_B}{\sqrt{2}}, \quad (5.3)$$

where s_a is a vibronic overlap factor for absorption. Although the shape of the absorption spectra can only be explained by superposition of FRENKEL and charge-transfer states,

³Please note that we keep talking of quasi-1D states although DAVYDOV splitting is independent of the dimensionality.

⁴We will comment on the 3D case further below.

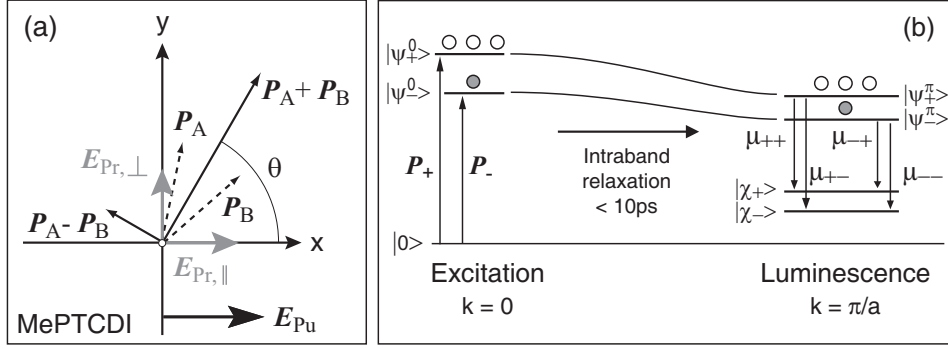


Figure 5.2.: Left (a): 2D laboratory system for coupled molecular transition dipole moments \mathbf{P}_A and \mathbf{P}_B , with additive and subtractive superpositions $\mathbf{P}_A + \mathbf{P}_B$ and $\mathbf{P}_A - \mathbf{P}_B$, respectively. In the example (a), the orientation of \mathbf{P}_A and \mathbf{P}_B actually corresponds to the orientation of two molecules in the MePTCDI unit cell. Right (b): Overview of excitation and population of two DAVYDOV-split states $|\psi_{\pm}^0\rangle$, subsequent intraband relaxation, and the transitions allowed in indirect emission. For the example in (b), $\xi^2 = 1/3$.

the transition dipole moments \mathbf{P}_{\pm} are dominated by the FRENKEL contribution [8, 34, 38, 39].

For the indirect emission back to the higher vibrational states of the ground state, it is important to include the coupling of adjacent molecules in stack direction, which also leads to DAVYDOV-split states $|\chi_{\pm}\rangle$ of the vibrational progression. The phonon-assisted emission thus allows four transitions dipole moments [40]

$$\boldsymbol{\mu}_{++} = \boldsymbol{\mu}_{--} = s_e (\mathbf{P}_A + \mathbf{P}_B) \quad (5.4)$$

$$\boldsymbol{\mu}_{+-} = \boldsymbol{\mu}_{-+} = s_e (\mathbf{P}_A - \mathbf{P}_B), \quad (5.5)$$

with a FRANCK-CONDON factor s_e for emission. The absorption into $|\psi_{\pm}^0\rangle$ at the Γ -point and the emission $|\psi_{\pm}^0\rangle \rightarrow |\chi_{\pm}\rangle$ onto the vibrational states $|\chi_{\pm}\rangle$ at the border of the Brillouin zone are sketched in the simplified band structure plot in Fig. 5.2.

In order to evaluate the microscopic emission contribution of a single pair of molecules in the unit cell, we define the direction of the linearly polarized pump electric field parallel to the x-axis (cf. Fig. 5.2):

$$\mathbf{E}_{Pu} = E_{Pu} \begin{pmatrix} 1 \\ 0 \end{pmatrix}. \quad (5.6)$$

In anisotropy measurements, the population is probed parallel and perpendicular to the polarization of excitation by emission of radiation. We thus obtain for the probe electric fields⁵:

$$\mathbf{E}_{Pr,\parallel} = E_{Pr} \begin{pmatrix} 1 \\ 0 \end{pmatrix} \quad \text{and} \quad \mathbf{E}_{Pr,\perp} = E_{Pr} \begin{pmatrix} 0 \\ 1 \end{pmatrix}. \quad (5.7)$$

⁵This concept is general and not limited to luminescence anisotropy, and it may also be applied in pump-probe experiments.

In this coordinate system, the \mathbf{P}_i and $\boldsymbol{\mu}_{ij}$ are best represented in polar coordinates:

$$\mathbf{P}_+ = P_+ \begin{pmatrix} \cos \theta \\ \sin \theta \end{pmatrix} \quad \text{and} \quad \mathbf{P}_- = P_- \begin{pmatrix} \sin \theta \\ \cos \theta \end{pmatrix} = \xi P_+ \begin{pmatrix} \sin \theta \\ \cos \theta \end{pmatrix} \quad (5.8)$$

$$\boldsymbol{\mu}_{++} = s_e P_+ \begin{pmatrix} \cos \theta \\ \sin \theta \end{pmatrix} \quad \text{and} \quad \boldsymbol{\mu}_{+-} = s_e P_- \begin{pmatrix} \sin \theta \\ \cos \theta \end{pmatrix} = s_e \xi P_+ \begin{pmatrix} \sin \theta \\ \cos \theta \end{pmatrix} \quad (5.9)$$

The two DAVYDOV-split states $|\psi_{\pm}^0\rangle$ are initially populated according to the ratio ξ of the respective transition dipole moments \mathbf{P}_+ and \mathbf{P}_- (Fig. 5.2) and the orientation of those with respect to the pump electric field. The populations n_{\pm} are proportional to the square of the projections of \mathbf{P}_{\pm} to \mathbf{E}_{Pu} :

$$n_+(\theta) \propto (\mathbf{P}_+ \mathbf{E}_{\text{Pu}})^2 \quad (5.10)$$

$$n_-(\theta) \propto (\mathbf{P}_- \mathbf{E}_{\text{Pu}})^2. \quad (5.11)$$

In Fig. 5.2, we illustrate an example for $\xi^2 = 1/3$. If the emission is incoherent, we can add the contributions from the $|\psi_{\pm}^{\pi}\rangle$ to the $|\chi_{\pm}\rangle$ under consideration of the respective transition dipole moment(s). For example, the contribution from $|\psi_{+}^{\pi}\rangle$ to $|\chi_{+}\rangle$, detected parallel to the x-axis, yields

$$I_{\parallel}^{++}(\theta) = C (\mathbf{P}_+ \mathbf{E}_{\text{Pu}})^2 (\boldsymbol{\mu}_{++} \mathbf{E}_{\text{Pr},\parallel})^2, \quad (5.12)$$

with a proportionality factor C . If we sum up all possible contributions with the definitions made in Eqs. (5.4–5.11), we obtain the contribution from one unit cell for parallel and perpendicular direction:

$$\begin{aligned} I_{\parallel}(\theta) &= \sum_{i,j=+,-} I_{\parallel}^{ij}(\theta) = \sum_{i,j=+,-} C n_i(\theta) (\boldsymbol{\mu}_{ij} \mathbf{E}_{\text{Pr},\parallel})^2 \\ &= C E_{\text{Pu}}^2 E_{\text{Pr}}^2 P_+^4 (\cos^2 \theta + \xi^2 \sin^2 \theta)^2 \end{aligned} \quad (5.13)$$

$$\begin{aligned} I_{\perp}(\theta) &= \sum_{i,j=+,-} I_{\perp}^{ij}(\theta) = \sum_{i,j=+,-} C n_i(\theta) (\boldsymbol{\mu}_{ij} \mathbf{E}_{\text{Pr},\perp})^2 \\ &= C E_{\text{Pu}}^2 E_{\text{Pr}}^2 P_+^4 ((1 + \xi^4) \cos^2 \theta \sin^2 \theta + \xi^2 (\sin^4 \theta + \cos^4 \theta)). \end{aligned} \quad (5.14)$$

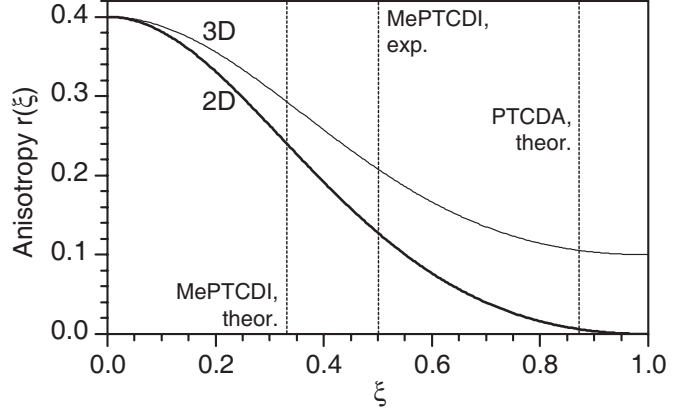
The treatment in a 2D model implies that the molecules and therefore also all vectors for the DCs for absorption and emission as well as the electric field polarizations lie parallel to the substrate. This is a reasonable assumption for such planar molecules as MePTCDI and PTCDA [23, 101]. In order to obtain the macroscopic contribution from the whole isotropic polycrystalline sample⁶, the microscopic contributions in Eqs. (5.13, 5.14) have to be integrated over the angle θ from 0 to 2π , leading to the following simple expressions:

$$I_{\parallel} = C (3(1 + \xi^4) + 2\xi^2) \quad (5.15)$$

$$I_{\perp} = C ((1 + \xi^4) + 6\xi^2). \quad (5.16)$$

⁶Our laser spot size by far exceeds the size of the crystallites.

Figure 5.3.: Anisotropy r as a function of the ratio ξ of the DAVYDOV components for a 2D system (thick line) and a 3D system (thin line). Dashed vertical lines indicate theoretical and experimental limits for MePTCDI and PTCDA. See text for explanation.



The luminescence anisotropy of our sample in a 2D model can then be computed by insertion of Eqs. (5.15, 5.16) into the definition of the anisotropy in Eq. (5.1):

$$r_{2D}(\xi) = \frac{2 - 4\xi^2 + 2\xi^4}{5 + 14\xi^2 + 5\xi^4}. \quad (5.17)$$

We note that even if the populations of $|\psi_{\pm}\rangle$ would be changed by equilibration or down-relaxation, i. e.

$$\tilde{n}_+ = \tilde{n}_- = \frac{n_+ + n_-}{2} \quad \text{or} \quad \begin{cases} \tilde{n}_+ = 0 \\ \tilde{n}_- = n_+ + n_- \end{cases}. \quad (5.18)$$

the “relaxed” anisotropy $\tilde{r}_{2D}(\xi)$ takes the same value as in Eq. (5.17). For clarity, Fig. 5.3 illustrates $r_{2D}(\xi)$, and also $r_{3D}(\xi)$ for completeness⁷. It is worth discussing the limits of the very important result for $r_{2D}(\xi)$ in Eq. (5.17) for a moment:

- Firstly, the absence of any DAVYDOV components ($\xi = 0$) yields $r(0) = 0.4$. This limit is in full consistence with the result for an ensemble of randomly oriented dipoles in an isotropic sample.
- Secondly, $r(\xi)$ is a measure for the orientation of the two molecules in the unit cell, because it only depends on $\xi = |\mathbf{P}_-|/|\mathbf{P}_+|$. In particular, Eq. (5.17) reveals that for identical size of the DCs with $\xi = 1$, r_{2D} disappears. This is obvious from symmetry arguments⁸. This upper limiting case becomes extremely interesting for our model system PTCDA, where the two molecules in the unit cell are arranged under an angle of $\delta = 82.2^\circ$, as shown in Fig. 2.6. This leads to nearly equally sized DCs \mathbf{P}_+ and \mathbf{P}_- .

⁷Apart from the fact that the treatment of the 3D system is a more tedious task, it generally can be done the same way as for the 2D case. We just mention the result and display it in Fig. 5.3:

$$r_{3D}(\xi) = \frac{2 - 2\xi^2 + 2\xi^4}{5 + 10\xi^2 + 5\xi^4}. \quad (5.19)$$

⁸ $r_{3D}(1)$ does not disappear because the transverse electric fields of \mathbf{E}_{Pr} cannot monitor any projection of dipoles onto the longitudinal direction, which results in “missing” population information.

Measurements of luminescence anisotropies

After the theoretical discussion of the expected luminescence anisotropies for our model systems MePTCDI and PTCDA, we now present the experimental results. Prior to time-resolved PL, we have carefully verified our main assumption of isotropically oriented crystallites in the thin film. For that purpose, we have performed polarized *cw* absorption measurements with a spectrophotometer for vertical and horizontal orientation, and also under an angle of 45° as double-check. Moreover, *cw* luminescence has also been proven to be isotropic by means of polarized emission measurements with a fluorescence spectrometer. Hence, our working hypothesis of randomly oriented crystallites was justified.

Figure 5.4 depicts luminescence decay curves for MePTCDI and PTCDA, for both room temperature and low temperature. For the measurements at 10 K, the samples were kept in helium vapor continuous flow in a bath cryostat. Solid circles illustrate parallel polarization of excitation and emission detection. These data have already been shown in Fig. 5.1. Open circles symbolize the data for emission being perpendicular to the polarization of excitation. The polarization dependence of the streak camera setup was accounted for by a calibration as described in Sect. 3.4.2.

For MePTCDI at room temperature in Fig. 5.4 (a), we obtain a value of $r \approx 0.2$ for the initial anisotropy. This experimental value is now compared with theoretical and experimental limits reported by HOFFMANN [23] which are also depicted in Fig. 5.3 by vertical lines. The angle of orientation of the two MePTCDI molecules in the unit cell is $\delta = 36.8^\circ$. In the simplest theory considering only FRENKEL excitons, ξ can be computed by the following relation:

$$\xi = \frac{\sin(\delta/2)}{\cos(\delta/2)}. \quad (5.20)$$

Inserting the angle of $\delta = 36.8^\circ$ into Eq. (5.20), we obtain a theoretical *lower* limit of $\xi = 0.33$. Further contribution from, e. g. CT states, would increase ξ . On the other hand, HOFFMANN evaluated an experimental polarization ratio of $\xi^2 = \alpha_s/\alpha_p$ for a highly ordered film of MePTCDI on a stretched polymer substrate. Here, α_s and α_p are the absorbances perpendicular and parallel to the principal orientation, respectively. The outcome of this experiment was an *upper* limit of $\xi = 0.5$. Any reduction of the imperfections of the samples and the increase of the experimental accuracy would only have led to a reduced value of ξ . Thus, the expected window of the anisotropy ranges from $r(0.33) = 0.24$ from geometry up to $r(0.5) = 0.13$ for the experiment. Assuming a reasonable 5% error in the stability of the streak camera system, we can estimate the error for the luminescence anisotropy to $\Delta r \approx 0.04$ (for MePTCDI). Hence, our experimental value of $r = 0.2 \pm 0.04$ in Fig. 5.4 (a) is in good agreement with the above limits.

In the case of PTCDA, we have pointed out that \mathbf{P}_+ and \mathbf{P}_- are nearly equally sized, yielding a theoretical limit of $\xi \approx 0.87$ after Eq. (5.20). We therefore expect a nearly vanishing luminescence anisotropy from Eq. (5.17). This behavior also agrees quite favorably with the experimental result in Fig. 5.4 (c), where r more or less equals zero. We thus conclude that the initial time-resolved luminescence anisotropy for both MePTCDI and PTCDA can fully be explained with the exciton model of DAVYDOV-split states.

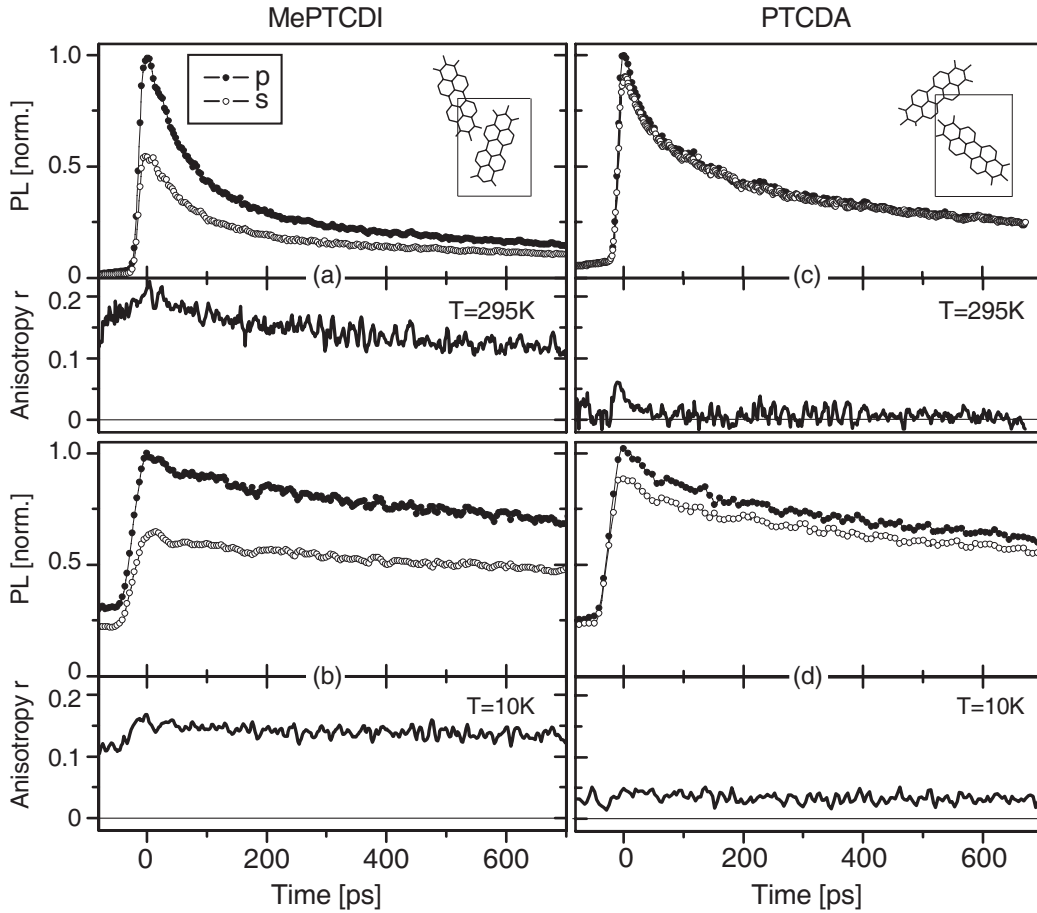


Figure 5.4.: Polarization-dependent time-resolved photoluminescence (normalized) for MePTCDI (left column) and PTCDA (right column) thin polycrystalline films. The corresponding anisotropies were calculated as defined by Eq. (5.1). In all PL panels, solid circles depict mutually parallel polarizations of excitation and emission, while for the open circles the emission was detected perpendicular to excitation. (a) and (c) are at room temperature, and (b) and (d) are at 10K. The small insets in (a) and (c) symbolize the orientation of the two molecules in the unit cells.

For comparison, we have also determined the PL anisotropy at low temperature to learn about the origin of the anisotropy decay for MePTCDI in Fig. 5.4 (a). Low-temperature data in Fig. 5.4 do neither show any significant decay of r for MePTCDI, nor for PTCDA. To initially comment on the starting values of the PL anisotropies, we point towards the offsets in the PL curves as a result of the long-lived luminescence from the previous excitation. When computing $r = (I_{\parallel} - I_{\perp}) / (I_{\parallel} + 2I_{\perp})$, these offsets essentially cancel in the numerator and add in the denominator, thus leading to an artificially reduced value for r , as visible for MePTCDI. However, this cannot account for the fact that in PTCDA, $r \approx 0.03$ has slightly increased. Because the lower limit for r definitely is $r = 0$, this slight increase can most likely be attributed to the experimental accuracy (of 0.025 for the same 5% laser stability).

The absence of a decay of r with time indicates that the samples keep their polarization memory for a long time. The only way to lose this memory is the diffusion of excitons from their parent crystallite where they were created into adjacent crystallites with a different macroscopic orientation. In other words, a constant r demonstrates that the transfer of excitons by diffusion into adjacent crystallites is inhibited. SCHÜPPEL et al. [125] recently have shown in PTCDA by luminescence quenching experiments that this diffusion can be described by a thermally activated hopping process, with an activation energy of approximately 13 meV. This energy corresponds to a temperature much higher (150 K) than our measurement temperature of 10 K. We therefore conclude that this thermally activated hopping mechanism can explain the behavior of the anisotropy decay in Fig. 5.4.

5.2. Ultrafast intraband relaxation

Resuming the discussion of the actual intraband relaxation time constants started at the beginning of this chapter, we have found the necessity for much higher time resolution than provided by the streak camera setup. For this reason, we have explored our samples with the pump-probe technique, offering a time resolution of about 30 fs, more than 300 times better than the streak camera setup. For the remainder of this thesis, we will continue with the presentation of pump-probe results, whilst the samples of choice will still be thin polycrystalline films.

5.2.1. Depopulation of the absorbing states

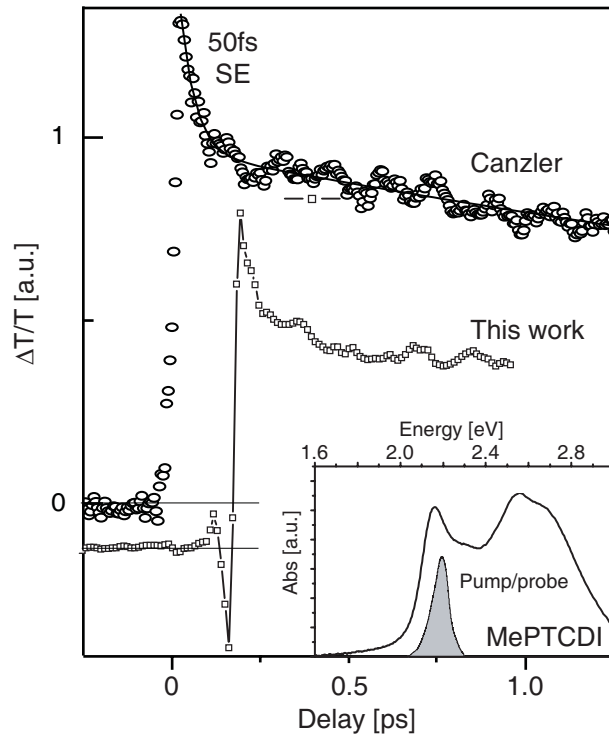
The most straightforward pump-probe experiment is to investigate the changes of the population of the absorbing state $|\psi^0\rangle$ at the Γ -point⁹, because the principle knowledge of how $|\psi^0\rangle$ can be accessed is obvious: A *stimulated emission/nonlinear absorption* experiment that transfers the excited state population in S_1 back to the ground state S_0 (or one of its vibrational levels $S_{0,n}$) can be carried out without any knowledge about higher excited states, as is imperative for the interpretation of an *excited state absorption* experiment. Clearly, the transition dipole moment for SE is the same as for absorption.

Degenerate pump-probe

During the brief review of the measurements of the excitonic relaxation in MePTCDI by CANZLER [35] in Sect. 2.4, we already mentioned that the depopulation of the absorbing state $|\psi^0\rangle$ was estimated to be on the order of 50 fs. This value was extracted from degenerate pump-probe experiments, one of which is illustrated in Fig. 5.5, symbolized by the curve with the open circles. The inset depicts the measurement principle of equal pump and probe spectra. Experimentally, this is accomplished quite easily by splitting a small fraction from the pump beam to serve as probe beam. The very first decay with a time constant of 50 fs of the (positive) transient transmittance $\Delta T/T$ was interpreted as the decay of stimulated emission (SE) in the absorbing state $|\psi^0\rangle$, while the subsequent decay was explained by the recovery of the bleached ground state. Hence, this 50 fs time

⁹For this and the following subsection, we omit the fact that $|\psi^0\rangle$ is DAVYDOV-split as in Sect. 5.1.2 (pump and probe beam polarizations are mutually parallel).

Figure 5.5.: Two spectrally integrated resonant pump-probe measurements on MePTCDI thin films for comparison. Data are presented as differential transmittance $\Delta T/T$ as a function of probe delay. Data with open circles are reproduced from CANZLER [35]. New measurement data, gathered in the framework of this thesis, are symbolized by open squares. In both cases the samples were excited in the lowest excited state and probed as depicted in the inset. The shaded grey area depicts the (equal) pump and probe spectrum. The curve for the new data has been shifted vertically and horizontally for clarity and better comparison. Measurements were carried out at room temperature.



constant would then correspond to the time required to depopulate the absorbing state towards the border of the BZ.

In order to verify this “reference data”, this experiment has been repeated with a 35 nm polycrystalline film of MePTCDI. Our experimental conditions were comparable to the original ones: the time resolution was approximately 30 fs, measured by auto-correlation, the exciton density created was on the order of $5 \times 10^{19} \text{ cm}^{-3}$, and pump and probe spectra were placed amidst the lowest excited state band. In Fig. 5.5, the new data are symbolized by open squares, which have been shifted vertically and horizontally to the reference data for clarity. Whereas the two curves relax very similarly after their maxima, the rise of $\Delta T/T$ significantly differs. The fact that the new data oscillate symmetrically around the steep onset of the curve makes us very suspicious because it extremely resembles and points towards a coherent artifact (see, e. g., [62]). Phononic modulations (that are superimposed on the original data) can hardly explain such symmetric spikes. Our repeated experiment thus definitely casts some doubt on the original interpretation [35] of the degenerate pump-probe experiment. We conclude that unfortunately no information about the depopulation of the absorbing state can be extracted from our SE experiment, leaving open the answer to the question of intraband relaxation.

Excited state absorption

Another issue of the discussed degenerate pump-probe experiment is the fact that the $\Delta T/T$ signal is in general composed of contributions from stimulated emission (probing the S_1 state) and nonlinear absorption (NLA, probing the ground state S_0). However, excited state absorption might also be present, if the system also offers optical transitions

from S_1 to higher excited states at the respective energy. Now, NLA can be omitted if the probe spectrum is shifted to lower energies and placed beyond the onset of linear absorption. Different pump and probe spectra also allow us to use a cutoff filter between the sample and the detector to block unwanted stray light from the pump beam.

Here, our knowledge of the transient film spectra from Sect. 4.3 comes into play, indicating that both MePTCDI and PTCDA have a very broad excited state absorption band in the range of 1.80–2.00 eV. For this reason, in all further pump-probe measurements we have used a Gaussian envelope probe spectrum, centered around 640 nm (1.94 eV) with a FWHM of 34 nm (100 meV). Amplitude and phase of the probe pulses have been shaped with the AOPDF pulse shaper that was presented in Sect. 3.3.3¹⁰. The Gaussian spectral envelope allowed probe pulses with a temporal FWHM $\Delta\tau_p$ of 23 fs.

PTCDA Figure 5.6 presents the result for the excited state absorption experiment for PTCDA. As shown in (b), the sample was pumped resonantly at the lowest excited state, creating exciton densities of $3 \times 10^{19} \text{cm}^{-3}$, which corresponds to one exciton per 85 molecules. The probe spectrum around 640 nm is also depicted as dark shaded area. The cross-correlation measurements by sum-frequency generation resulted in a FWHM of $\Delta\tau_{xc} \approx 40$ fs for the cross-correlation envelope. Looking at Fig. 5.6 (a), we first note that the negative sign of the $\Delta T/T$ signal indicates that its origin actually is excited state absorption. At a first glance, the rise of $|\Delta T/T|$ appears to happen approximately on a 50 fs time scale.

We will now comment in detail on this particular temporal evolution of the transient transmittance in Fig. 5.6 (a), taking into account the limited instrument response. Our aim is learn about the relaxation of excitons in k -space, after they have been created by a pump pulse of Gaussian shape and finite length at the absorbing state $|\psi^0\rangle$ at the Γ -point. For a sketch of this process, we remind the reader of Figs. 2.5 or 5.2. Let $\tau_{r,1}$ be the life time of $|\psi^0\rangle$ being depopulated by intraband relaxation towards the border of the BZ by a single channel:

$$n_{\psi^0}(t) = n_{\psi^0,0} e^{-t/\tau_{r,1}} \Theta(t) , \quad (5.21)$$

with the HEAVISIDE step function $\Theta(t)$. If we look at a band state $|\psi^k\rangle$ with a different k -vector ($0 < k \leq \pi/a$) being fed by this population, its population increases correspondingly:

$$n_{\psi^k}(t) = n_{\psi^0,0} (1 - e^{-t/\tau_{r,1}}) \Theta(t) . \quad (5.22)$$

We will postpone the discussion about the actual nature of $|\psi^k\rangle$ until later in this chapter.

We now consider that we probe this band state in our pump-probe experiment. In the ideal impulsive limit, both pump and probe are $\delta(t)$ -pulses with infinite time resolution. In this particular case, we would be able to observe $n_{\psi^k}(t)$ from Eq. (5.22) directly as $\Delta T/T$ signal. Due to the finite length of the pulses, however, the measured signal $S(t)$

¹⁰From Figs. 4.8 and 4.9, we know that the broad ESA bands of MePTCDI and PTCDA peak at slightly higher wavelengths than the chosen center wavelength of 640 nm. However, since the usable spectral output window of the AOPDF is limited, the chosen configuration still allowed to use the device down to 570 nm for other experiments, which would otherwise not have been possible.

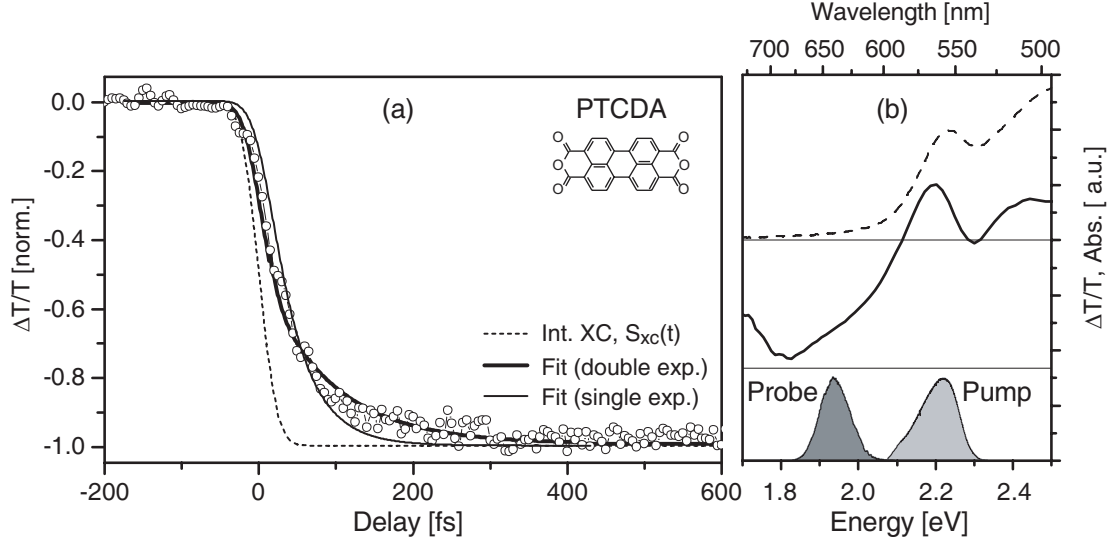


Figure 5.6.: Left (a) Normalized transient transmittance for a PTCDA thin film for the first few hundred femtoseconds, taken at room temperature. Dashed line: integrated cross-correlation by Eq. (5.26). Thin and thick solid lines are fits with one and two exponentials after Eqs. (5.28, 5.30), respectively. See text for a detailed discussion. Right (b) depicts the experimental configuration with linear absorption of the thin film (dashed), transient absorption at 500 fs (solid line) as well as pump and probe spectra.

must be described as a convolution of the population $n_{\psi^k}(t)$ with the instrument response $R(t)$ of finite temporal length:

$$S(t) = \int_{-\infty}^{\infty} dt' n_{\psi^k}(t' - t) R(t'). \quad (5.23)$$

In our case, the instrument response is given by the Gaussian cross-correlation envelope of pump and probe beam, as defined in Sect. 3.3.1:

$$R(t) = I_{xc,2}(t) = I_0 \exp\left(-\frac{4 \ln 2}{\Delta\tau_{xc}^2} t^2\right). \quad (5.24)$$

To facilitate reading, it is helpful to define the abbreviation $\tilde{\tau}_{xc} = \Delta\tau_{xc}/\sqrt{4 \ln 2}$. The convolution in Eq. (5.23) can then be written as

$$S(t) = \int_{-\infty}^{\infty} dt' n_{\psi^k,0} (1 - e^{-(t'-t)/\tau_{r,1}}) \Theta(t' - t) I_0 e^{-t'^2/\tilde{\tau}_{xc}^2}. \quad (5.25)$$

Before we finally write down the complete resolution of Eq. (5.25), we regard our probed state $|\psi^k\rangle$ as instantaneously fed, i. e., its population rate $k_{r,1} = 1/\tau_{r,1}$ is infinite. Let $I_{xc,2}(t)$ be the real time resolution. Just like the example in the previous paragraph

with δ -pulses, this now corresponds to the other extreme. Then, the solution to Eq. (5.25) is fairly simple:

$$S_{\text{xc}}(t) = -\frac{1}{2} \left[1 + \operatorname{erf} \left(\frac{t}{\tilde{\tau}_{\text{xc}}} \right) \right], \quad (5.26)$$

where $S_{\text{xc}}(t)$ has been normalized to -1. The function $\operatorname{erf}(t)$ denotes the error function, which is defined as

$$\operatorname{erf}(t) = \frac{2}{\sqrt{\pi}} \int_0^t dx \exp(-x^2). \quad (5.27)$$

Eq. (5.26) essentially is the *integrated cross-correlation* envelope function and defines the measurable pump-probe signal $S_{\text{xc}}(t)$ for a nonphysical instantaneously rapid intraband relaxation. Therefore, $S_{\text{xc}}(t)$ corresponds to the time resolution of the system. In Fig. 5.6 (a), the integrated cross-correlation is symbolized by the dashed line. Clearly, $|\Delta T/T|$ initially rises approximately (parallel) with time resolution. Yet, after a few tens of femtoseconds, $\Delta T/T$ moves away from $S_{\text{xc}}(t)$. Hence, we can already remark that our transient transmittance signal can definitely resolve the intraband relaxation process of excitons away from $|\psi^0\rangle$.

For a more quantitative interpretation and the extraction of actual values for $\tau_{\text{r},1}$, we solve Eq. (5.25) analytically and obtain:

$$S_1(t) = -\frac{1}{2} \left[1 + \operatorname{erf} \left(\frac{t}{\tilde{\tau}_{\text{xc}}} \right) - e^{-\frac{4t\tau_{\text{r},1} - \tilde{\tau}_{\text{xc}}^2}{4\tau_{\text{r},1}^2}} \left(1 + \operatorname{erf} \left(\frac{2t\tau_{\text{r},1} - \tilde{\tau}_{\text{xc}}^2}{2\tilde{\tau}_{\text{xc}}\tau_{\text{r},1}} \right) \right) \right]. \quad (5.28)$$

Again, $S_1(t)$ has been normalized to -1. The best fit of $S_1(t)$ to the data with a value of $\tau_{\text{r},1} = 40$ fs (with fixed $\tilde{\tau}_{\text{xc}} = 25$ fs) is also shown as *thin solid line* in Fig. 5.6 (a). Although it performs quite reasonably, the fit shows some clear deviations from the data after some 50 fs, where the experimental curve is bent more smoothly. As for our fit function, such an additional curvature can only be accomplished by the introduction of a second decay time constant $\tau_{\text{r},2}$ bending the fit at the relevant position. This motivates to rewrite Eq. (5.22) and to introduce a second exponential including a second relaxation time constant $\tau_{\text{r},2}$:

$$n_{\psi^k}(t) = n_{\psi^0,0} \left(1 - a_1 e^{-t/\tau_{\text{r},1}} - a_2 e^{-t/\tau_{\text{r},2}} \right) \Theta(t). \quad (5.29)$$

The result for our fit function corresponding to Eq. (5.28) then reads:

$$S_2(t) = -\frac{1}{2} \left[1 + \operatorname{erf} \left(\frac{t}{\tilde{\tau}_{\text{xc}}} \right) - \sum_{i=1,2} a_i e^{-\frac{4t\tau_{\text{r},i} - \tilde{\tau}_{\text{xc}}^2}{4\tau_{\text{r},i}^2}} \left(1 + \operatorname{erf} \left(\frac{2t\tau_{\text{r},i} - \tilde{\tau}_{\text{xc}}^2}{2\tilde{\tau}_{\text{xc}}\tau_{\text{r},i}} \right) \right) \right]. \quad (5.30)$$

$S_2(t)$ has also been fit to our data, yielding best values for $\tau_{\text{r},1} \approx 0$ ($\tau_{\text{r},1} \leq \tilde{\tau}_{\text{xc}}$) and $\tau_{\text{r},2} = 88$ fs. In order to reduce the number of free parameters, we used $a_1 = a_2 = \frac{1}{2}$. These

values are suited to sufficiently describe the data. We thus assume that both exponentials in Eq. (5.29) contribute equally, which is the simplest case. The corresponding curve is depicted in 5.6 (a) as *thick solid line*, matching the experimental PTCDA data very well and significantly better than the fit with $S_1(t)$ with a single exponential.

It is important to stress that the above formulation so far is just a mathematical trick to obtain $S_2(t)$. Introducing a second time constant as in Eq. (5.29) may suggest that the band state $|\psi^k\rangle$ is actually populated with excitons from two different sources. This is not reasonable because all population has to come from $|\psi^0\rangle$. The main concept that comes into play here is the fact that the excited state absorption is sensitive to different momentum states. In terms of the observation of two decay time constants, we therefore conclude that we probe two states simultaneously. Since $\tau_{r,1}$ is on the order of time resolution or smaller, the most straightforward conclusion is that it describes the initial excitation into the absorbing state $|\psi^0\rangle$. *The second time constant $\tau_{r,2}$ represents the intraband relaxation time constant towards the border of the BZ*, and the signal contribution stems from the state $|\psi^k\rangle$. Since the oscillator strength for a pump-probe transition from any $|\psi^k\rangle$ to higher band states $|\phi^k\rangle$ should not strongly depend on k , the choice of $a_1 = a_2 = \frac{1}{2}$ is also justified with this assumption. In the case of a multi-step relaxation process with intermediate states, $\tau_{r,2}$ is an upper limit for the depopulation time of $|\psi^0\rangle$.

One important remark should also be made about the above statement $\tau_{r,1} \approx 0$ ($\tau_{r,1} \leq \tilde{\tau}_{xc}$). Because the zero position of the time axis had to be adjusted manually – due to the fact that the temporal pulse overlap accords with an arbitrary translation position in space of the used translation stage – a definite value for $\tau_{r,1}$ cannot be given. For the thick solid fit curve in Fig. 5.6, a value of $\tau_{r,1} = 2$ fs has been retrieved from the fit. A slightly different choice of the zero position of the time axis yields a fit of equal quality for the onset with a slightly changed value for $\tau_{r,1}$. The statement $\tau_{r,1} \approx 0$ ($\tau_{r,1} \leq \tilde{\tau}_{xc}$) thus means “ $\tau_{r,1}$ is below the time resolution limit”.

MePTCDI After the somewhat tedious introduction of the mathematical apparatus, the treatment of the results for the MePTCDI thin film is now significantly easier. The experimental conditions for this experiment were comparable: A resonant pump pulse created excitons densities of $2 \times 10^{19} \text{cm}^{-3}$ at the Γ -point, corresponding to one exciton per 95 molecules. Again, the probe spectrum was centered around 640 nm.

In the same manner as before, Fig. 5.7 sketches the experimental outline together with the results. From the data in Fig. 5.7 (a) we can draw the same conclusions for MePTCDI as has been done for PTCDA: At first, negative $\Delta T/T$ identifies excited state absorption as the signal source. At the border of the displayed range, $|\Delta T/T|$ starts to decrease again, which is also the case for PTCDA, although hardly visible in Fig. 5.6. The origin of this decrease is exciton recombination and exciton-exciton annihilation and happens on a much longer time scale than currently investigated. This process will be discussed later in this chapter, and in detail in Chapter 6. Secondly, $|\Delta T/T|$ also starts to rise with time resolution, but bends away from it and exhibits a subsequent delayed rise. Fitting with the double-exponential fit function $S_2(t)$ from Eq. (5.30) works best with the values $\tau_{r,1} \approx 0$ ($\tau_{r,1} \leq \tilde{\tau}_{xc}$) and $\tau_{r,2} = 56$ fs and convincingly describes the experimental data. For the fit displayed in Fig. 5.7, $\tau_{r,1} = 3$ fs was used. Despite the more rapid relaxation

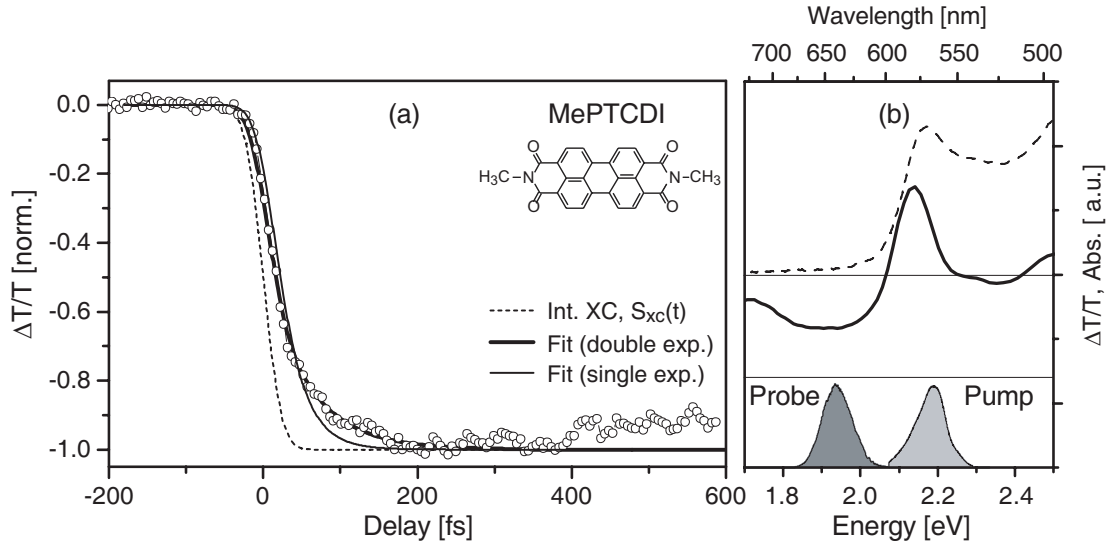


Figure 5.7.: Same as in Fig. 5.6, but for a MePTCDI thin film. Left (a) Experimental data at room temperature, integrated cross-correlation (dashed) symbolizing time resolution, thick and thin solid line (double and single exponential fit, respectively). Right (b) depicts this experiment's configuration with thin film linear absorption (dashed), transient absorption at 500 fs (solid line) as well as pump and probe spectra.

process, the single-exponential fit with $S_1(t)$ is visually inferior, as can be seen from Fig. 5.7(a) (thin solid line). As before, we therefore conclude that the depopulation time of $|\psi^0\rangle$ towards the border of the Brillouin zone for MePTCDI under the given conditions has an upper limit of $\tau_{r,2} = 56$ fs.

Before we continue with a detailed investigation of intraband relaxation under different experimental conditions, there is another important remark to be made. Under the assumption that the higher exciton bands we probe into have the same k -dependence and a k -independent transition dipole from the lowest excited band, exciton relaxation should affect the transient transmittance neither temporally nor spectrally. Regarding the higher state(s) we probe into, we actually know the spectrum from our own investigations in Chapter 4. Their exciton dispersion will be determined by the coupling of completely different molecular states than in the lowest excited state, and their exciton-phonon coupling might be different. Thus, it is most unlikely that both dispersion and transition dipole moments remain the same. Yet, the fact that we observe two relaxation time constants is directly interpreted as the sign that dispersion and/or transition dipole moments do change.

5.2.2. Intensity and temperature dependence

Up to now, we have not commented on the mechanism of excitonic relaxation. Relaxation in k -space, of course, requires the wave vector k to be changed. Just as in the indirect emission process, this is done by the aid of phonons. Obviously, two straightforward ways to alter the phononic properties of the sample are the variations of excitation intensity

and/or sample temperature, which will be addressed in this section.

The dependence on temperature and on excitation intensity was measured with the same configuration as the data presented in the previous section, using excited state absorption, monitored by a probe beam centered around 640 nm. Again, the samples were pumped resonantly into the lowest excited state. Metallic neutral-density filters were employed to modify the pump intensity. For the low-temperature measurements, the samples were mounted to a cold finger of a helium continuous flow optical cryostat. The exciton densities created were estimated as described in Sect. 3.4.1. In order to keep the figures less overcharged and not to mention exciton densities repeatedly, they have been summarized in Table 5.1. The numbers in the columns ((h) = *high* intensity, (m) = *moderate* intensity, (l) = *low* intensity), broken down both by sample and by temperature, then denote the densities that are related to a certain label in one of the following graphs.

Ultrafast initial relaxation

Figure 5.8 shows the normalized transient transmittance $\Delta T/T$ for PTCDA for the first few hundred femtoseconds after excitation for room temperature (a) and low temperature (b). The data already shown in Fig. 5.6 are also repeated as open circles in (a). For better comparison, each curve has been normalized to its maximum value. We note that the total time window displayed is different for both panels, so that the curvature of the rise of $|\Delta T/T|$ can be better seen.

As for the exemplary case in Fig. 5.6, fit functions are displayed. We first employed $S_2(t)$ to fit the data. If in this case it turned out that $\tau_{r,2} \rightarrow \tau_{r,1} \approx \tilde{\tau}_{xc}$, $S_2(t)$ and $S_1(t)$ are no longer distinguishable. In this case, the fit $S_1(t)$ with one exponential is displayed, which is commonly the case for the highest excitation densities.

Keeping the temperature constant in (a), it is clearly visible that the relaxation process is slowed down with decreasing excitation intensity. While the delayed rise of $|\Delta T/T|$ is pronounced for curves (m) and (l), it is not visible for (h). There, $\Delta T/T$ even remains

Table 5.1.: Exciton densities created by the pump pulse (all values in cm^{-3}) for the pump-probe experiments in Chapters 5 and 6. The letters ((h),(m),(l)) in parentheses correspond to the labels of the curves in the figures starting with Fig. 5.8. The curves (time scans) for intermediate densities (h-m) and (m-l) are not always shown in the figures, yet the parameters that have been evaluated from them, e. g., the $\tau_{r,2}$ as in Fig. 5.10. Exciton densities were estimated using Eq. (3.50).

Sample	T [K]	Exciton densities related to figure labels [cm^{-3}]				
		(h)	(h-m)	(m)	(m-l)	(l)
PTCDA	295	3.1×10^{20}	1.4×10^{20}	3.1×10^{19}	1.6×10^{19}	3.9×10^{18}
PTCDA	5	2.2×10^{20}	1.1×10^{20}	2.5×10^{19}	1.3×10^{19}	2.9×10^{18}
MePTCDI	295	2.4×10^{20}	1.2×10^{20}	2.4×10^{19}	1.1×10^{19}	1.9×10^{18}
MePTCDI	5	1.9×10^{20}	1.0×10^{20}	2.1×10^{19}	1.1×10^{19}	2.8×10^{18}

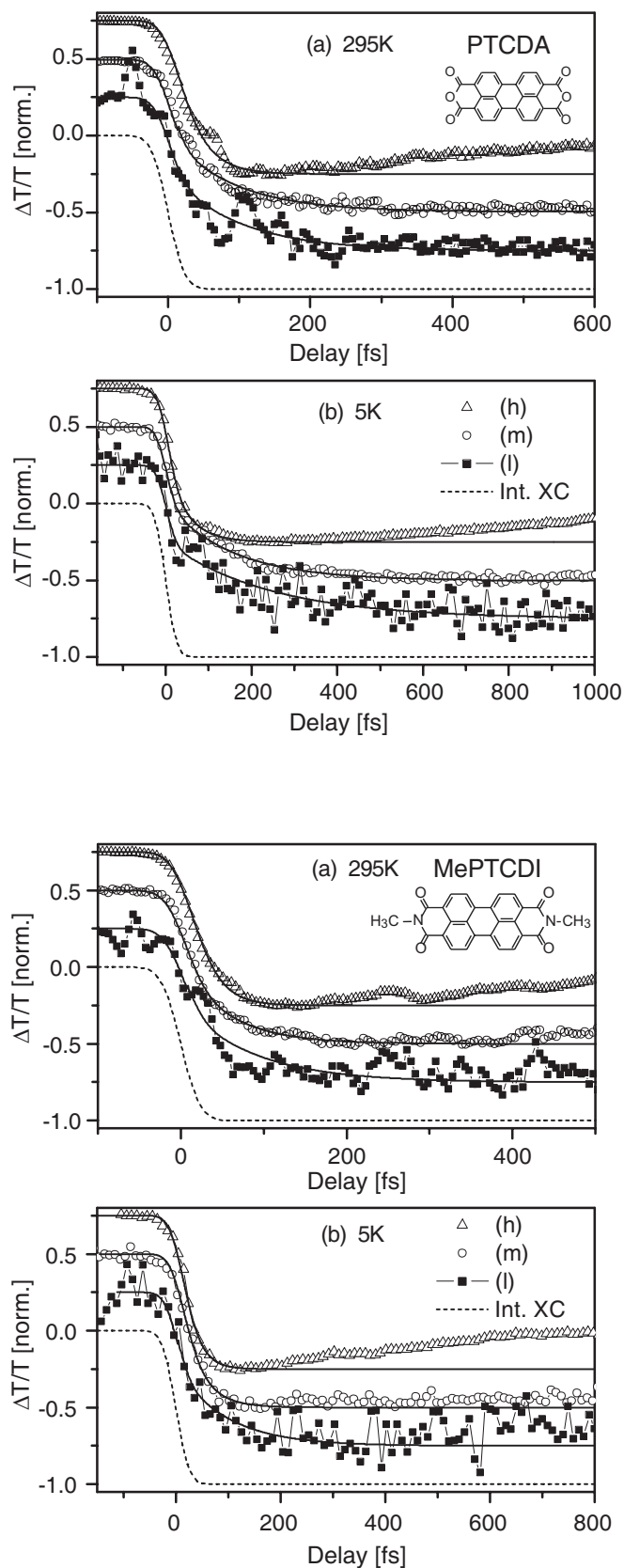
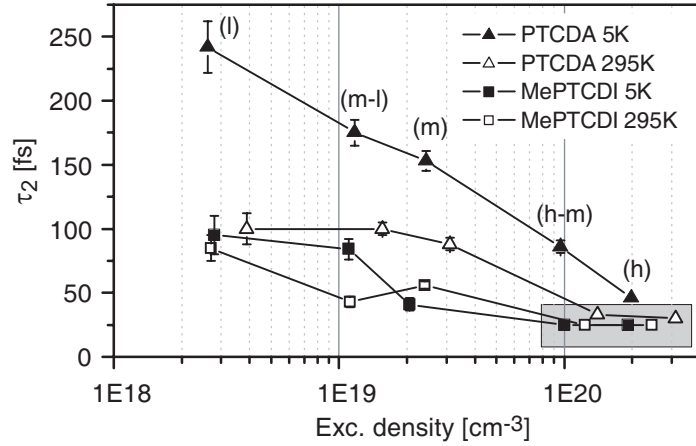


Figure 5.8.: $\Delta T/T$ (normalized) for a PTCDA thin film at 295 K (a) and at 5 K (b) with data for three different excitation intensities per temperature. The labels (h), (m), (l) symbolize “high” (open triangles), “moderate” (open circles) and “low” (solid squares) pump intensity, respectively. Their corresponding initial exciton densities are listed in Table 5.1. Data from Fig. 5.6 are repeated as open circles (m) at 295 K. For clarity, the curves have been shifted vertically by 0.25 each. Solid lines are fits, and the dashed line is the integrated cross-correlation. Note the different time axes.

Figure 5.9.: Same as in Fig. 5.8, but for a MePTCDI thin film. Data from Fig. 5.7 are repeated as open circles (m) at 295 K.

Figure 5.10.: Intraband relaxation time constants $\tau_{r,2}$ extracted from the fits to the data in Figs. 5.8 and 5.9. The gray rectangle highlights the range where the single exponential fit performs better. Labels (h),..., (l) are as in the previous figures (cf. Table 5.1) and apply to all four curves, from big $\tau_{r,2}$ to small $\tau_{r,2}$.



parallel to the integrated cross-correlation, at the limit of time resolution. Comparison of a certain exciton density in 5.8 (a) and (b) also demonstrates that a temperature increase accelerates the relaxation process.

As for the MePTCDI thin film, our exemplary curve in Fig. 5.7 revealed a faster intraband relaxation process than the one for PTCDA. This observation is also confirmed by Fig. 5.9, where the intensity and temperature dependence for MePTCDI is displayed. Moreover, intensity and temperature dependence valid for PTCDA are also confirmed by the MePTCDI measurements in Fig. 5.9, although they are less pronounced, especially the latter. Figure 5.10 displays the values of the intraband relaxation times for the two samples for the various initial exciton densities and temperatures. At the highest excitation densities, the rise of $|\Delta T/T|$ is at or close to the limit of time resolution and completely described by a single exponential behavior. In these cases, $S_1(t)$ has been used to fit the data. The corresponding range is highlighted in Fig. 5.10 by the gray rectangle. In all other cases the value of $\tau_{r,2}$ is displayed. Table 5.2 summarizes the values of the fit parameters $\tau_{r,1}$ and $\tau_{r,2}$ for the data points in Fig. 5.10.

The relaxation in k -space requires the emission of phonons. Converting the energy difference between the lowest absorbing and the emitting states of 40–45 meV (cf. Sect.

Table 5.2.: Values for the fit parameters for the data points in Fig. 5.10: If $S_1(t)$ is more appropriate, only one value ($\tau_{r,1}$) is given. If $S_2(t)$ is suited better, the combination of $\tau_{r,1}$ and $\tau_{r,2}$ is listed.

Sample	T [K]	Relaxation time constants $\tau_{r,1}$ [fs] or $\tau_{r,1} / \tau_{r,2}$ [fs]				
		(h)	(h-m)	(m)	(m-l)	(l)
PTCDA	295	29	30	2 / 88	2 / 100	2 / 100
PTCDA	5	2 / 46	2 / 86	2 / 153	3 / 175	2 / 242
MePTCDI	295	25	25	3 / 56	1 / 43	2 / 86
MePTCDI	5	25	25	21 / 41	7 / 85	2 / 95

2.3) in MePTCDI and PTCDA thin films to wavenumbers, this corresponds to values of 320–340 cm^{-1} . SCHOLZ et al. [29] and TENNE et al. [126] have addressed the vibronic properties in PTCDA thin epitaxial films and single crystals, respectively, using RAMAN spectroscopy. HASCHE et al. [108] have used ultrafast time-domain spectroscopy to investigate coherent phonon oscillations in thin films of MePTCDI. Despite the fact that in neither case phonons with the appropriate energy have been found, multiple other phonons with energies around 100 cm^{-1} [29, 108, 127] and relatively large RAMAN cross-section have been detected which could play a role in the relaxation process. Phonon emission can either be spontaneous or stimulated by phonons already present in the crystal. The fact of a faster relaxation at higher temperatures corresponds to increased stimulated phonon emission caused by higher thermal concentration of stimulating phonons. Higher excitation density will also cause a higher phonon concentration and thus leads to increased stimulated phonon emission. Hence, the trends in Figs. 5.8–5.10 can be well understood qualitatively.

As far as our limits of about ~ 250 fs and ~ 100 fs for the intraband relaxation time constant $\tau_{r,2}$ for the lowest excitation are concerned, it remains open whether these values are already the intrinsic low density limits. INO et al. [58] have reported upper and lower limits of 360 fs and 250 fs, respectively, for the relaxation time constant of the S_1 state in PTCDA at room temperature. However, they did not comment on the excitation densities used, and excitation took place into high-energy states of 5 eV, making the comparison somewhat difficult.

Long-time behavior and streak camera limit

Up to now, we have looked at the intraband relaxation process from two different viewpoints separately. Time-resolved photoluminescence has taught us about the arrival of excitons in the emitting states, and from excited state absorption in pump-probe we were able to estimate the duration of the relaxation process. In this paragraph, we create the overlap of the two measurement techniques by direct comparison of the individual results from PL and pump-probe.

Fig. 5.11 depicts again the time-resolved PL data from Sect. 5.1 as open squares in direct comparison with the pump-probe data from Figs. 5.8 and 5.9. This time, the data are displayed for a broad time range until 180 ps and with a logarithmic ordinate. Labels for all curves ($(h), \dots$) and exciton densities created by the pump pulse are the same as in the previous figures. At high intensities, the rapid decay is mainly governed by exciton-exciton interaction and annihilation, as we will see in the next chapter.

With decreasing pump intensity, the life time of the probed (pump-probe) state(s) drastically increases and approaches the intrinsic life time, which is determined by exciton recombination. As for the luminescence data, we have already noted in Sect. 5.1.1 that we have ensured the PL signal to depend linearly on the pump intensity, pointing towards the absence of exciton-exciton interaction. The density created in this case was $\sim 10^{17} \text{ cm}^{-3}$.

In Fig. 5.8 (a), the low-intensity limit for the PTCDA pump-probe data is depicted as (l) with solid squares, corresponding to an excitation density of $3.9 \times 10^{18} \text{ cm}^{-3}$, which is still one order of magnitude higher than for the streak camera measurement. Unfortunately, the signal-to-noise ratio did not allow to reach this limit. It can be seen that the low-intensity data (m) are superimposed by some modulation. Nevertheless, the PL data,

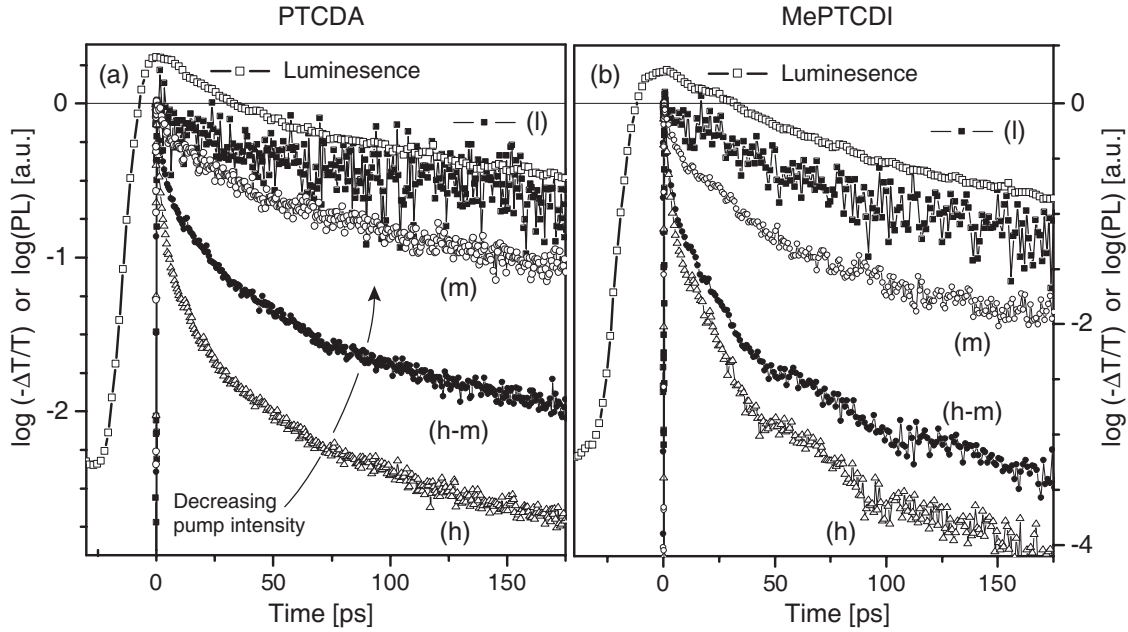


Figure 5.11.: Comparison of time-resolved photoluminescence (*open squares*) data from Fig. 5.1 with long-time pump-probe data on a logarithmic scale for various excitation intensities. Left (a) PTCDA thin film, right (b) MePTCDI thin film. All data are at room temperature. Symbols and corresponding labels are the same as Figs. 5.8 and 5.9, and initial exciton densities are as in Table 5.1. The PL curves have been shifted vertically by 0.3 to better distinguish them from the low-intensity pump-probe data (l). Note the different y coordinates indicating much faster decay in MePTCDI.

shifted upwards by 0.3, shows a temporal behavior and a life time which are very similar. In either case, the tail of the curves show a nearly linear decay, indicating the absence of exciton-exciton interaction. In the case of MePTCDI in Fig. 5.8 (b), this accordance between the PL data and the low-intensity pump-probe data (l) is even better, since both curves are essentially parallel¹¹.

The results indicate that with the low-intensity curves (l) we have reached the streak camera limit and *exciton-exciton interaction should be considered at densities higher than* $\sim 5 \times 10^{18} \text{ cm}^{-3}$. The second conclusion that we can draw is that upon basis of the data in Fig. 5.11, our state $|\psi^k\rangle$ monitored in pump-probe is *likely to be the emitting state*, $|\psi^\pi\rangle$. This would imply that the $\tau_{r,2}$ extracted from the ESA measurements are real intraband relaxation times and not only upper limits. However, an irrefutable statement about the nature of $|\psi^k\rangle$ is unfortunately not possible from the time dependence of the ESA signal alone.

¹¹The suspicious modulations at high densities (h) and (h-m) are no artifacts. They stem from a collective excitation of the whole film. Due to local heating effects, an acoustic shock wave forms and propagates in the film, changing the mass density. This alters the optical response of the probed region. This effect has been well understood for thin films of phthalocyanines [128].

5.2.3. Pump-probe anisotropy

In Sect. 5.1.2, we have employed luminescence anisotropy to obtain supplementary information about our model systems, and we found a convincing accordance of our anisotropy model with the experimental results. It is therefore obvious to also determine the pump-probe anisotropy and to compare it to the PL anisotropy. This means that we will readopt our formalism of DAVYDOV-split doublets $|\psi_{\pm}^0\rangle$ populated upon excitation by the pump beam, and we will also consider DAVYDOV-split band states $|\psi_{\pm}^k\rangle$.

Experimentally, the $\Delta T/T$ signal was measured simultaneously for mutually parallel and perpendicular probe polarization. This was accomplished by insertion of a broadband half wave plate ($\lambda/2$) tilting the probe beam polarization by 45° with respect to the pump polarization. A polarizing beam splitter placed behind the sample separated both probe polarizations, which were then recorded by individual auto-balanced photodetectors as described in Sect. 3.4.1. As in the streak camera measurements, we have verified that the samples did not show anisotropic behavior which might be caused by intense excitation. This was done by measurements of the time-integrated polarization-dependent luminescence at the pump-probe setup.

Figure 5.12 shows again the pump-probe data on a long time scale for excitation density (m) from Fig. 5.11, symbolized by open circles, for MePTCDI (left) and PTCDA (right). The perpendicular counterparts are displayed with solid circles. In the two lower panels, the pump-probe anisotropies as computed by Eq. (5.1) are depicted. In contrast to the luminescence anisotropies shown in Fig. 5.4, two major differences can be identified. Not only are the pump-probe anisotropies for both materials astonishingly similar, but also for the anisotropy of PTCDA $r \neq 0$ holds, which is in clear contradiction to the PL results. The easiest guess that this unexpected result may be attributed to an experimental error or artifact can be refuted by our observation that other thin films of PTCDA reproducibly show the same behavior. Moreover, the time dependence of the pump-probe anisotropies in Fig. 5.12 proves that this effect cannot be explained by a mere calibration error of the two polarization channels¹².

The particular difficulty in the analysis of this open issue is the lack of information about the target states and the probed transition dipole moments in pump-probe. In luminescence, the final states $|\chi_{\pm}\rangle$ and the dipole moments $\boldsymbol{\mu}_{ij}$ (where $i, j = (+, -)$), for emission are known. As for excited state absorption of a thin film, however, neither of them are really known, and the quantum-chemical calculations on an isolated dimer can only provide limited information.

We now consider the most obvious case of DAVYDOV-split higher excited states $|\phi_{\pm}^k\rangle$ the probe pulse excites into from the probed state $|\psi_{\pm}^k\rangle$. Then, the (2D) treatment can be done in full analogy to luminescence anisotropy, as sketched in Fig. 5.2, with transition dipole moments $\boldsymbol{\mu}'_{ij}$ ($i, j = (+, -)$) for the $S_1 \rightarrow S_n$ transition. We do not make an a priori statement about their actual orientation. From symmetry arguments, our only justified assumption is that as in luminescence the ratio of the $\boldsymbol{\mu}'$ is given by

$$\xi = \left| \boldsymbol{\mu}'_{+-} \right| / \left| \boldsymbol{\mu}'_{++} \right|. \quad (5.31)$$

¹²Without displaying all data, we note that also the data for other excitation densities (h),... show the same behavior. The effect is thus independent of the excitation density.

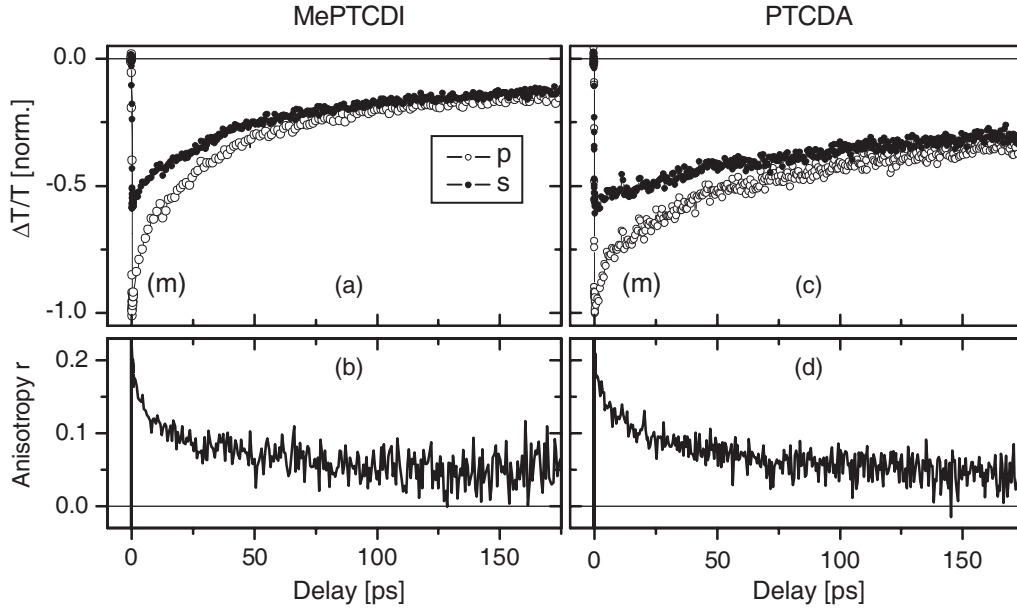


Figure 5.12.: Polarization-dependent pump-probe measurements and the resulting pump-probe anisotropies for MePTCDI (a,b) and PTCDA (c,d). “p” and “s” denote mutually parallel and perpendicular polarization of pump and probe beam, respectively. Parallel data (open circles) are the same as (m) from Fig. 5.11. The perpendicular curve was recorded simultaneously at the same excitation density.

If $\boldsymbol{\mu}' \parallel \boldsymbol{\mu}$, we immediately get the same result as in Eq. (5.17), independent of whether the populations of $|\psi_{\pm}^k\rangle$ are equilibrated. Thus, for PTCDA, where $\xi \approx 0.9$, $r_{2D} = \tilde{r}_{2D} \approx 0$ is also expected for the pump-probe anisotropy. Assuming the other extreme of transition dipole moments $\boldsymbol{\mu}' \perp \boldsymbol{\mu}$, we obtain for the 2D anisotropy

$$r_{2D,\perp}(\xi) = \frac{-2 + 4\xi^2 - 2\xi^4}{7 + 10\xi^2 + 7\xi^4}, \quad (5.32)$$

and again, this compacts to $r_{2D} = \tilde{r}_{2D} = 0$, if $\xi = 1$. Hence, *regardless* of the mutual orientation of $\boldsymbol{\mu}$ and $\boldsymbol{\mu}'$, in PTCDA one expects $r_{2D} \approx 0$ for any two states $|\psi_{\pm}^k\rangle, |\phi_{\pm}^k\rangle$ that show DAVYDOV splitting.

The experimental fact that $r(0) \approx 0.2$ in PTCDA suggests that this contradiction may be resolved solely by additional states that are not DAVYDOV-split. This is only possible if one drops the concept of interaction between inequivalent stacks. Treatment of the question in this *oriented gas model* of non-interacting stacks would allow to explain values of $r_{2D} = 0.4$ (probed dipole \parallel pumped dipole) or $r_{2D} = -2/7$ (probed dipole \perp pumped dipole) or in between (mixture of transitions)¹³. However, the oriented gas model clearly fails with the interpretation of the proven luminescence anisotropy for PTCDA and MePTCDI.

¹³The value of $-2/7$, following from Eq. (5.32) for the limiting case $\xi = 0$, is due to the 2D treatment. In 3D treatment, of course, we obtain $-2/5$ as predicted by Eq. (4.4).

Another loophole would be the assumption of *completely* different states in pump-probe and luminescence. For example, the pump-probe state $|\psi_{\pm}^k\rangle$ might be a precursor of the emitting state $|\psi_{\pm}^{\pi}\rangle$. This is extremely unlikely because the temporal behavior of the low-intensity limit (1) of $\Delta T/T$ and the luminescence signal are almost identical, requiring $|\psi_{\pm}^{\pi}\rangle$ to be very short-lived, in clear contradiction to the theoretically expected lifetime for an indirect emission process in luminescence [40]. An alternative idea might be an absorbing state $|\psi_{\pm}^0\rangle$ being actually depopulated via two completely different channels towards $|\psi^k\rangle$ and $|\psi_{\pm}^{\pi}\rangle$. In this case, $|\psi^k\rangle$ ought not to be DAVYDOV-split (in puzzling contrast to $|\psi_{\pm}^0\rangle$ and $|\psi_{\pm}^{\pi}\rangle$), and the transition dipole moment for ESA ought to have identical orientations in MePTCDI and PTCDA, requiring an additional short-axis polarized dipole to obtain $r(0) \approx 0.2$. Moreover, the two depopulation rates of $|\psi_{\pm}^0\rangle$ should essentially be identical. The question concerning the expected ESA contribution from the DAVYDOV-split emitting state remains open. This construction seems utmost artificial. We therefore conclude this section with the remark that a full understanding of the pump-probe anisotropy requires a much deeper understanding the states and transition dipole moments involved in excited state absorption than currently available. However, this is only possible with extended experimental efforts and in close combination with more sophisticated quantum-chemical calculations.

Although not all questions raised in this chapter could be fully answered, we now summarize the findings of ultrafast intraband relaxation. Using excited state absorption, we were able to time-resolve the intraband relaxation process from the Γ -point to the border of the Brillouin zone in thin films of MePTCDI and PTCDA. For moderate excitation densities on the order of 10^{19} cm^{-3} , this process happens on a ~ 60 fs (MePTCDI) and ~ 90 fs time scale (PTCDA). Intraband relaxation is accompanied by stimulated emission of phonons. Reducing the number of phonons available by decreasing the pump intensity and/or the temperature proved to slow down the relaxation process. We also tentatively conclude that the probed state in ESA is the emitting state. From the viewpoint of time-resolved luminescence, the rise time of the signal is in accordance with the upper limit of the ESA measurements. The experimental results for the different luminescence anisotropies in MePTCDI and PTCDA were in full accordance with the predictions made by a luminescence anisotropy model being in full consistence with the exciton model of DAVYDOV-split states.

6. Exciton-exciton interaction and annihilation at high excitation densities

Up to now, we have considered excitons only as “isolated” (quasi-)particles being well separated in space and contributing independently to the total transient transmittance signal. Yet, the strong dependence of the excited state absorption signal on excitation intensity observed in Sect. 5.2.2 demonstrates that exciton-exciton interaction can not be neglected in high excitation regimes. In this chapter, we want to quantify this intensity dependence, using three different models to describe the annihilation process. We will present these models in Sect. 6.1 and apply them to our ESA data in Sect. 6.2. For both room and liquid helium temperature, we will extract annihilation rates, diffusion constants, annihilation radii, and diffusion lengths.

6.1. Annihilation models

6.1.1. Introduction

The comparison of pump-probe traces at various excitation densities in Fig. 5.11 on a logarithmic scale indicated that for initial exciton densities higher than $5 \times 10^{18} \text{ cm}^{-3}$, a nonlinear decay of the transient transmittance $\log(-\Delta T/T)$ becomes apparent. This implies that the $\Delta T/T$ signal does not decay with a single exponential unless we have reached the low-density limit (1)¹. Deviations from single exponential behavior imply that multiple concurrent relaxation processes contribute to the signal.

Here, we separate the de-excitation by annihilation from intrinsic exciton recombination. The latter might itself be accomplished by various relaxation channels, such as radiative and nonradiative recombination². These channels are in the following substituted by one single effective channel with a generalized life time τ . Then, the general rate equation for the population n of the probed first excited state can be written as:

$$\frac{d}{dt} n(t) = -\frac{n(t)}{\tau} - f \gamma n(t)^2. \quad (6.1)$$

Here, the first term on the right hand side stands for the generalized population change in the low-density limit decaying with the single-exciton rate $1/\tau$. The second term is due to the bimolecular annihilation process and therefore scales with the square of $n(t)$. The annihilation rate “constant” γ may actually be time-dependent, as we will see further below. Usually, the additional coefficient f appears explicitly in the rate equation Eq. (6.1), indicating the type of the annihilation reaction.

¹As in the previous chapter, we keep the uniform labels (h), . . . , (l). Values are given in Table 5.1.

²This is definitely the case for MePTCDI and PTCDAs thin films.

First, we consider the reaction $S_1+S_1 \rightarrow X+S_0$, with S_0 being the ground state, S_1 the first excited singlet state, and X a higher excited state. If no exciton remains after bimolecular annihilation, $f = 1$. This case applies, e. g., if the excitons dissociate to create an ionized state, which is typically assumed in the early works on molecular crystals [129]. If, however, the annihilation of a pair leaves one exciton behind after an intermediate step ($S_1+S_1 \rightarrow S_n+S_0 \rightarrow S_1+S_0$), $f = \frac{1}{2}$. In the literature, the discussion about the actual value of f is often only touched or even completely omitted. Mostly, f is considered to be $\frac{1}{2}$ without any further discussion. In any case, the maximum error in the determination of the annihilation rate constant γ due to the parameter f is a factor of 2, since $\frac{1}{2} \leq f \leq 1$.

When deriving the second term in Eq. (6.1), the common procedure is to regard excitons as mobile particles and to solve the diffusion equation under given constraints to obtain $n(x, t)$. Changes of the particle density are expressed by a current of ΔN particles per unit time Δt normal through a given surface A :

$$\mathbf{j}_N = \frac{\Delta N}{\Delta t} \frac{1}{A} \mathbf{e}_A = -D \nabla n(x, t), \quad (6.2)$$

with diffusion constant D . The solution to γ is then related to finding an appropriate expression for $\nabla n(x, t)$. In the following subsections, we discuss three different microscopic models for exciton-exciton annihilation: three-dimensional diffusion, one-dimensional diffusion, and annihilation via a single-step FÖRSTER transfer.

6.1.2. Three-dimensional annihilation

In the simplest case, excitons are assumed to be particles with isotropic diffusion constant D_{3D} , which annihilate if a pair comes closer than a critical distance \bar{a} . This distance corresponds to an average 3D-lattice constant. An approximate solution was already given for the equivalent problem of coagulating particles by SMOLUCHOWSKI [130] and reviewed in [131]

$$\gamma_{3D} = 8\pi D_{3D} \bar{a} \left(1 + \frac{\bar{a}}{\sqrt{2D_{3D}\pi t}} \right). \quad (6.3)$$

We briefly sketch the derivation of Eq. (6.3) to be able to translate the ideas to the single-step mechanism in Sect. 6.1.4. The derivation is based on the related problem of particle capture by an immobile trap. Assuming an interaction distance \bar{a} and an initially uniform exciton concentration n_0 , the diffusion problem around the spherical quenching sphere of a single trap can be exactly solved and gives for the exciton current into the trap (see, e. g., [132]):

$$|\mathbf{j}_N| = \gamma_{T,3D} \cdot n_0, \quad (6.4)$$

with the trapping rate constant

$$\gamma_{T,3D} = 4\pi D_{3D} \bar{a} \left(1 + \frac{\bar{a}}{\sqrt{D_{3D}\pi t}} \right). \quad (6.5)$$

We now consider a volume V containing N excitons and N_T non-interacting traps. Let the corresponding densities be $n = N/V$ and $n_T = N_T/V$. Then, the exciton number changes according to $\dot{N} = -N_T|\dot{j}_N|$, leading to an average exciton density:

$$\frac{d}{dt} n = -\gamma_{T,3D} \cdot n_0 \cdot n_T . \quad (6.6)$$

This rate equation describes the diffusion of excitons driven by the concentration gradient ∇n between the inner boundary given by the trap-surface ($n(\bar{a}) = 0$) and the outer boundary given by the undisturbed region far away ($n(r \rightarrow \infty) = n_0$). If additional processes change the concentration at the outer boundary, n_0 should be replaced by its actual value. It can thus be approximated by the average concentration n , and Eq. (6.6) becomes:

$$\frac{d}{dt} n = -\gamma_{T,3D} \cdot n \cdot n_T . \quad (6.7)$$

The rate law (6.7) for the trapping problem can easily be applied to bimolecular annihilation. Then, each exciton acts as a trap and $n_T = n$. In addition, the rate constant $\gamma_{T,3D}$ for the particle current into the trap has to be modified, since now the trap is mobile, too. As the relative motion of two diffusing particles can be described by an effective diffusion constant $D_{\text{eff}} = D_{3D} + D_{3D}$ [130, 131], the rate constant $\gamma_{T,3D}$ becomes γ_{3D} as given in Eq. (6.3)³.

The t -dependence of the annihilation constant arises from the fact that proximate excitons, or excitons closest to traps, will interact first. Progressively greater inter-particle distances result in decreasing annihilation rates. In many cases, the rate constant γ_{3D} is even considered only for time scales $t \gg \bar{a}^2/(2D_{3D}\pi)$. Using the nearest neighbor hopping time $t_H = \bar{a}^2/(6D_{3D})$, this corresponds to $t \gg t_H$. At such time scales, the transient term in Eq. (6.3) can be neglected and the rate constant takes the simple, time-independent form $\gamma_{3D} = 8\pi D_{3D}\bar{a}$.

6.1.3. One-dimensional annihilation

Although we do not make an a priori statement about the dimensionality of the diffusion process, the above premise of an isotropic diffusion constant D_{3D} seems somewhat unlikely in a highly anisotropic molecular crystal, such as PTCDA and MePTCDI. SUNA [133] has pointed out that the rate constants for diffusion-controlled reactions in molecular crystals strongly depend on the dimensionality of the system. For the one-dimensional case, the rate constant for bimolecular annihilation is given by (see, e. g., [134]):

$$\gamma_{1D} = \frac{1}{aN_0} \sqrt{\frac{8D_{1D}}{\pi t}} , \quad (6.8)$$

³We note that this scenario actually refers to an annihilation reaction $S_1+S_1 \rightarrow X+S_0$, where both excitons are destroyed, i. e., $f = 1$. One might think at first glance that use of the trapping rate law implies a survival of one exciton (the trap). However, the annihilation of the trap is included by the fact that the concentration n of “excitons falling into traps” refers to all excitons and thereby includes the “excitons acting as traps”.

with a being the 1D-lattice constant, D_{1D} the diffusion constant along the considered direction, and N_0 the 3D molecular density.

The rate constant γ_{1D} in Eq. (6.8) can be retrieved from the one-dimensional diffusion problem for a semi-infinite slab. Let the initial population be constant ($n(x, t = 0) = n_0$), and let there be a perfect sink at the surface of the slab, i. e., $n(x = 0, t) = 0$. The exciton current density into the sink is then given by $\sqrt{D_{1D}/(\pi t)}$ [135]. If we treat the 3D molecular crystal as a system of 1D stacks with a trapping site density n_T , the treatment can be done analogously to the 3D case in Eq. (6.7), and we obtain:

$$\frac{d}{dt} n = -\gamma_{T,1D} \cdot n \cdot n_T. \quad (6.9)$$

Here, the annihilation rate constant is

$$\gamma_{T,1D} = \frac{1}{aN_0} \sqrt{\frac{4D_{1D}}{\pi t}}. \quad (6.10)$$

Similar to the 3D case, the transition towards the annihilation problem is done by taking $n_T = n$ and by using the effective diffusion constant $D_{\text{eff}} = D_{1D} + D_{1D}$ in the rate constant $\gamma_{T,1D}$, arriving at the annihilation rate constant γ_{1D} in Eq. (6.8). In remarkable contrast to the 3D diffusion problem, the 1D rate constant γ_{1D} does not approach a finite value for large t . Thus, the dynamics in 1D will be significantly different from the 3D case.

6.1.4. Förster-type interaction and annihilation

The two diffusion models discussed so far assume that the excitons diffuse sufficiently rapid in many steps of the type $S_1 + S_0 \rightarrow S_0 + S_1$ towards each other, until they annihilate via a short range interaction in a final step of the type $S_1 + S_1 \rightarrow X + S_0$. As an alternative model, we now discuss the case that annihilation occurs without exciton diffusion and just by a single, long-range annihilation step.

As seen in Figs. 4.8 and 4.9, both PTCDA and MePTCDI show strong photoinduced absorption in the range between 1.7–2.0 eV. This allows for good spectral overlap with the photoluminescence (shown in Fig. 5.1), peaking around 1.80 eV. Thus, efficient FÖRSTER type energy transfer with a large FÖRSTER radius R_F can be expected for the annihilation step $S_1 + S_1 \rightarrow S_n + S_0$, with S_n being the state the probe pulse excites into in the excited state absorption experiments.

To derive a rate law for such a single-step annihilation mechanism, we start again with the trapping problem. FÖRSTER [136] considered a model in which a donor molecule is surrounded by a statistic distribution of acceptor molecules with volume density n_T . For a single donor molecule, the decay rate follows from a summation of the intrinsic decay rate $1/\tau$ and all energy transfer rates to the surrounding acceptor molecules. Averaging over all distributions of donor molecules leads to the time-dependent exciton population on the donor molecules [136]:

$$n(t) = n_0 \exp\left(-\frac{t}{\tau} - \frac{4}{3}\pi R_F^3 \sqrt{\frac{\pi t}{\tau}} n_T\right). \quad (6.11)$$

Derivation with respect to t yields a rate equation

$$\frac{d}{dt} n = -\frac{n}{\tau} - \gamma_F \cdot n \cdot n_T, \quad (6.12)$$

with a rate constant

$$\gamma_F = \frac{2}{3} \pi R_F^3 \sqrt{\frac{\pi}{\tau t}}. \quad (6.13)$$

This formalism is used to discuss luminescence quenching experiments in molecular crystals with an acceptor (quencher) concentration n_T [137]. For application to annihilation experiments, we identify $n_T = n$ as in the diffusion problem and arrive at a rate law of the general form of Eq. (6.1), with an annihilation constant γ_F . The rate constant γ_F for the single-step annihilation mechanism is (apart from the role of τ) structurally equivalent to the rate constant for the 1D diffusion model, as both share a $t^{-1/2}$ dependence.

6.2. Application of annihilation models

In this section, we turn towards the application of all three annihilation models to our pump-probe data in order to identify the most appropriate annihilation process. Initially, the experimental conditions are briefly recapitulated: Thin films of PTCDA and MePTCDI with 25 nm and 35 nm thickness were excited resonantly into the lowest excited S_1 state using 25 fs pump pulses, centered around 2.22 eV for PTCDA and 2.16 eV for MePTCDI. The probe pulses were shaped by the AOPDF (Sect. 3.3.3) with a Gaussian spectral envelope centered around 1.94 eV and a FWHM of 100 meV. Because both PTCDA and MePTCDI show strong photoinduced absorption in this range (Sect. 4.3), we were able to monitor the populations in the S_1 manifold by means of excited state absorption. Measurements have been performed at room and liquid helium temperature over a wide range of excitation densities. Figure 5.11 has already presented the room-temperature data on a long time range for both PTCDA and MePTCDI. The data for 5 K will be presented together with the fits in the following section Sect. 6.2.1. Values for the annihilation constants, diffusion constants, diffusion lengths, and FÖRSTER radii will then be summarized later in Sect. 6.2.2.

6.2.1. Fits to experimental data

We have solved the rate equation Eq. (6.1) with the different annihilation constants γ_i from Eqs. (6.3),(6.8),(6.13). The coefficient f in Eq. (6.1) has been chosen to be $f = \frac{1}{2}$, assuming an annihilation reaction $S_1 + S_1 \rightarrow S_n + S_0 \rightarrow S_1 + S_0$, which implies that the ionization of the higher excited S_n state plays only a marginal role.

The results for the exciton density $n(t)$ are as follows: For the 3D diffusion model, we obtain

$$n_{3D}(t) = n_0 e^{-t/\tau} \left[1 + c' \left(\frac{\sqrt{2D_{3D}\tau}}{\bar{a}} (1 - e^{-t/\tau}) + \operatorname{erf} \left(\sqrt{\frac{t}{\tau}} \right) \right) \right]^{-1}, \quad (6.14)$$

with the abbreviation $c' = 4\pi n_0 \bar{a}^2 \sqrt{D_{3D}\tau/2}$. The error function “erf” has already been defined in Eq. (5.27). For the 3D mean lattice constants, we derive $\bar{a}_P = 7.24 \text{ \AA}$ for PTCDA [24] and $\bar{a}_M = 7.57 \text{ \AA}$ for MePTCDI [14] from the crystal structures. Since we cannot detect $n(t)$ directly, we have to establish the link to the detected signals $|\Delta T/T(t)|$. For that purpose, we have used a detection efficiency factor $\eta = |\Delta T/T|/n$ mapping exciton densities to signals. This factor can be determined from the initial density $n_0 = n(t=0)$ which can be estimated using Eq. (3.50)⁴.

The low-density life times τ were extracted from linear fits to the tails of the low-intensity pump-probe data $\log(-\Delta T/T)$. For room temperature, these data are shown in Fig. 5.11 (label “(1)”). Yet, the rather noisy signal at this excitation density resulted in broad ranges of possible values for τ . The most trustworthy values τ_{opt} were $\tau_{P,5K} = 5.7 \text{ ns}$ and $\tau_{P,295K} = 470 \text{ ps}$ for PTCDA, and for MePTCDI $\tau_{M,5K} = 3.3 \text{ ns}$ and $\tau_{M,295K} = 235 \text{ ps}$. Fits with the annihilation model from Eq. (6.14) were performed for distinct (i. e., fixed during the fitting procedure) values of the different τ_i . The error bars of the fit parameters were estimated using estimated error bars for the τ_i ⁵. Hence, only one parameter, the diffusion coefficient D , was fit at a time, making the fits more reliable.

The solutions for the 1D diffusion annihilation model and for the single-step FÖRSTER-type annihilation model are:

$$n_{1D}(t) = n_0 e^{-t/\tau} \left[1 + \frac{n_0}{aN_0} \sqrt{2D_{1D}\tau} \operatorname{erf}\left(\sqrt{\frac{t}{\tau}}\right) \right]^{-1}. \quad (6.15)$$

$$n_F(t) = n_0 e^{-t/\tau} \left[1 + \frac{1}{3}\pi^2 n_0 R_F^3 \operatorname{erf}\left(\sqrt{\frac{t}{\tau}}\right) \right]^{-1}. \quad (6.16)$$

The distance a of adjacent molecules is the 1D lattice constant, i. e., $a_P = 3.72 \text{ \AA}$ for PTCDA and $a_M = 3.87 \text{ \AA}$ for MePTCDI. The respective 3D molecular densities are $N_{0,P} = 2.64 \times 10^{21} \text{ cm}^{-3}$ and $N_{0,M} = 2.30 \times 10^{21} \text{ cm}^{-3}$. The fit parameters were D_{1D} for the 1D model and R_F for the FÖRSTER model. In all cases, the same values for the life times τ_i as for the 3D model have been employed.

The apparent similarity between the 1D diffusion-limited process and static annihilation via FÖRSTER interaction has already been pointed out early [129, 133], which is frequently mentioned in the literature. Yet, the discussion usually remains limited to extracting values for γ_F or γ_{1D} only. In this work, we perform a more detailed analysis and actually provide values for the diffusion constants D and the FÖRSTER radius R_F .

PTCDA Figure 6.1 again depicts the pump-probe ESA data for high (h) and moderate (m) excitation densities (cf. Table 5.1 and Sect. 5.2.2) for room temperature as in Fig. 5.11, together with the best fit curves for all three annihilation models. The vertical scale of the panels (a) and (b) has been adjusted to match best the range of the individual curves. Low-temperature data is presented in Fig. 6.2. In all four cases, the fit curves for the 1D-diffusion limited process are in striking agreement with the experimental data. As

⁴Our treatment implies that the population is generated instantly by a single pump pulse at $t = 0$.

⁵These error bars were rather large: $\tau_{\text{max}} \approx \tau_{\text{opt}} \times 1.45$, $\tau_{\text{min}} \approx \tau_{\text{opt}} \times 0.65$.

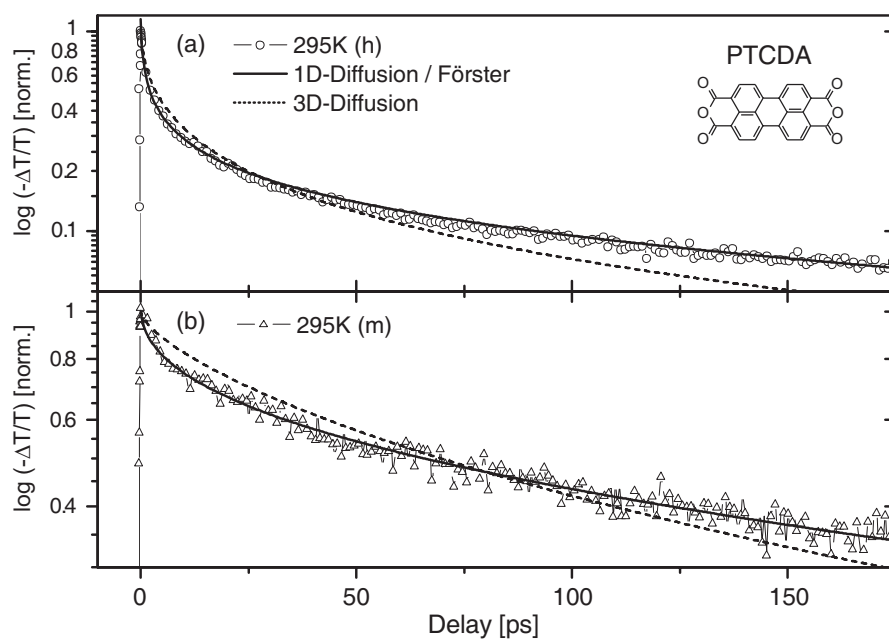


Figure 6.1.: Fits to pump-probe ESA data from a PTCDA thin film at room temperature at high (h),(a) and moderate (m),(b) excitation densities. The fit curves have been calculated as defined by Eq. (6.15) for 1D diffusion annihilation and by Eq. (6.14) for 3D diffusion annihilation. Fit curves for the single-step FÖRSTER model after Eq. (6.16) coincide with curves for 1D annihilation. Results are displayed for the best fits. Excitation densities are as in Table 5.1.

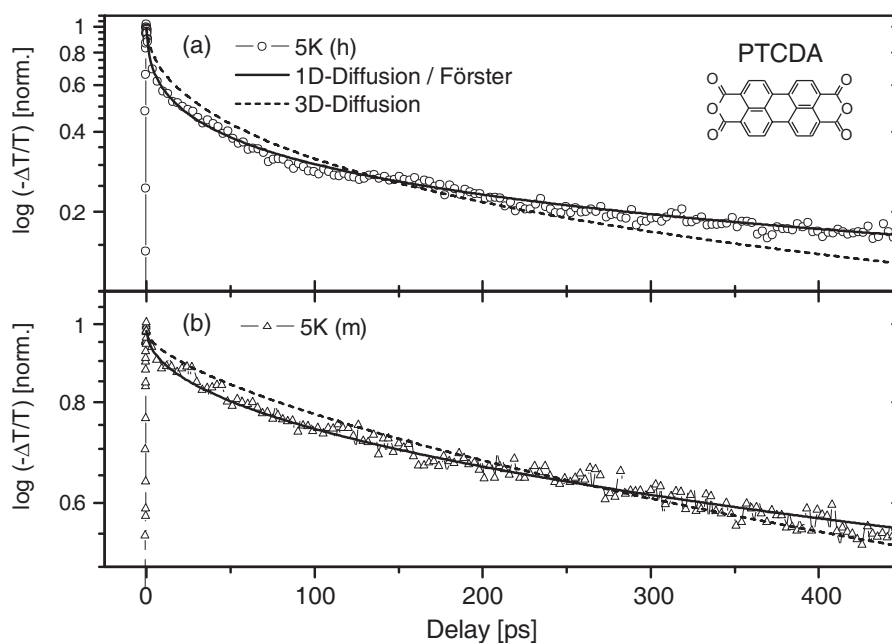


Figure 6.2.: As in Fig. 6.1, but at 5K, again for high (h),(a) and moderate (m),(b) excitation densities. Again, curves for the 1D and the FÖRSTER model coincide.

6. Exciton-exciton interaction and annihilation at high excitation densities

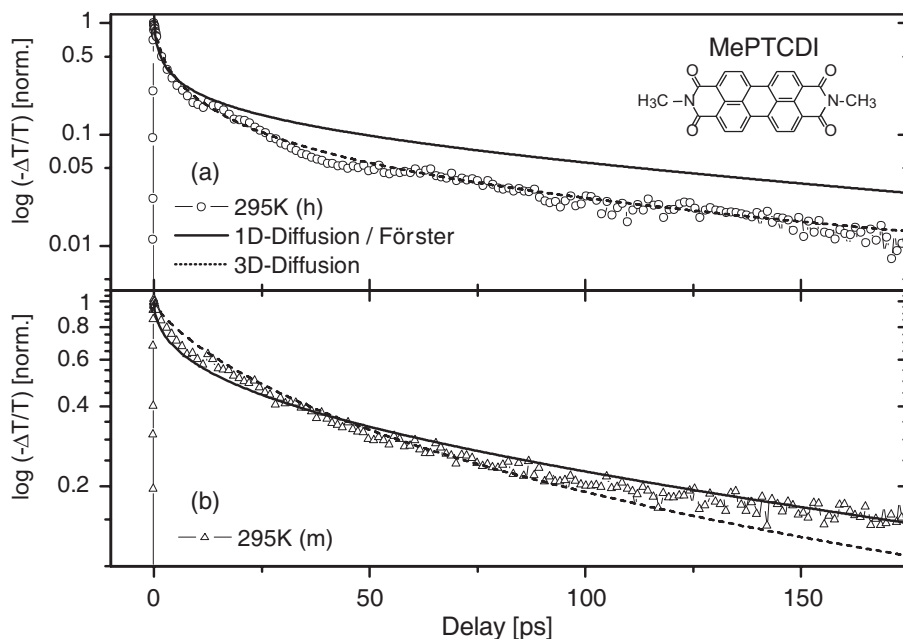


Figure 6.3.: Fits to pump-probe ESA data from a MePTCDI thin film at room temperature at high (h),(a) and moderate (m),(b) excitation densities. The fit curves have been calculated as defined by Eq. (6.15) for 1D diffusion annihilation and by Eq. (6.14) for 3D diffusion annihilation. Fit curves for the single-step FÖRSTER model after Eq. (6.16) coincide with curves for 1D annihilation. Results are displayed for the best fits. Excitation densities are as in Table 5.1.

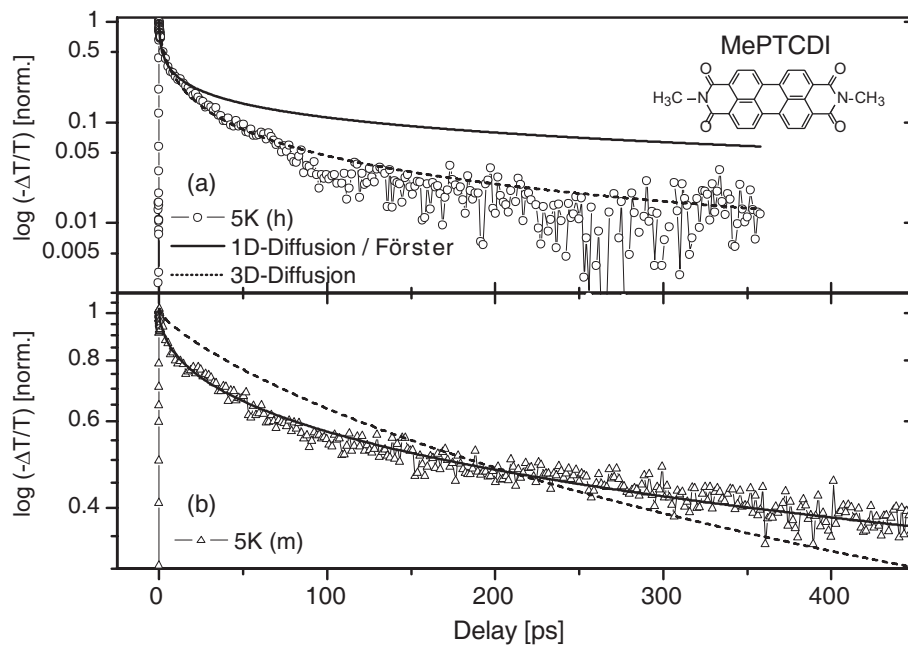


Figure 6.4.: As in Fig. 6.3, but at 5K, again for high (h),(a) and moderate (m),(b) excitation densities. Again, curves for the 1D and the FÖRSTER model coincide.

expected from the same structure and the same $t^{-1/2}$ dependence of the annihilation constants γ_{1D} and γ_F , this also applies to the FÖRSTER single-step model – the curves actually coincide. We emphasize that we have also fit the models to the curves for the two remaining excitation densities (h-m) and (m-l) (cf. Table 5.1) at room temperature and achieved fits of as high quality as in Figs. 6.1 and 6.2.

In contrast, the 3D-diffusion model shows clear discrepancies in all cases. Still, when the parameter \bar{a} is no longer kept constant in the fitting process for the 3D diffusion model, it is in fact possible to obtain fits from Eq. (6.14) also for the 3D model being in good agreement with the data. However, this results in rather unphysical values of $\bar{a} \approx 20 \text{ \AA}$, large compared to the actual lattice constants.

We interpret our results as an evidence that – in case that we consider a diffusion-limited process – *exciton transport in PTCDA thin films is primarily one-dimensional, along the stacking direction*. However, it is as just to conclude that exciton annihilation might be due to a single-step FÖRSTER-type annihilation process⁶.

MePTCDI Figures 6.3 and 6.4 depict the ESA data for MePTCDI thin films at high (h) (panel (a)) and moderate (m) (panel (b)) excitation densities for room temperature and low temperature, respectively. As above, the fits with the 1D diffusion model for moderate excitation densities (m) are in very good agreement with the experimental data. Of course, this also applies to the single-step FÖRSTER model, as the curves coincide again. The 3D model in these cases is clearly inferior. However, the situation drastically changes when we look at the high excitation (h) density data in Figs. 6.3 (a) and 6.4 (a). There, the 1D model and the FÖRSTER model completely fail, whereas the 3D diffusion model describes the data very convincingly. As far as the two intermediate excitation densities (h-m) and (m-l) (cf. Table 5.1) are concerned, we note that for the excitation density (m-l) only the 1D and the FÖRSTER model are in clear accordance with the data. For density (h-m) all fits are of similar mediocre quality, but with slight advantages in favor of the 3D model.

If we again consider a diffusion-limited process, our results indicate that *at not too high excitation densities (m), exciton transport in MePTCDI thin films is also one-dimensional, along the stacking direction*, just as in PTCDA. Yet, with increasing exciton density the transport is described much better by a 3D diffusion model. Hence, not only does the question arise which process is responsible for the change of the transport properties. Since our quasi-1D samples have a high intrinsic anisotropy, it is also interesting how such a 3D transport in a stacked environment should look like⁷.

In the similar columnar materials class of phthalocyanines, evidence for hopping between adjacent stacks has been found [139]⁸, which could increase the dimensionality of the system. Theoretical models of 1D diffusion with escape by inter-stack hopping [140]

⁶It should be noted that decay kinetics described by a $t^{-1/2}$ -dependence could also be due to exciton trapping by impurities in the crystalline structure (cf. Eq. (6.9)). Then, the decay rate should depend linearly on the initial exciton density. The nonlinear dependence of the decay rate (best seen in Fig. 5.11) on excitation intensity shows that this is not the case for PTCDA (and also MePTCDI).

⁷We would assume 3D transport rather in isotropic material, as shown, e. g., in the amorphous Alq₃ (tris(8-hydroxyquinoline) aluminum) [138].

⁸In triplet-triplet exciton annihilation.

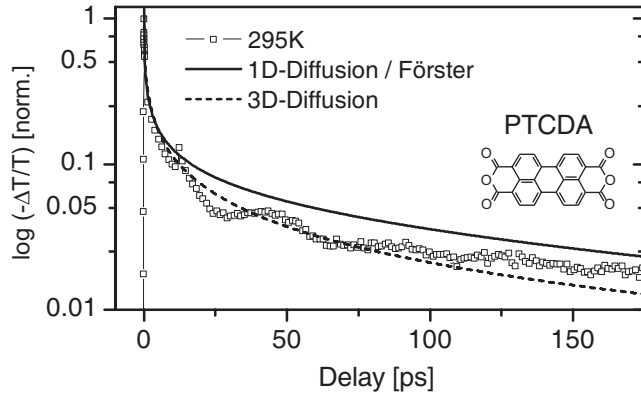


Figure 6.5.: Fits to pump-probe ESA data for a PTCDA thin film at room temperature as in Fig. 6.1, but with an excitation density of $1.4 \times 10^{21} \text{ cm}^{-3}$. The oscillation is attributed to a collective excitation of the film as noted on page 81 for MePTCDI [128].

have confirmed that even if they happen infrequently, these hops can affect the decay kinetics, especially at longer times. If we examine Figs. 6.3 (a) and 6.4 (a), it might be possible that this hopping process is effective after some 25 ps.

We should therefore estimate the inter-stack coupling in MePTCDI compared to PTCDA, where the 3D model is not appropriate. Intuitively, one might think that the mutual orientation of the two stacks in MePTCDI (cf. Fig. 2.6, where the unit cells are depicted) under only a small angle favors inter-stack coupling in contrast to the PTCDA crystal with its herringbone-like orientation of stacks. However, in the first approximation the inter-stack coupling in MePTCDI and PTCDA is in fact of similar strength⁹. Moreover, similar coupling strength can also be inferred from the observation that the DAVYDOV-splitting is on same order of magnitude [23, 48]. Hence, the mere assumption of a preferred inter-stack hopping in MePTCDI *alone* does not completely resolve the open issue, although it might play a small role.

Figure 6.5 shows fits to pump-probe data from a PTCDA thin film at room temperature, as in Fig. 6.1, but at an excitation density of $1.4 \times 10^{21} \text{ cm}^{-3}$, 4.5 times higher than for the curve (h) in Fig. 6.1 (a). Interestingly, the 3D diffusion model now performs significantly better than the 1D diffusion/single-step FÖRSTER model, comparable to the MePTCDI examples at high intensities (h) above. Hence, for a given excitation density n_0 , relaxation processes in PTCDA happen with a relaxation rate being achievable in MePTCDI using excitation densities of almost one order of magnitude lower.

For the annihilation reaction $S_1 + S_1 \rightarrow S_n + S_0 \rightarrow S_1 + S_0$, it is generally assumed that the higher excited S_n state loses its energy by vibronic (phononic) relaxation. We therefore tentatively conclude *that the cross sections for phononic relaxation in MePTCDI are significantly larger than in PTCDA*. The accelerated intraband relaxation processes in MePTCDI in Sect. 5.2.2 point in the same direction. For a complete understanding and resolution of this problem, however, enhanced models and additional theoretical efforts are required, which are beyond the scope of this thesis. As far as the data at high excitation intensities are concerned, our models in Eqs. (6.14–6.16) are certainly limited.

⁹The matrix-element between nonequivalent molecules in the unit cell in point dipole approximation is 5.83 meV for MePTCDI and 3.89 meV for PTCDA, calculated by HOFFMANN after [100].

6.2.2. Summarized fit results

In this section, the results for the different fit parameters D , R_F , γ_i are summarized. The outcome for the D and R_F is displayed in Fig. 6.6. For the presentation in this figure and for the discussion in this section, an important remark is to be made: In Sect. 6.2.1 we have pointed out that the single-exciton relaxation rate $1/\tau$ could only be determined with large error bars due to the limited signal-to-noise ratio at the low-density limit. In fact, the values for τ_i (for a given temperature or material) varied by about a factor of 2. The fits have been carried out with distinct values of τ , and the Figs. 6.1–6.5 depict the most appropriate fits to the data. This is to say that the values for the τ_i in these figures are not necessarily always the same. The error bars in Fig. 6.6 indicate the possible variations as a result of the different life times τ_i used in the fits¹⁰.

PTCDA We first discuss the results for PTCDA. The diffusion constants D_{1D} and FÖRSTER radii R_F are depicted by triangles in Fig. 6.6 (a) and (b), respectively. For both room and low temperature, the obtained D_{1D} are independent of the initial exciton density n_0 . This proves that the diffusion model from Sect. 6.1.3 can be consistently applied for various excitation densities n_0 . The temperature dependence of D_{1D} shows an increase from $(4.5 \pm 1) \times 10^{-3} \text{ cm}^2 \text{ s}^{-1}$ at helium temperature to $(4 \pm 1) \times 10^{-2} \text{ cm}^2 \text{ s}^{-1}$ at room temperature. These values are related to annihilation rates via Eq. (6.8), and we obtain $\gamma_{1D,5K} = (1.05 \pm 0.15) \times 10^{-15} \text{ t}^{-1/2} \text{ cm}^3 \text{ s}^{-1/2}$ and $\gamma_{1D,295K} = (3.3 \pm 0.5) \times 10^{-15} \text{ t}^{-1/2} \text{ cm}^3 \text{ s}^{-1/2}$ at 5 K and 295 K, respectively.

SCHÜPPEL and co-workers [125] have extracted exciton diffusion constants and diffusion lengths for PTCDA from luminescence quenching measurements in a double layer system of PTCDA/TiOPC (titanyl-phthalocyanine). They extracted values of $10^{-3} \text{ cm}^2 \text{ s}^{-1}$ at 5 K and $6 \times 10^{-3} \text{ cm}^2 \text{ s}^{-1}$ at 295 K, which are smaller than our values by a factor of 5–7. This difference might be explained with the fact that the probed state in our experiments could differ from the emitting state probed in the luminescence quenching measurements, so that a direct comparison of the values is not appropriate. Moreover, the time window we look at in our experiments is substantially shorter. Thus, we may see a higher effective diffusion coefficient D_{1D} because fewer excitons have been bound by traps and impurities. One might also have in mind local heating effects due to the up to 1000-fold higher excitation density in the pump-probe experiments. Yet, such an effect cannot be held responsible, because our D_{1D} does not depend on n_0 .

A thermally activated hopping process can be regarded as the probable cause for the increase of D_{1D} by one order of magnitude [132]. One should note that this increase in D_{1D} goes in parallel with a decreased life time τ as a result of the activation of nonradiative decay channels. Therefore, the resulting root mean square displacement

$$\Lambda_{1D} = \sqrt{2\tau D_{1D}} \quad (6.17)$$

may eventually be independent of the temperature. In fact, we obtain $\Lambda_{1D} \approx 74 \text{ nm}$ at 5 K and $\Lambda_{1D} \approx 68 \text{ nm}$ at 295 K. Remarkably, the average distance of excitons in the stack at the highest excitation density (h) for PTCDA ($n = 3.1 \times 10^{20} \text{ cm}^{-3}$) is approximately

¹⁰These errors are much larger than the mere (numerical) uncertainty due to the fit algorithm.

6. Exciton-exciton interaction and annihilation at high excitation densities

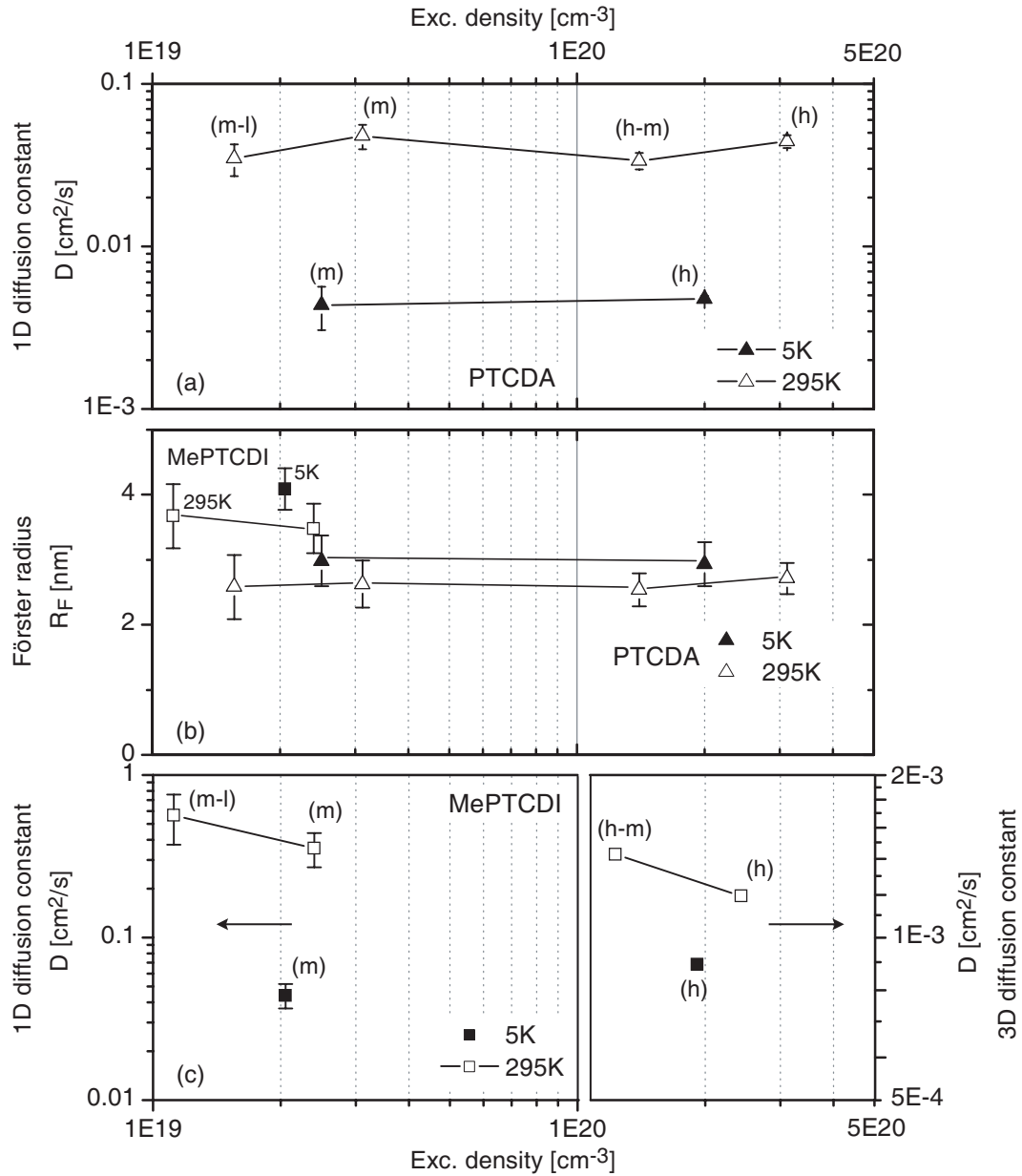


Figure 6.6.: Diffusion constants and FÖRSTER radii obtained from the fits to pump-probe data. Top (a): Diffusion constant D_{1D} from the 1D diffusion model for 295K and 5K for PTCDA. Bottom (c): Diffusion constants D_{1D} from 1D model (left frame) and D_{3D} from 3D model (right frame), whichever fits the data better for the relevant excitation density. Labels next to the data points are again abbreviations for the excitation densities (Table 5.1). Center panel (b): FÖRSTER radii for PTCDA (triangles) and MePTCDI (squares) obtained from the single-step FÖRSTER model. No points are shown for MePTCDI for $n_0 > 10^{20}$ cm⁻³ since the FÖRSTER model is no longer appropriate. Error bars indicate the variations due to different values of the life time τ used in the fits.

$\Delta x = a \cdot N_0/n = 3.1$ nm, which is much smaller than the root mean square displacement. Thus, one of the premises for the derivation of the annihilation constant is not fulfilled, namely the assumption of non-interacting traps. The nevertheless high accuracy of the fit might be explained by the arguments given in the derivation of the 3D-model for the case of overlapping diffusion regions. Alternatively, the underlying mechanism could be a single-step mechanism as discussed below.

GULBINAS et al. [56, 57] as well as MI et al. [141] have carried out investigations of excited state dynamics at high excitation densities of various phthalocyanines¹¹, which also belong to the class of stacked quasi-1D materials. Both groups have obtained 1D annihilation constants in the range $\gamma_{1D,295K} \approx 1 - 3 \times 10^{-15} \text{ t}^{-1/2} \text{ cm}^3 \text{ s}^{-1/2}$, in very good accordance with our values. GULBINAS et al. [56] have also converted the annihilation constants to 1D diffusion constants D_{1D} , being interestingly about one order of magnitude lower than our values. The in-stack distance a for phthalocyanines is on the same order as for PTCDA, but the molecular density N_0 is smaller by a factor of two (due to the larger molecules), which can already explain a factor of 4 in Eq. (6.8).

The FÖRSTER radii R_F for the single-step FÖRSTER model are shown in Fig. 6.6 (b), symbolized by triangles for PTCDA. The resulting R_F are all in the range of 2.8 ± 0.5 nm. From Eq. (6.13), we can evaluate the corresponding annihilation rates $\gamma_{F,5K} = (1.3 \pm 0.2) \times 10^{-15} \text{ t}^{-1/2} \text{ cm}^3 \text{ s}^{-1/2}$ (5 K) and $\gamma_{F,295K} = (3 \pm 0.6) \times 10^{-15} \text{ t}^{-1/2} \text{ cm}^3 \text{ s}^{-1/2}$ (295 K). In accordance with D_{1D} in the 1D diffusion model, the R_F obtained do not depend on the initial exciton density n_0 neither for room nor for helium temperature, which confirms the consistency of the model. Furthermore, it can be seen that the R_F are also independent of T . Temperature-independent values for R_F are consistent with the observed temperature-independent values for the diffusion length Λ_{1D} in the 1D-model, since both parameters describe an effective length scale for the interaction.

A temperature-independent R_F is physically reasonable for the assumed FÖRSTER transfer: Because the $S_1 \rightarrow S_0$ emission spectrum overlaps very well with the excited state absorption band $S_1 \rightarrow S_n$, a temperature-dependent change of the shape of the spectra will not strongly impact on the spectral overlap integral, which determines the FÖRSTER transfer rate. The good spectral overlap, together with the fact that both transitions are strongly allowed singlet-singlet transitions, can also explain the large value of R_F . It is similar to FÖRSTER radii in effective donor-acceptor energy transfer systems, since essentially the same type of transitions is involved. This is in contrast to the mechanism of a nearest-neighbor jump in the diffusion model, where the excitons jump to the nearest neighbor via the reaction $S_1 + S_0 \rightarrow S_0 + S_1$. For this jump to an unexcited molecule, the spectral overlap between $S_1 \rightarrow S_0$ emission and $S_0 \rightarrow S_1$ linear absorption is decisive. Because of the large STOKES-shift in PTCDA films, this overlap is dominated by the wings of the spectra. Thus it is strongly influenced by temperature dependent changes in the peak-width. Rising temperature gives broader spectra, larger overlap and finally larger diffusion constants.

An isotropic FÖRSTER interaction seems to be difficult to reconcile with the highly anisotropic stacked structure, but – as stated above – R_F is a parameter carrying information about effective interaction lengths, and it has been acquired by averaging over a

¹¹Vanadyl-/Lead-/Chlorine-Aluminium/Magnesium-Phthalocyanine (VOPC, PbPC, ClAlPC, MgPC)

large volume. If we count the number N of PTCDA molecules inside a sphere with radius R_F , we obtain $N \approx 240$, which indicates that our system is already turning towards an isotropic system.

For completeness, we also list the diffusion constants D_{3D} obtained within the 3D diffusion-limited model, although it is clearly inferior: $D_{3D,5K} = (6.4 \pm 0.5) \times 10^{-5} \text{ cm}^2 \text{ s}^{-1}$ at 5 K and $D_{3D,295K} = (3.1 \pm 0.3) \times 10^{-4} \text{ cm}^2 \text{ s}^{-1}$ at 295 K, which corresponds to annihilation constants $\gamma_{3D,5K} \approx 1.25 \times 10^{-10} \text{ cm}^3 \text{ s}^{-1}$ and $\gamma_{3D,295K} \approx 5.5 \times 10^{-10} \text{ cm}^3 \text{ s}^{-1}$, respectively. The hopping times at 295 K are $t_H = \bar{a}^2 / (6D_{3D}) = 2.8 \text{ ps}$ and thus very short compared to the time scale we investigate. Thus, in our regime the transient term in the 3D annihilation rate constant in Eq. (6.3) is indeed only a minor correction ($\mathcal{O}(10^{-6})$).

Larger corrections would be expected from other approximations inherent in the simple 3D model: The obtained diffusion constants correspond to 3D root mean square displacements

$$\Lambda_{3D} = \sqrt{6\tau D_{3D}}, \quad (6.18)$$

which gives values of 11 nm at 295 K or 20 nm at 5 K. These root mean square displacements are only 1–1.5 orders of magnitude above the average lattice constant $\bar{a} = 7.24 \text{ \AA}$ and thus the continuum approximation in the 3D model becomes already crude. Furthermore, Λ_{3D} is only a factor of 4–7 above the FÖRSTER radius obtained from the single step model. Alternatively expressed, the number of single diffusion steps during the exciton life time is only, e. g., 160 at 295 K. For such a small number of diffusion steps, a distinction between pure diffusion models and long-range single step models becomes difficult and combined models would be most appropriate. These problems of the 3D-diffusion results arise much less in the 1D-diffusion model, since there the obtained displacements are much larger and the number of single diffusion steps is of the order of $\sim 27,000$ at 295 K, providing internal consistency to the 1D-diffusion model.

MePTCDI We finally summarize the fit parameters for MePTCDI. In Fig. 6.6 (c), the values for the diffusion constants D_{1D} (left frame) and D_{3D} (right frame) are displayed, whichever model is more appropriate at the respective excitation density. For moderate densities (m),(m-l), the diffusion constant D_{1D} increases from $(4.4 \pm 0.8) \times 10^{-2} \text{ cm}^2 \text{ s}^{-1}$ at 5 K to some $(5 \pm 2.5) \times 10^{-1} \text{ cm}^2 \text{ s}^{-1}$ at room temperature, which corresponds to annihilation rates $\gamma_{1D,5K} = (3.8 \pm 0.4) \times 10^{-15} \text{ t}^{-1/2} \text{ cm}^3 \text{ s}^{-1/2}$ and $\gamma_{1D,295K} = (1.25 \pm 0.3) \times 10^{-14} \text{ t}^{-1/2} \text{ cm}^3 \text{ s}^{-1/2}$ at 5 K and 295 K, respectively. Compared to PTCDA, the annihilation rates in MePTCDI are about 3–4 times higher, which thus results in diffusion constants for MePTCDI being about one order of magnitude larger. This result agrees with the perception that all relaxation processes in MePTCDI happen much faster. The observation of the suspiciously high diffusion constants D_{1D} and diffusion lengths Λ_{1D} – we obtain Λ_{1D} of $(160 \pm 70) \text{ nm}$ – indicates that for MePTCDI, an important additional relaxation component seems to be missing in the rate equation Eq.(6.1). One might consider a much higher impurity or static trap concentration than in PTCDA.

Since R_F enters the formula for γ_F in Eq. (6.13) in the cubic term, the 3–4-fold increase of γ_{1D} for MePTCDI leads to FÖRSTER radii which are only about 1.5 times higher for MePTCDI than for PTCDA: In Fig. 6.6 (b), R_F is in the range of $3.8 \pm 0.6 \text{ nm}$, and it is

(almost) independent of temperature and excitation density n_0 in the observed range, in accordance with PTCDA.

For high excitation densities (h-m),(h) the right frame in Fig. 6.6 (c) depicts the results for the diffusion constants D_{3D} resulting from the 3D diffusion model. For density (h), we obtain $D_{3D,5K} = 9 \times 10^{-4} \text{ cm}^2 \text{ s}^{-1}$ at 5 K and $D_{3D,295K} = (1.2 \pm 0.1) \times 10^{-3} \text{ cm}^2 \text{ s}^{-1}$ at 295 K, which are related to annihilation constants $\gamma_{3D,5K} = 1.7 \times 10^{-9} \text{ cm}^3 \text{ s}^{-1}$ and $\gamma_{3D,295K} = (2.28 \pm 0.04) \times 10^{-9} \text{ cm}^3 \text{ s}^{-1}$, respectively. For the 3D diffusion lengths, we obtain $\Lambda_{3D} = 13 \text{ nm}$ at room temperature and $\Lambda_{3D} = 34 \text{ nm}$ at low temperature.

The hopping time $t_H = \bar{a}^2/(6D_{3D})$ derived from these values amounts to only 1 ps at room temperature and is very small compared to the measurement time. Again, this means that in Eq. (6.3) the transient term is negligible. Since the single-exciton relaxation rate in Eq. (6.1) can also be neglected because of the dominating annihilation rate, the exciton density would solely depend on a t -independent rate γ . We then obtain a hyperbolic behavior for the description of the exciton density n :

$$n(t) = \frac{n_0}{1 + \gamma n_0 t}. \quad (6.19)$$

Eq. (6.19) is the limiting case for the highest excitation densities, and it can in fact also be applied to PTCDA data above densities of 10^{21} cm^{-3} , which corresponds already to one exciton per two molecules. It is evident that in this case, the predictive power of our three models fails, because the premises as introduced in the sections 6.1.2–6.1.4 are no longer fulfilled. Still, this does not answer the open question of the surprising difference between PTCDA and MePTCDI. The most promising path to the understanding would be to focus efforts on the clarification of the differences of the single-exciton relaxation behavior in particular, which seems to be significantly different for the both materials and is in either case not well enough understood.

In conclusion of this chapter, we first have presented three different models to describe exciton-exciton annihilation processes at excitation densities higher than about $5 \times 10^{18} \text{ cm}^{-3}$: a three-dimensional diffusion-limited model, a one-dimensional diffusion-limited model, and a single-step long-range FÖRSTER-type annihilation model. Whereas the annihilation rates for the two latter models are structurally equivalent and predict the same type of decay law, the one for the former looks significantly different. All three models essentially have one free parameter: the diffusion constants D_{3D} and D_{1D} or the FÖRSTER-radius R_F . We have applied all three models to a set of excited state absorption data from pump-probe experiments. This has been done for various excitation densities, at both room and helium temperature, and for two materials PTCDA and MePTCDI. In case of PTCDA, all data can be explained with high precision by the 1D diffusion-limited model and the single-step FÖRSTER model. In these cases, the whole set of intensity-dependent multi-exponential decay curves can be consistently fitted. Temperature dependence and order of magnitude of the obtained parameters D_{1D} or R_F correspond to expectations in both models. The 3D annihilation law is significantly less adequate to describe the decay data unless the excitation density exceeds $5 \times 10^{20} \text{ cm}^{-3}$. For MePTCDI, the 1D model and the FÖRSTER model can also successfully describe the

6. Exciton-exciton interaction and annihilation at high excitation densities

decay kinetics, with consistent results for the parameters D_{1D} or R_F . Yet, these models can only be applied at excitation densities less than $5 \times 10^{19} \text{ cm}^{-3}$. The 3D model, however, performs significantly better than the other two at densities around 10^{20} cm^{-3} . This clear difference between the two materials indicates that the single-exciton decay rate entering the annihilation formalism is not yet adequately described for MePTCDI in our models. Therefore, additional efforts should especially focus on a better understanding of this point, preferably with samples of very high purity to rule out trapping caused by impurities.

7. Summary and outlook

Within the framework of this thesis, we have investigated thin polycrystalline films and matrix-isolated molecules of the perylene derivatives PTCDA (3,4,9,10-perylenetetracarboxylic dianhydride) and MePTCDI (N,N'-dimethylperylene-3,4,9,10-dicarboximide). The crystalline phases of these materials are paradigmatic representatives of quasi-one-dimensional organic molecular systems. We addressed transient absorption spectra, excitonic relaxation in the lowest excited state subsequent to excitation, and exciton-exciton interaction and annihilation at high excitation densities by means of femtosecond pump-probe spectroscopy.

7.1. Summary

The knowledge about the nature of the higher excited states and the optical transitions involved in pump-probe experiments are mandatory prerequisites for the investigation of the excited state dynamics based on nonlinear spectroscopy. Upon formation of the molecular crystal, the excited states of the crystalline material are dominated by the excited states of the isolated molecules, which therefore need to be understood first.

For this reason, we first addressed the topic of transient absorption spectra. Since the solubility of PTCDA and MePTCDI is too low to prepare solutions not exhibiting aggregation and still allowing to measure nonlinear optical properties, we used samples where the dye molecules were embedded in a SiO₂ matrix. Transient absorption spectra in the energetic range of 1.2–2.6 eV have been measured with a time resolution of 500 fs. The shape of the spectra did not change with time. We were able to ascribe the respective signal contributions to ground state bleaching, stimulated emission, and excited state absorption. Comparison with quantum-chemical calculations carried out by SCHMIDT et al. allowed to identify the major excited state absorption (ESA) peak around 1.80 eV as the molecular $1B_{3u} \rightarrow 4A_g$ transition (where the label refers to the symmetry of the carbon backbone of MePTCDI or PTCDA). From the pump-probe anisotropy, the orientation of the transition dipole moment was determined to be parallel to the long molecular axis, in accordance with the result of the calculations. Two additional states – $3A_g$ and $6A_g$ – predicted by the calculations at the borders of the observable range could not be assigned without doubt.

As the trustworthiness of the quantum-chemical calculations was proven by the good agreement with the results of the experiments on the isolated molecules, we have also considered calculations on stack dimers by SCHMIDT et al. to explain the transient absorption spectra of thin films. In contrast to the monomer spectra, which were very similar for PTCDA and MePTCDI, the thin film spectra looked distinctly different. The trends visible in the experimental result from monomer to thin film could be understood qualitatively from the changes the calculations exhibited between monomer and dimer

spectra. In particular, three main ESA bands were experimentally observed, around 1.45 eV, 1.85–2.00 eV, and around 2.30 eV. The broad middle energy ESA band was considered suitable for the investigation of the following excited state relaxation dynamics, where the probe pulse spectrum was placed in the middle of this strong transition, so that the population in the first excited state could be monitored.

The second major topic was the relaxation of excitons in the lowest excited state subsequent to photo-excitation at the Γ -point. We discussed this question in the framework of a band structure model by HOFFMANN et al. [8, 34]. From time-resolved luminescence measurements, an upper limit of 10 ps for the population of the emitting states was deduced. Excited state absorption time-resolved the intraband relaxation process and revealed relaxation time constants of 60 fs (MePTCDI) and 90 fs (PTCDA) for moderate excitation densities ($\mathcal{O}(10^{19}) \text{ cm}^{-3}$) at room temperature. We showed that the relaxation process was accelerated by increase of temperature and/or initial excitation density, which could be explained by stimulated phonon emission during relaxation in k -space. We determined a lower limit of 25 fs (resolution limit) for excitation densities $> 10^{20} \text{ cm}^{-3}$ and upper limits of 250 fs (PTCDA) and 100 fs (MePTCDI) at low excitation densities ($\mathcal{O}(10^{18}) \text{ cm}^{-3}$) at helium temperature (signal-to-noise ratio limit).

These measurements were only made possible by the integration of a new pulse shaping device into the pump-probe setup, the acousto-optical programmable dispersive filter (AOPDF). The AOPDF allowed us to flatten the spectral phase of the probe beam, which was necessary to generate shorter probe pulses and to avoid generation of phononic modulations due to the chirped probe pulse that otherwise would have been superimposed on top of the transient absorption signal.

From the comparison of the long-time behavior of the pump-probe ESA signal with the luminescence signal, we tentatively concluded that the state monitored in the ESA experiments was the emitting state. With increasing excitation density, the decay of the pump-probe signal was significantly accelerated, which was interpreted as exciton-exciton interaction and annihilation at densities higher than $5 \times 10^{18} \text{ cm}^{-3}$.

In order to understand the underlying mechanism of annihilation and its related parameters, we have modeled the experimental multiexponential decay dynamics for a set of intensity-dependent decay curves of PTCDA and MePTCDI for both room and low temperature. Three different models have been tested: a diffusion-limited annihilation model in both three and one dimensions (where the diffusion constant D was the major fit parameter), and a long-range FÖRSTER-type annihilation model, with the FÖRSTER radius R_F being the main fit parameter. The structure of the 1D diffusion-limited model and the FÖRSTER model are structurally equivalent. For PTCDA, the 1D and the FÖRSTER models fit the data with high precision, while the 3D model was clearly inferior unless the initial excitation density was very high ($5 \times 10^{20} \text{ cm}^{-3}$). Temperature dependence and orders of magnitude of the obtained parameters D or R_F corresponded to the expectations. However, a decision between them could not be made based on our data. In case of MePTCDI, the 1D and the FÖRSTER model were in good agreement for a smaller interval of excitation densities. For an initial exciton density higher than $5 \times 10^{19} \text{ cm}^{-3}$, the 3D model performed significantly better. This result suggests that the single-exciton relaxation rate, which is distinctively faster than in PTCDA, does not enter the formalism adequately.

7.2. Outlook

In the preceding summary, we have left aside one open issue which could not satisfactorily be answered. While the luminescence anisotropy is in perfect agreement with the expectation from our model calculation and fully consistent with the generally accepted concept of DAVYDOV splitting, the pump-probe anisotropy could not be explained. The degree of knowledge about the states and the transition dipole moments involved in luminescence is still much higher than in the pump-probe experiments, although this thesis adds numerous new contributions to the knowledge base of nonlinear optical properties of PTCDA and MePTCDI. In any case, more sophisticated models with support from quantum-chemical model calculations are mandatory.

A first step towards finding an answer to this open question would certainly be to consider a third perylene derivative as test material, first in luminescence, and later in pump-probe. A possible option would probably be 3,4,9,10-perylenetetracarboxylic bis-benzimidazole (PTCBI), which has been used in the TANG solar cell [5]. However, compared to PTCDA and MePTCDI, the level of understanding of PTCBI is rather modest, at least as far as nonlinear, time-resolved and ultrafast processes are concerned. No band structure models have been adapted to it yet. Yet, a time-resolved luminescence anisotropy experiment, which is much less extensive than a pump-probe experiment, would in fact be a good starting point.

In this thesis, it has not been fully proven that the state probed in pump-probe spectroscopy is actually the emitting state. Still, it is likely that indeed it is. A breakthrough in this context would be an ultrafast experiment on time-resolved luminescence with the pump-probe setup using up-conversion of the luminescence light, because it would help to clarify the nature of the probed states in ESA and in luminescence. Femtosecond luminescence anisotropy should then be in accordance with the luminescence anisotropy as measured with the streak camera system, which would be another test for our model. However, given our experience that it is already very hard even to detect the time-integrated luminescence with the pump-probe setup, this experiment appears extraordinary difficult¹.

As far as the transient spectra of the matrix-isolated samples are concerned, it would definitely be desirable to improve the already satisfying accordance with the quantum-chemical calculations, also as a feedback for the predictive power of the calculations. On the one hand, samples with a lower concentration of dye molecules may help to underline the monomer character of the samples. On the other hand, additional experiments at energies below 1.2 eV will surely answer the question about the nature of the observed ESA transition around 1.35 eV (whether it is the $3A_g$ state or not). This is not straightforward, since it would require a different probe light source and additional IR photodetectors which are currently not part of the experimental setup. A femtosecond continuum with a broader high-energy pedestal towards the near UV (e. g. from CaF_2 or LiF) may help to

¹We recall that PTCDA and MePTCDI are indirect emitters with poor luminescence yield. In fact, we have measured the time-integrated luminescence with the pump-probe setup to exclude any intrinsic anisotropy of the samples. Still, both time-resolved and spectrally resolved measurements would be necessary. A 200 kHz Ti:Sa amplifier system, which we unfortunately do not have access to, is definitely better suited for this experiment.

detect the $6A_g$ state, but it might still be masked by ground state bleaching contributions.

A very interesting question would also be the clarification of the microscopic mechanism of exciton-exciton annihilation. In fact, it would be possible to distinguish between the 1D diffusion-limited model and the FÖRSTER model: Using a set of SiO_2 matrix-systems with sequentially reduced dye concentrations could rule out the diffusion model, since the dye molecules would at some stage be too far apart in space, so that only a long-range FÖRSTER transfer would be possible. However, this will probably result in an insufficient signal-to-noise ratio, at least with a 1 kHz system. Alternatively, one could try to produce 1D isolated stacks, being separated by walls or large outer substituents that would prevent 3D coupling to a large degree and allow interaction in only one direction, as was shown in the stacked quasi-1D phthalocyanines [139].

Appendix A.

Quantum-chemical calculations

The quantum-chemical calculations presented in Chapter 4 have been carried out by K. SCHMIDT, D. BELJONNE, and J.-L. BRÉDAS. This chapter provides additional information to the summary given in Sects. 4.2.4 (monomers) and 4.3.2 (dimers).

General information

The ground state S_0 was optimized with density functional theory (DFT), and the first excited singlet state S_1 with time-dependent density functional theory (TDDFT) [142–144], using the B3LYP exchange-correlation functional [145] and the split valence basis set SV(P) [146] as implemented in TURBOMOLE [147–149]. For the excited state energies and transition dipole moments, the intermediate neglect of differential overlap (INDO/S) method [116] has been used (employing the Mataga-Nishimoto potential to describe Coulomb repulsion terms [150]) combined with two different schemes to include correlation effects: the Coupled Cluster with singles and doubles (CCSD) method [117, 151] and the multireference double-configuration-interaction (MRD-CI) technique [118, 152].

Both approaches are size-consistent and incorporate higher excitations (i.e., doubly, triply, and quadruply excited configurations) that are necessary to provide more quantitative predictions. In particular doubly excited determinants constitute a significant portion of the excited states that are active in two-photon absorption [152–156]. CCSD and MRD-CI both have been demonstrated to provide the excited state energies and transition dipole moments in good agreement with experiment and, thus, to reliably describe excited state absorption [157] and non-linear optical processes such as two-photon absorption [158–161] and third-harmonic generation [159, 160] in conjugated molecules. To account for possible geometrical relaxation of the molecule, calculations have been done for both the ground state (S_0) and first excited state (S_1) geometry.

In all methods, the molecular orbitals entering the active space of configuration interaction (CI space) ranged from the six highest occupied to the six lowest unoccupied molecular orbitals. In case of MRD-CI, the singly excited determinants HOMO \rightarrow LUMO, HOMO \rightarrow LUMO+1, HOMO-1 \rightarrow LUMO, HOMO-1 \rightarrow LUMO+1 and the doubly excited HOMO, HOMO \rightarrow LUMO, LUMO determinant served as references.

Tables A.1 and A.2 list names, ground state energies, polarizations as well as oscillator strengths from the ground state S_0 and the S_1 state for MePTCDI and PTCDA. The data are listed for the first 20 states above $1B_{3u}$, and they are organized by computational method and by geometry.

Table A.1.: Name, ground state energy, oscillator strengths and polarizations for the first 20 electronic states above the lowest excited state for the MePTCDI molecule, by calculation method and by geometry. $f(S_0)$ and $f(S_1)$ are oscillator strengths from the ground state S_0 and the S_1 state, respectively. Labels refer to the D_{2h} symmetry of the MePTCDI backbone. Data reproduced from [115].

CCSD							MRD-CI								
S_1 -geometry				S_0 -geometry				S_1 -geometry				S_0 -geometry			
Name	E(eV)	$f(S_0)$	$f(S_1)$	Name	E(eV)	$f(S_0)$	$f(S_1)$	Name	E(eV)	$f(S_0)$	$f(S_1)$	Name	E(eV)	$f(S_0)$	$f(S_1)$
1A _g	0	-	-	1A _g	0	-	-	1A _g	0	-	-	1A _g	0	-	-
1B _{3u}	2.69	0.79(x)	-	1B _{3u}	2.93	0.83(x)	-	1B _{3u}	2.71	0.92(x)	-	1B _{3u}	2.95	0.94(x)	-
2A _g	3.08	0	$< 10^{-2}$	2A _g	3.51	0	0.04(x)	2A _g	3.14	0	$< 10^{-2}$	2A _g	3.57	0	0.02(x)
1B _{1g}	3.56	0	$< 10^{-2}$	1B _{1g}	3.70	0	$< 10^{-2}$	1B _{1g}	3.69	0	0.01(y)	1B _{1g}	3.80	0	$< 10^{-2}$
1B _{2u}	3.58	$< 10^{-2}$	0	1B _{2u}	3.72	0.01(y)	0	1B _{2u}	3.78	0.01(y)	0	1B _{2u}	3.90	0.02(y)	0
2B _{1g}	3.63	0	$< 10^{-2}$	2B _{1g}	3.89	0	0.09(y)	2B _{1g}	3.83	0	0.09(y)	2B _{1g}	4.16	0	0.12(y)
3B _{1g}	3.85	0	$< 10^{-2}$	3B _{1g}	4.11	0	0.02(y)	3B _{1g}	4.03	0	0.04(y)	3A _g	4.23	0	0.34(x)
3A _g	3.97	0	0.41(x)	3A _g	4.15	0	0.26(x)	3A _g	4.04	0	0.49(x)	3B _{1g}	4.29	0	$< 10^{-2}$
2B _{2u}	4.41	0.22(y)	0	4B _{1g}	4.62	0	$< 10^{-2}$	4B _{1g}	4.68	0	$< 10^{-2}$	4B _{1g}	4.79	0	$< 10^{-2}$
4B _{1g}	4.47	0	$< 10^{-2}$	2B _{2u}	4.64	0.31(y)	0	2B _{2u}	4.68	0.32(y)	0	2B _{2u}	4.91	0.53(y)	0
4A _g	4.63	0	0.85(x)	3B _{2u}	4.87	0.24(y)	0	4A _g	4.81	0	1.05(x)	4A _g	5.08	0	1.27(x)
5A _g	4.67	0	0.01(x)	4A _g	4.91	0	0.97(x)	3B _{2u}	4.93	0.18(y)	0	3B _{2u}	5.12	0.07(y)	0
3B _{2u}	4.70	0.24(y)	0	5A _g	4.99	0	$< 10^{-2}$	4B _{2u}	5.17	0.23(y)	0	4B _{2u}	5.40	0.13(y)	0
4B _{2u}	4.95	0.08(y)	0	4B _{2u}	5.16	0.43(y)	0	5B _{2u}	5.25	0.29(y)	0	5B _{2u}	5.41	0.48(y)	0
5B _{2u}	4.98	0.30(y)	0	5B _{2u}	5.22	$< 10^{-2}$	0	2B _{3u}	5.48	0.04(x)	0	2B _{3u}	5.54	0.01(x)	0
2B _{3u}	5.21	0.01(x)	0	2B _{3u}	5.29	0.01(x)	0	6B _{2u}	5.49	0.06(y)	0	5B _{1g}	5.55	0	0.02(y)
6A _g	5.26	0	0.17(x)	6A _g	5.34	0	0.22(x)	5A _g	5.50	0	0.11(x)	6B _{2u}	5.57	0.04(y)	0
6B _{2u}	5.30	0.06(y)	0	6B _{2u}	5.38	0.10(y)	0	3B _{3u}	5.68	$< 10^{-2}$	0	5A _g	5.61	0	0.09(x)
5B _{1g}	5.34	0	$< 10^{-2}$	5B _{1g}	5.40	0	0.02(y)	7B _{2u}	5.81	0.05(y)	0	3B _{3u}	5.95	0.03(x)	0
3B _{3u}	5.40	$< 10^{-2}$	0	3B _{3u}	5.57	$< 10^{-2}$	0	4B _{3u}	5.87	1.05(x)	0	7B _{2u}	6.07	0.03(y)	0
4B _{3u}	5.44	$< 10^{-2}$	0	4B _{3u}	5.72	0.03(x)	0	8B _{2u}	5.96	0.28(y)	0	4B _{3u}	6.14	0.79(x)	0
6B _{1g}	5.47	0	$< 10^{-2}$	5B _{3u}	5.79	0.89(x)	0	6B _{1g}	5.99	0	0.01(y)	6B _{1g}	6.20	0	0.02(y)

Table A.2.: Name, ground state energy, oscillator strengths and polarizations for the PTCDA molecule, by calculation method and by geometry. $f(S_0)$ and $f(S_1)$ are oscillator strengths from the ground state S_0 and the S_1 state, respectively. Labels refer to the D_{2h} symmetry of PTCDA. Data reproduced from [115].

CCSD							MRD-CI								
S ₁ -geometry			S ₀ -geometry				S ₁ -geometry			S ₀ -geometry					
Name	E(eV)	f(S ₀)	f(S ₁)	Name	E(eV)	f(S ₀)	f(S ₁)	Name	E(eV)	f(S ₀)	f(S ₁)	Name	E(eV)	f(S ₀)	f(S ₁)
1A _g	0	-	-	1A _g	0	-	-	1A _g	0	-	-	1A _g	0	-	-
1B _{3u}	2.74	0.78(x)	-	1B _{3u}	2.98	0.82(x)	-	1B _{3u}	2.75	0.90(x)	-	1B _{3u}	3.00	0.92(x)	-
2A _g	3.09	0	< 10 ⁻²	2A _g	3.53	0	0.03(x)	2A _g	3.16	0	< 10 ⁻²	2A _g	3.59	0	0.01(x)
1B _{1g}	3.54	0	0.05(y)	1B _{1g}	3.72	0	0.01(y)	1B _{1g}	3.70	0	< 10 ⁻²	1B _{1g}	3.82	0	< 10 ⁻²
1B _{2u}	3.59	< 10 ⁻²	0	1B _{2u}	3.73	< 10 ⁻²	0	1B _{2u}	3.77	0.01(y)	0	1B _{2u}	3.90	0.01(y)	0
2B _{1g}	3.63	0	0.03(y)	2B _{1g}	3.84	0	0.07(y)	2B _{1g}	3.82	0	0.11(y)	2B _{1g}	4.11	0	0.10(y)
3B _{1g}	3.93	0	0.02(y)	3B _{1g}	4.20	0	0.04(y)	3B _{1g}	4.08	0	0.01(y)	3A _g	4.28	0	0.33(x)
3A _g	4.02	0	0.41(x)	3A _g	4.21	0	0.27(x)	3A _g	4.09	0	0.50(x)	3B _{1g}	4.36	0	0.03(y)
2B _{2u}	4.34	0.21(y)	0	2B _{2u}	4.55	0.24(y)	0	2B _{2u}	4.63	0.32(y)	0	4B _{1g}	4.83	0	< 10 ⁻²
4B _{1g}	4.50	0	< 10 ⁻²	4B _{1g}	4.67	0	< 10 ⁻²	4B _{1g}	4.69	0	< 10 ⁻²	2B _{2u}	4.86	0.47(y)	0
4A _g	4.64	0	0.08(x)	3B _{2u}	4.91	0.63(y)	0	4A _g	4.83	0	0.95(x)	3B _{2u}	5.10	0.43(y)	0
5A _g	4.65	0	0.73(x)	4A _g	4.93	0	0.83(x)	3B _{2u}	4.93	0.45(y)	0	4A _g	5.11	0	1.15(x)
3B _{2u}	4.74	0.54(y)	0	5A _g	4.97	0	0.02(x)	4B _{2u}	5.17	0.15(y)	0	4B _{2u}	5.43	0.23(y)	0
4B _{2u}	4.92	0.04(y)	0	4B _{2u}	5.18	0.04(y)	0	1B _{1u}	5.43	< 10 ⁻²	0	2B _{3u}	5.49	0.01(x)	0
1B _{1u}	5.15	< 10 ⁻²	0	2B _{3u}	5.24	0.01(x)	0	2B _{3u}	5.43	0.04(x)	0	5B _{2u}	5.55	0.04()	0
2B _{3u}	5.18	0.02(x)	0	6A _g	5.31	0	0.27(x)	5B _{2u}	5.47	0.08(y)	0	5A _g	5.58	0	0.12(x)
6A _g	5.23	0	0.19(x)	1B _{1u}	5.37	< 10 ⁻²	0	5A _g	5.50	0	0.11(x)	5B _{1g}	5.58	0	0.03(y)
5B _{2u}	5.32	0.05(y)	0	5B _{2u}	5.40	0.09(x)	0	5B _{1g}	5.53	0	0.06(y)	6B _{1g}	5.63	< 10 ⁻²	0
5B _{1g}	5.36	0	0.04(y)	5B _{1g}	5.43	0	0.02(y)	3B _{3u}	5.68	< 10 ⁻²	0	3B _{3u}	5.99	0.05(x)	0
3B _{3u}	5.40	< 10 ⁻²	0	3B _{3u}	5.57	< 10 ⁻²	0	4B _{3u}	5.87	1.07(x)	0	4B _{3u}	6.12	0.79(x)	0
6B _{1g}	5.41	0	< 10 ⁻²	4B _{3u}	5.73	0.39(x)	0	6B _{2u}	5.91	0.02(y)	0	6B _{2u}	6.13	0.01(y)	0
4B _{3u}	5.44	< 10 ⁻²	0	5B _{3u}	5.79	0.61(x)	0	6B _{1g}	5.93	0	< 10 ⁻²	7B _{1g}	6.20	0	0.01(y)

Dimer-specific information

Dimer calculations have been carried out in the crystal geometry (MePTCDI [14], PTCDA [24]) for two molecules in stack direction: Single molecules in S_0 -geometry using the B3LYP functional and the CCSD method with a CI space 12/12. Selected data for the stack dimers are listed in Tables A.3 and Table A.4, respectively. Data appear by courtesy of K. SCHMIDT, D. BELJONNE, and J.-L. BRÉDAS.

Table A.3.: Names, ground state energies, and oscillator strengths $f(2A_g)$ for the transitions $2A_g \rightarrow S_n$ from the lowest excited state $2A_g$ to higher excited states S_2 for a MePTCDI dimer in stack geometry. The list of states covers the spectral range as displayed in Fig. 4.10. Polarizations are named for the strongest transitions.

MePTCDI								
Name	E(eV)	$f(2A_g)$	Name	E(eV)	$f(2A_g)$	Name	E(eV)	$f(2A_g)$
$1A_g$	0	-	$9A_u$	4.10	0.04(x)	$15A_u$	4.79	0.05(x)
$2A_g$	2.70	-	$10A_g$	4.12	0	$16A_u$	4.81	0.01(x)
$1A_u$	2.88	0.01(z)	$10A_u$	4.33	0.03(x)	$21A_g$	4.82	0
$3A_g$	2.99	0	$11A_g$	4.36	0	$22A_g$	4.82	0
$2A_u$	3.17	0.03(z)	$12A_g$	4.38	0	$23A_g$	4.84	0
$4A_g$	3.47	0	$13A_g$	4.42	0	$17A_u$	4.86	0.02(x)
$3A_u$	3.49	0.04(x)	$14A_g$	4.47	0	$24A_g$	4.87	0
$4A_u$	3.56	$< 10^{-2}$	$11A_u$	4.48	0.01(y)	$18A_u$	4.88	0.01(x)
$5A_u$	3.57	0.01(x)	$15A_g$	4.51	0	$25A_g$	4.88	0
$5A_g$	3.59	0	$16A_g$	4.52	0	$19A_u$	4.90	$< 10^{-2}$
$6A_g$	3.62	0	$17A_g$	4.56	0	$26A_g$	4.90	0
$6A_u$	3.67	$< 10^{-2}$	$12A_u$	4.60	0.12(x)	$20A_u$	4.95	0.41(x)
$7A_g$	3.68	0	$18A_g$	4.63	0	$27A_g$	4.97	0
$8A_g$	3.85	0	$13A_u$	4.69	$< 10^{-2}$	$21A_u$	4.97	0.07(x)
$7A_u$	3.85	0.04(y)	$19A_g$	4.73	0	$22A_u$	4.99	$< 10^{-2}$
$9A_g$	3.98	0	$14A_u$	4.74	0.14(x)	$28A_g$	5.00	0
$8A_u$	4.03	0.12(x)	$20A_g$	4.79	0	$29A_g$	5.00	0

Table A.4.: Names, ground state energies, and oscillator strengths $f(2A_g)$ for the transitions $2A_g \rightarrow S_n$ from the lowest excited state $2A_g$ to higher excited states S_2 for a PTCDA dimer in stack geometry. The list of states covers the spectral range as displayed in Fig. 4.11. Polarizations are named for the strongest transitions.

PTCDA								
Name	E(eV)	$f(2A_g)$	Name	E(eV)	$f(2A_g)$	Name	E(eV)	$f(2A_g)$
1A _g	0	-	12A _u	4.44	0.08(x)	24A _u	4.92	$< 10^{-2}$
2A _g	2.76	-	12A _u	4.44	0.01(x)	24A _g	4.93	0
3A _g	2.90	0	13A _g	4.52	0	25A _g	4.95	0
1A _u	3.01	0.01(z)	14A _u	4.56	0.10(x)	26A _g	4.95	0
2A _u	3.09	$< 10^{-2}$	14A _g	4.57	0	27A _g	4.97	0
4A _g	3.48	0	15A _u	4.60	0.05(x)	25A _u	4.98	0.02(x)
3A _u	3.50	0.04(x)	15A _g	4.70	0	26A _u	5.00	0.02(z)
4A _u	3.54	$< 10^{-2}$	16A _u	4.69	0.04(x)	28A _g	5.03	0
5A _u	3.61	0.01(y)	16A _g	4.69	0	27A _u	5.07	0.07(x)
5A _g	3.62	0	17A _u	4.69	$< 10^{-2}$	28A _u	5.08	0.20(x)
6A _g	3.64	0	17A _g	4.70	0	29A _g	5.09	0
6A _u	3.68	$< 10^{-2}$	18A _g	4.72	0	30A _g	5.13	0
7A _g	3.75	0	18A _u	4.73	0.01(z)	29A _u	5.17	0.04(x)
7A _u	3.78	0.06(y)	19A _u	4.73	0.28(x)	31A _g	5.22	0
8A _g	3.80	0	20A _u	4.76	0.04(x)	30A _u	5.22	0.05(x)
8A _u	4.07	0.09(x)	19A _g	4.78	0	32A _g	5.26	0
9A _g	4.12	0	21A _u	4.79	$< 10^{-2}$	31A _u	5.27	0.02(x)
9A _u	4.13	0.05(x)	22A _u	4.80	0.08(x)	33A _g	5.29	0
10A _g	4.19542	0	20A _g	4.81	0	32A _u	5.29	0.15(x)
10A _u	4.28	0.01(x)	21A _g	4.85	0	33A _u	5.34	0.02(y)
11A _g	4.30	0	22A _g	4.89	0	34A _g	5.35	0
11A _u	4.32	0.01(x)	23A _g	4.89	0	35A _u	5.38	$< 10^{-2}$
12A _g	4.34	0	23A _u	4.91	$< 10^{-2}$	36A _g	5.41	0

Bibliography

- [1] C. W. Tang, private communication, data provided by Display Search, <http://www.displaysearch.com>, 2005.
- [2] C. W. Tang and S. A. VanSlyke, "Organic electroluminescent diodes", *Appl. Phys. Lett.*, vol. 51, pp. 913–915, 1987.
- [3] J. H. Burroughes, D. D. C. Bradley, A. R. Brown, R. N. Marks, K. Mackay, R. H. Friend, P. L. Burns, and A. B. Holmes, "Light-emitting-diodes based on conjugated polymers", *Nature*, vol. 347, pp. 539–541, 1990.
- [4] A. Dodabalapur, H. Katz, L. Torsi, and R. Haddon, "Organic heterostructure field-effect transistors", *Science*, vol. 269, pp. 1560–1562, 1995.
- [5] C. W. Tang, "Two-layer organic photovoltaic cell", *Appl. Phys. Lett.*, vol. 48, pp. 183–185, 1986.
- [6] C. Kittel, *Einführung in die Festkörperphysik*. R. Oldenbourg Verlag, München, 13th ed., 2002.
- [7] E. V. Tsiper and Z. G. Soos, "Charge redistribution and polarization energy of organic molecular crystals", *Phys. Rev. B*, vol. 64, p. 195124, 2001.
- [8] M. Hoffmann and Z. G. Soos, "Optical absorption spectra of the holstein molecular crystal for weak and intermediate electronic coupling", *Phys. Rev. B*, vol. 66, p. 024305, 2002.
- [9] A. S. Davydov, *Theory of molecular excitons*. Plenum Press, New York, first ed., 1971.
- [10] H. Haken and H. C. Wolf, *Molekülphysik und Quantenchemie*. Springer, Berlin, fourth ed., 2002.
- [11] E. A. Silinsh and V. Čápek, *Organic molecular crystals*. AIP Press, New York, first ed., 1994.
- [12] T. Kobayashi, ed., *J-Aggregates*. Singapore: World Scientific, first ed., 1996.
- [13] F. Graser and E. Hädicke, "Kristallstruktur und Farbe bei Perylen-3,4:9,10-bis-(dicarboximid)-Pigmenten, 2", *Liebigs Ann. Chem.*, pp. 483–494, 1984.
- [14] E. Hädicke and F. Graser, "Structures of eleven perylene-3,4:9,10-bis(dicarboximide) pigments", *Acta. Cryst. C*, vol. 42, pp. 189–195, 1986.
- [15] G. Klebe, F. Graser, E. Hädicke, and J. Berndt, "Crystallochromy as a solid-state effect: Correlation of molecular conformation, crystal packing and colour in perylene-3,4:9,10-bis(dicarboximide) pigments", *Acta Cryst.B*, vol. 45, pp. 69–77, 1989.
- [16] M. Pope and C. E. Swenberg, *Electronic Processes in Organic Crystals and Polymers*. Oxford University Press, New York, second ed., 1999.

- [17] S. R. Forrest, "Ultrathin organic films grown by organic molecular beam deposition and related techniques", *Chem. Rev.*, vol. 97, pp. 1793–1896, 1997.
- [18] E. Umbach, K. Glöckler, and M. Sokolowski, "Surface architecture with large organic molecules: Interface order and epitaxy", *Surface Science*, vol. 402–404, pp. 20–31, 1998.
- [19] D. Meissner and J. Rostalski, "Photovoltaics of interconnected networks", *Synth. Met.*, vol. 121, pp. 1551–1552, 2001.
- [20] P. Peumans, V. Bulović, and S. R. Forrest, "Efficient photon harvesting at high optical intensities in ultrathin organic double-heterostructure photovoltaic diodes", *Appl. Phys. Lett.*, vol. 76, pp. 2650–2652, 2000.
- [21] P. Peumans, S. Uchida, and S. R. Forrest, "Efficient bulk heterojunction photovoltaic cells using small-molecular-weight organic thin films", *Nature*, vol. 425, pp. 158–162, 2003.
- [22] N. Karl and J. Marktanner, "Structural order and photoelectric properties of organic thin films", *Mol. Cryst. Liq. Cryst.*, vol. 315, pp. 163–168, 1998.
- [23] M. Hoffmann, K. Schmidt, T. Fritz, T. Hasche, V. M. Agranovich, and K. Leo, "The lowest energy Frenkel and charge-transfer excitons in quasi-one-dimensional structures: application to MePTCDI and PTCDA crystals", *Chem. Phys.*, vol. 258, pp. 73–96, 2000.
- [24] A. J. Lovinger, S. R. Forrest, M. L. Kaplan, P. H. Schmidt, and T. Venkatesan, "Structural and morphological investigation of the development of electrical conductivity in ion-irradiated thin films of an organic material", *J. Appl. Phys.*, vol. 55, pp. 476–482, 1984.
- [25] U. Gomez, M. Leonhardt, H. Port, and H. C. Wolf, "Optical properties of amorphous ultrathin films of perylene derivatives", *Chem. Phys. Lett.*, vol. 268, pp. 1–6, 1997.
- [26] M. Leonhardt, O. Mager, and H. Port, "Two-component optical spectra in thin PTCDA films due to the coexistence of α and β -phase", *Chem. Phys. Lett.*, vol. 313, pp. 24–30, 1999.
- [27] M. Sadrai, L. Hadel, R. R. Sauer, S. Husain, K. Krogh-Jespersen, J. D. Westbrook, and G. R. Bird, "Lasing action in a family of perylene derivatives: singlet absorption and emission spectra, triplet absorption and oxygen quenching constants, and molecular mechanics and semiempirical molecular orbital calculations", *J. Phys. Chem.*, vol. 96, pp. 7988–7996, 1992.
- [28] M. Adachi, Y. Murata, and S. Nakamura, "Spectral similarity and difference of naphthalenetetracarboxylic dianhydride, perylenetetracarboxylic dianhydride, and their derivatives", *J. Phys. Chem.*, vol. 99, pp. 14240–14246, 1995.
- [29] R. Scholz, A. Y. Kobitski, T. U. Kampen, M. Schreiber, D. R. T. Zahn, G. Jungnickel, M. Elstner, M. Sternberg, and T. Frauenheim, "Resonant Raman spectroscopy of 3,4,9,10-perylene-tetracarboxylic-dianhydride epitaxial films", *Phys. Rev. B*, vol. 61, pp. 13659–13669, 2000.
- [30] M. Makowski and M. T. Pawlikowski, "The Franck-Condon effect in 1^1B_{1u} state of 3,4,9,10-perylenetetracarboxylic-dianhydride", *Chem. Phys. Lett.*, vol. 393, pp. 305–308, 2004.
- [31] J. P. Toennies and A. F. Vilesov, "Spectroscopy of atoms and molecules in liquid helium", *Ann. Rev. Phys. Chem.*, vol. 49, pp. 1–41, 1998.

- [32] M. Wewer and F. Stienkemeier, “Laser-induced fluorescence spectroscopy of 3,4,9,10-perylenetetracarboxylic-dianhydride in helium nanodroplets”, *J. Chem. Phys.*, vol. 120, pp. 1239–1244, 2004.
- [33] M. Wewer and F. Stienkemeier, “Laser-induced fluorescence spectroscopy of N,N'-dimethyl 3,4,9,10-perylene tetracarboxylic diimide monomers and oligomers attached to helium nanodroplets”, *Phys. Chem. Chem. Phys.*, vol. 7, pp. 1171–1175, 2005.
- [34] M. Hoffmann, *Mixing of Frenkel and Charge-Transfer Excitons and their quantum confinement in thin films*, vol. 31 of *Thin films and nanostructures*, ch. 5, pp. 221–292. Elsevier, 2003.
- [35] T. W. Canzler, *Ultrafast Dynamics in Quasi-One-Dimensional Organic Molecular Crystals. Self-Assembled Monolayers of Photochromic Molecules*. PhD thesis, Institut für Angewandte Photophysik, Technische Universität Dresden, 2002.
- [36] P. M. Kazmaier and R. Hoffmann, “A theoretical study of crystallochromy. Quantum interference effects in the spectra of perylene pigments”, *J. Am. Chem. Soc.*, vol. 116, pp. 9684–9691, 1994.
- [37] V. Bulović, P. E. Burrows, S. R. Forrest, J. A. Cronin, and M. E. Thompson, “Study of localized and extended excitons in 3,4,9,10-perylenetetracarboxylic dianhydride (PTCDA). I. Spectroscopic properties of thin films and solutions”, *Chem. Phys.*, vol. 210, pp. 1–12, 1996.
- [38] M. H. Hennessy, Z. G. Soos, R. A. Pascal Jr., and A. Girlando, “Vibronic structure of PTCDA stacks: The exciton-phonon-charge-transfer dimer”, *Chem. Phys.*, vol. 245, pp. 199–212, 1999.
- [39] G. Mazur, P. Petelenz, and M. Slawik, “Theoretical calculations of the electroabsorption spectra of perylenetetracarboxylic dianhydride”, *J. Chem. Phys.*, vol. 118, pp. 1423–1432, 2003.
- [40] I. Vragović and R. Scholz, “Frenkel exciton model of optical absorption and photoluminescence in α -PTCDA”, *Phys. Rev. B*, vol. 68, p. 155202, 2003.
- [41] T. Holstein, “Studies of polaron motion. Part I. The molecular-crystal model”, *Ann. Phys.*, vol. 8, pp. 325–342, 1959.
- [42] T. Holstein, “Studies of polaron motion. Part II. The “small” polaron”, *Ann. Phys.*, vol. 8, pp. 343–389, 1959.
- [43] A. Nollau, M. Hoffmann, K. Floreck, T. Fritz, and K. Leo, “A simple measurement of the absolute internal quantum efficiency of thin organic films”, *J. Appl. Phys.*, vol. 87, pp. 7802–7804, 2000.
- [44] R. E. Merrifield, “Ionized states in a one-dimensional molecular crystal”, *J. Chem. Phys.*, vol. 34, p. 1835, 1961.
- [45] Z. Shen, P. Burrows, S. Forrest, Z. Ziari, and W. Steier, “Electroabsorption due to excitons in crystalline molecular thin films grown by organic molecular beam deposition”, *Chem. Phys. Lett.*, vol. 236, pp. 129–134, 1995.

- [46] A. Y. Kobitski, R. Scholz, I. Vragović, H. P. Wagner, and D. R. T. Zahn, “Low-temperature time-resolved photoluminescence characterization of 3,4,9,10-perylene tetracarboxylic dianhydride crystals”, *Phys. Rev. B*, vol. 66, p. 153204, 2002.
- [47] A. Y. Kobitski, R. Scholz, D. R. T. Zahn, and H. P. Wagner, “Time-resolved photoluminescence study of excitons in α -PTCDA as a function of temperature”, *Phys. Rev. B*, vol. 68, p. 155201, 2003.
- [48] M. I. Alonso, M. Garriga, N. Karl, J. O. Ossó, and F. Schreiber, “Anisotropic optical properties of single crystalline PTCDA studied by spectroscopic ellipsometry”, *Org. Electron.*, vol. 3, pp. 23–31, 2002.
- [49] S. V. Frolov, Z. Bao, M. Wohlgenannt, and Z. V. Vardeny, “Ultrafast spectroscopy of even-parity states in π -conjugated polymers”, *Phys. Rev. Lett.*, vol. 85, pp. 2196–2199, 2000.
- [50] T. Kobayashi, A. Shirakawa, H. Matsuzawa, and H. Nakanishi, “Real-time vibration mode-coupling associated with ultrafast geometrical relaxation in polydiacetylene induced by sub-5fs pulses”, *Chem. Phys. Lett.*, vol. 321, pp. 385–393, 2000.
- [51] O. J. Korovyanko, I. I. Gontia, Z. V. Vardeny, T. Masuda, and K. Yoshino, “Ultrafast dynamics of excitons and solitons in disubstituted polyacetylene”, *Phys. Rev. B*, vol. 67, p. 035114, 2003.
- [52] I. G. Scheblykin, O. Y. Sliusarenko, L. S. Lepnev, A. G. Vitukhnovsky, and M. Van der Auweraer, “Excitons in molecular aggregates of 3,3'-bis-[3-sulfopropyl]-5,5'-dichloro-9 ethylthiacarbocyanine (THIATS): Temperature dependent properties”, *J. Phys. Chem. B*, vol. 105, pp. 4636–4646, 2001.
- [53] K. Ohta, M. Yang, and G. R. Fleming, “Ultrafast exciton dynamics of J-aggregates in room temperature solution studied by third-order nonlinear optical spectroscopy and numerical simulation based on exciton theory”, *J. Chem. Phys.*, vol. 115, pp. 7609–7621, 2001.
- [54] G. Lanzani, S. V. Frolov, P. A. Lane, Z. V. Vardeny, M. Nisoli, and S. De Silvestri, “Transient spectroscopy of Frenkel and charge transfer excitons in alpha-sexithienyl films”, *Phys. Rev. Lett.*, vol. 79, pp. 3066–3069, 1997.
- [55] S. V. Frolov, C. Kloc, B. Batlogg, M. Wohlgenannt, X. Jiang, and Z. V. Vardeny, “Excitation dynamics in single molecular crystals of alpha-hexathiophene from femtoseconds to milliseconds”, *Phys. Rev. B*, vol. 63, p. 205203, 2001.
- [56] V. Gulbinas, M. Chachisvilis, A. Persson, S. Svanberg, and V. Sundström, “Ultrafast excitation relaxation in colloidal particles of chloraluminium phthalocyanine: one-dimensional exciton-exciton annihilation”, *J. Phys. Chem.*, vol. 98, pp. 8118–8123, 1994.
- [57] V. Gulbinas, M. Chachisvilis, L. Valkunas, and V. Sundström, “Excited state dynamics of phthalocyanine films”, *J. Phys. Chem.*, vol. 100, pp. 2213–2219, 1996.
- [58] D. Ino, K. Watanabe, N. Takagi, and Y. Matsumoto, “Ultrafast excited state dynamics in 3,4,9,10-perylene tetracarboxylic dianhydride (PTCDA) thin films”, *Chem. Phys. Lett.*, vol. 383, pp. 261–265, 2004.
- [59] M. A. Baldo and S. R. Forrest, “Transient analysis of organic electrophosphorescence: I. Transient analysis of triplet energy transfer”, *Phys. Rev. B*, vol. 62, pp. 10958–10966, 2000.

-
- [60] M. A. Baldo, C. Adachi, and S. R. Forrest, “Transient analysis of organic electrophosphorescence. II. Transient analysis of triplet-triplet annihilation”, *Phys. Rev. B*, vol. 62, pp. 10967–10977, 2000.
- [61] M. A. Baldo, R. J. Holmes, and S. R. Forrest, “Prospects for electrically pumped organic lasers”, *Phys. Rev. B*, vol. 66, p. 035321, 2002.
- [62] C. Rullière, ed., *Femtosecond laser pulses*. Springer, Berlin, second ed., 2004.
- [63] J.-C. Diels and W. Rudolph, *Ultrashort laser pulse phenomena*. Academic Press, San Diego, first ed., 1996.
- [64] Schott AG, “Schott Optischer Glaskatalog.” Available online and for download at http://www.schott.com/optics_devices/german/download/index.html.
- [65] M. Bass, ed., *Handbook of optics*, vol. II, Part 4– Optical and physical properties of materials. Optical Society of America, second ed., 1995.
- [66] C. Spielmann, F. Krausz, T. Brabec, E. Wintner, and A. J. Schmidt, “Femtosecond pulse generation from a synchronously pumped Ti:sapphire laser”, *Opt. Lett.*, vol. 16, pp. 1180–1182, 1991.
- [67] R. W. Boyd, *Nonlinear optics*. Academic Press, San Diego, Ca., second ed., 2003.
- [68] R. R. Alfano and S. L. Shapiro, “Observation of self-phase modulation and small-scale filaments in crystals and glasses”, *Phys. Rev. Lett.*, vol. 24, pp. 592–596, 1970.
- [69] R. L. Fork, C. V. Shank, C. Hirlimann, and R. Yen, “Femtosecond white-light continuum pulses”, *Opt. Lett.*, vol. 8, pp. 1–3, 1983.
- [70] A. Brodeur and S. L. Chin, “Band-gap dependence of the ultrafast white-light continuum”, *Phys. Rev. Lett.*, vol. 80, pp. 4406–4409, 1998.
- [71] A. Brodeur and S. L. Chin, “Ultrafast white-light continuum generation and self-focusing in transparent condensed media”, *J. Opt. Soc. Am. B*, vol. 16, pp. 637–650, 1999.
- [72] M. Kolesik, G. Katona, J. V. Moloney, and E. M. Wright, “Physical factors limiting the spectral extent and band gap dependence of supercontinuum generation”, *Phys. Rev. Lett.*, vol. 91, p. 043905, 2003.
- [73] M. Kolesik, G. Katona, J. V. Moloney, and E. M. Wright, “Theory and simulation of supercontinuum generation in transparent bulk media”, *Appl. Phys. B*, vol. 77, pp. 185–195, 2003.
- [74] V. G. Dmitriev, G. G. Gurzadyan, and D. N. Nikogosyan, *Handbook of nonlinear optical crystals*. Springer, Berlin, third ed., 1999.
- [75] P. Di Trapani, A. Andreoni, G. P. Banfi, C. Solcia, R. Danielius, A. Piskarskas, P. Foggi, M. Monguzzi, and C. Sozzi, “Group-velocity self-matching of femtosecond pulses in non-collinear parametric generation”, *Phys. Rev. A*, vol. 51, pp. 3164–3468, 1995.
- [76] G. M. Gale, M. Cavallari, T. J. Driscoll, and F. Hache, “Sub-20-fs tunable pulses in the visible from an 82-MHz optical parametric oscillator”, *Opt. Lett.*, vol. 20, pp. 1562–1564, 1995.

- [77] T. Wilhelm, J. Piel, and E. Riedle, “Sub-20-fs pulses tunable across the visible from a blue-pumped single-pass noncollinear parametric converter”, *Opt. Lett.*, vol. 22, pp. 1494–1498, 1997.
- [78] G. Cerullo, M. Nisoli, and S. De Silvestri, “Generation of 11 fs pulses tunable across the visible by optical parametric amplification”, *Appl. Phys. Lett.*, vol. 71, pp. 3616–3618, 1997.
- [79] R. Huber, H. Satzger, W. Zinth, and J. Wachtveitl, “Noncollinear optical parametric amplifiers with output parameters improved by the application of a white light continuum generated in CaF₂”, *Opt. Commun.*, vol. 194, pp. 443–448, 2001.
- [80] R. Danielius, A. Piskarskas, P. Di Trapani, A. Andreoni, C. Solcia, and P. Foggi, “Matching of group velocities by spatial walk-off in collinear three-wave interaction with tilted pulses”, *Opt. Lett.*, vol. 21, pp. 973–975, 1996.
- [81] A. Shirakawa and T. Kobayashi, “Noncollinear phase- and group-velocity matching of optical parametric amplifier for ultrashort pulse generation”, *IEICE Trans. Electron.*, vol. E81-C, pp. 246–253, 1998.
- [82] P. Tzankov and T. Fiebig, “Tunable femtosecond pulses in the near-ultraviolet from ultra-broadband parametric amplification”, *Appl. Phys. Lett.*, vol. 82, pp. 517–519, 2003.
- [83] A. M. Weiner, “Femtosecond pulse shaping using spatial light modulators”, *Rev. Sci. Instrum.*, vol. 71, pp. 1929–1960, 2000.
- [84] A. M. Weiner, D. Leaird, J. Patel, and J. R. Wullert, “Programmable shaping of femtosecond optical pulses by use of 128-element liquid crystal phase modulator”, *IEEE J. Quantum Electron.*, vol. 28, pp. 908–920, 1992.
- [85] R. L. Fork, C. H. Brito Cruz, P. C. Becker, and C. V. Shank, “Compression of optical pulses to six femtoseconds by using cubic phase compensation”, *Opt. Lett.*, vol. 12, pp. 483–485, 1987.
- [86] R. Szipöcs, K. Ferencz, C. Spielmann, and F. Krausz, “Chirped multilayer coatings for broad-band dispersion control in femtosecond lasers”, *Opt. Lett.*, vol. 19, pp. 201–203, 1994.
- [87] D. Kaplan and P. Tournois, “Acousto-optic spectral filtering of femtosecond laser pulses” in *Ultrafast optics IV* (F. Krausz et al., ed.), pp. 105–118, Springer, Berlin, 2004.
- [88] P. Tournois, “Acousto-optic programmable dispersive filter for adaptive compensation of group delay time dispersion in laser systems”, *Opt. Commun.*, vol. 140, pp. 245–249, 1997.
- [89] M. A. Dugan, J. X. Tull, and W. S. Warren, “High-resolution acousto-optic shaping of unamplified and amplified femtosecond laser pulses”, *J. Opt. Soc. Am. B*, vol. 14, pp. 2348–2358, 1997.
- [90] F. Verluise, V. Laude, Z. Cheng, C. Spielmann, P. Tournois, and A. Migus, “Amplitude and phase control of ultrashort pulses by use of an acousto-optic programmable dispersive filter: pulse compression and shaping”, *Opt. Lett.*, vol. 25, pp. 575–577, 2002.
- [91] F. Verluise, V. Laude, J. P. Huignard, and P. Tournois, “Arbitrary dispersion control of ultrashort optical pulses with acoustic waves”, *J. Opt. Soc. Am. B*, vol. 17, pp. 138–145, 2000.
- [92] A. Yariv and P. Yeh, *Optical waves in crystals*. Wiley, New York, 1984.

- [93] P. Tournois, private communication, 2005.
- [94] J. Chilla and O. Martinez, “Analysis of a method of phase measurement of ultrashort pulses in the frequency-domain”, *IEEE J. Quantum Elect.*, vol. 27, pp. 1228–1235, 1991.
- [95] A. Monmayrant, A. Arbouet, B. Girard, B. Chatel, A. Barman, B. J. Whitaker, and D. Kaplan, “CMB6: Optimisation of NOPA output pulse shaping using an AOPDF with dispersion self-correction” in *Conference on Lasers and Electro-Optics/Quantum Electronics and Laser Science and Photonic Applications, Systems and Technologies 2005*, (Optical Society of America, Washington, DC), 2005.
- [96] G. Stock and W. Domcke, “Detection of ultrafast molecular-excited-state dynamics with time- and frequency-resolved pump-probe spectroscopy”, *Phys. Rev. A*, vol. 45, pp. 3032–3042, 1992.
- [97] J. Shah, “Ultrafast spectroscopy of semiconductors and semiconductor nanostructures” in *Springer Series in Solid-State Sciences* (M. Cardona, P. Fulde, K. von Klitzing, and H.-J. Queisser, eds.), Springer, Berlin, 1996.
- [98] S. Oliveira, L. De Boni, D. S. Corrêa, L. Misoguti, S. Zílio, C. R. Mendonça, C. J. L. Constantino, and R. F. Aroca, “JWB36: Nonlinear absorption spectrum in perylene derivatives” in *Conference on Lasers and Electro-Optics/Quantum Electronics and Laser Science and Photonic Applications, Systems and Technologies 2005*, (Optical Society of America, Washington, DC), 2005.
- [99] S. L. Oliveira, D. S. Corrêa, L. Misoguti, C. J. L. Constantino, R. F. Aroca, S. C. Zílio, and C. R. Mendonça, “Perylene derivatives with large two-photon absorption cross-sections for application in optical limiting and upconversion lasing”, *Adv. Mat.*, vol. 17, pp. 1890–1893, 2005.
- [100] M. Hoffmann, *Frenkel and charge-transfer excitons in quasi-one-dimensional molecular crystals with strong intermolecular orbital overlap*. PhD thesis, Institut für Angewandte Photophysik, Technische Universität Dresden, 2000.
- [101] K. Floreck, *Untersuchungen zum Zusammenhang zwischen Excitonendynamik und Schichtstruktur in organischen Farbstoffaufdampfschichten*. Diplomarbeit, Institut für Angewandte Photophysik, Technische Universität Dresden, 1997.
- [102] A. Goldsmith, T. Waterman, and H. Hirschhorn, *Handbook of thermophysical properties of solid materials*, vol. 3–Ceramics. Pergamon Press, Oxford, first ed., 1961.
- [103] A. B. Djuricic, T. Fritz, and K. Leo, “Determination of optical constants of thin absorbing films from normal incidence reflectance and transmittance measurements”, *Opt. Commun.*, vol. 166, pp. 35–42, 1999.
- [104] A. B. Djuricic, T. Fritz, and K. Leo, “Modeling the optical constants of organic thin films: application to 3,4,9,10-perylenetetracarboxylic dianhydride (PTCDA)”, *Opt. Commun.*, vol. 183, pp. 123–132, 2000.
- [105] W. H. Melhuish, “Absolute spectrofluorometry” in *National Bureau of Standards Special Publication 378, Accuracy in spectrophotometry and luminescence measurements : Proceedings of the conference held at the National Bureau of Standards, Gaithersburg, Md. March 22-24, 1972* (R. Mavrodineanu and J. I. Shultz, eds.), pp. 137–150, National Bureau of Standards, Washington, 1973.

- [106] M. Wewer and F. Stienkemeier, “Molecular versus excitonic transitions in PTCDA dimers and oligomers studied by helium nanodroplet isolation spectroscopy”, *Phys. Rev. B*, vol. 67, p. 125201, 2003.
- [107] H. Proehl, T. Dienel, R. Nitsche, and T. Fritz, “Formation of solid-state excitons in ultrathin crystalline films of PTCDA: From single molecules to molecular stacks”, *Phys. Rev. Lett.*, vol. 93, p. 097403, 2004.
- [108] T. Hasche, T. W. Canzler, R. Scholz, M. Hoffmann, K. Schmidt, T. Frauenheim, and K. Leo, “Coherent external and internal phonons in quasi-one-dimensional organic molecular crystals”, *Phys. Rev. Lett.*, vol. 86, pp. 4060–4063, 2001.
- [109] E. M. H. P. Van Dijk, J. Hernando, J.-J. García-López, M. Crego-Calama, D. N. Reinhoudt, L. Kuipers, M. F. García-Parajó, and N. F. Van Hulst, “Single-molecule pump-probe detection resolves ultrafast pathways in individual and coupled quantum systems”, *Phys. Rev. Lett.*, vol. 94, p. 078302, 2005.
- [110] E. M. H. P. Van Dijk, J. Hernando, M. F. García-Parajó, and N. F. Van Hulst, “Single-molecule pump-probe experiments reveal variations in ultrafast energy redistribution”, *J. Chem. Phys.*, vol. 123, p. 064703, 2005.
- [111] M. Hoffmann, Z. G. Soos, and K. Leo, “Absorption spectra and band-structure of mixed Frenkel-charge-transfer vibronic states in one-dimensional molecular crystals”, *Nonl. Opt.*, vol. 29, pp. 227–237, 2002.
- [112] E. Engel, M. Koschorreck, K. Leo, and M. Hoffmann, “Ultrafast relaxation in quasi-one-dimensional organic molecular crystals”, *Phys. Rev. Lett.*, vol. 95, p. 157403, 2005.
- [113] E. Engel, K. Leo, and M. Hoffmann, “Ultrafast relaxation and exciton-exciton annihilation in PTCDA thin films at high excitation densities”, *Chem. Phys.*, *in press*, 2005.
- [114] J. R. Lakowicz, ed., *Principles of luminescence spectroscopy*. Kluwer Academic/Plenum Publ., New York, second ed., 1999.
- [115] E. Engel, K. Schmidt, D. Beljonne, J.-L. Brédas, J. Assa, H. Fröb, K. Leo, and M. Hoffmann, “Transient absorption spectroscopy and quantum-chemical studies of matrix-isolated perylene-related molecules”, *Phys. Rev. B (submitted)*, 2005.
- [116] J. Ridley and M. Zerner, “Intermediate neglect of differential overlap technique for spectroscopy - pyrrole and azines”, *Theo. Chim. Acta*, vol. 32, pp. 111–134, 1973.
- [117] G. D. Purvis III and R. Bartlett, “A full coupled cluster singles and doubles model: The inclusion of disconnected triples”, *J. Chem. Phys.*, vol. 76, pp. 1910–1918, 1982.
- [118] R. J. Buenker and S. D. Peyerimhoff, “Individualized configuration selection in CI calculations with subsequent energy extrapolation”, *Theor. Chim. Acta*, vol. 35, pp. 33–58, 1974.
- [119] K. Schmidt, D. Beljonne, J.-L. Brédas, E. Engel, K. Leo, and M. Hoffmann, in preparation.
- [120] H. Proehl, R. Nitsche, T. Dienel, K. Leo, and T. Fritz, “In situ differential reflectance spectroscopy of thin crystalline films of PTCDA on different substrates”, *Phys. Rev. B*, vol. 71, p. 165207, 2005.
- [121] K. Schmidt, private communication, based on TD-DFT calculations of PTCDA ions, 2005.

-
- [122] K. Schmidt, private communication, 2005.
- [123] F. F. So and S. R. Forrest, "Evidence for exciton confinement in crystalline organic multiple quantum wells", *Phys. Rev. Lett.*, vol. 66, pp. 2649–2651, 1991.
- [124] K. Puech, H. Fröb, and K. Leo, "Excimer dynamics in ultrathin organic films", *J. Lum.*, vol. 72–74, pp. 524–525, 1997.
- [125] R. Schüppel, T. Dienel, K. Leo, and M. Hoffmann, "Time-resolved luminescence quenching in thin films of perylene-tetracarboxylic-dianhydride", *J. Lumin.*, vol. 110, pp. 309–314, 2004.
- [126] D. A. Tenne, S. Park, T. U. Kampen, A. Das, R. Scholz, and D. R. T. Zahn, "Single crystals of the organic semiconductor perylene tetracarboxylic dianhydride studied by Raman spectroscopy", *Phys. Rev. B*, vol. 61, pp. 14564–14569, 2000.
- [127] T. J. Koscic, C. L. Schosser, and D. D. Dlott, "Vibrational spectroscopy of solid state molecular dimers", *Chem. Phys. Lett.*, vol. 96, pp. 57–64, 1983.
- [128] V. Butvilas, V. Gulbinas, A. Urbas, and A. J. Vachin, "Ultrafast processes in VO-phthalocyanine film caused by intense excitation", *Radiat. Phys. Chem.*, vol. 39, pp. 165–169, 1992.
- [129] R. C. Powell and Z. G. Soos, "Singlet exciton energy transfer in organic solids", *J. Lumin.*, vol. 11, pp. 1–45, 1975.
- [130] M. v. Smoluchowski, "Versuch einer mathematischen Theorie der Koagulationskinetik kolloider Lösungen", *Z. Physik. Chemie*, vol. 92, p. 129, 1917.
- [131] S. Chandrasekhar, "Stochastic problems in physics and astronomy", *Rev. Mod. Phys.*, vol. 15, pp. 1–89, 1943.
- [132] V. M. Agranovich and M. D. Galanin, *Electronic Excitation Energy Transfer in Condensed Matter*. North-Holland Publishing Company, Amsterdam, first ed., 1982.
- [133] A. Suna, "Kinematics of exciton-exciton annihilation in molecular crystals", *Phys. Rev. B*, vol. 1, pp. 1716–1739, 1970.
- [134] D. C. Torney and H. M. McConnell, "Diffusion-limited reactions in one dimension", *J. Phys. Chem.*, vol. 87, pp. 1941–1951, 1983.
- [135] H. S. Carslaw and J. C. Jaeger, *Conduction of heat in solids*. Oxford University Press, New York, second ed., 1959.
- [136] T. Förster, "Experimentelle und theoretische Untersuchungen des zwischenmolekularen Übergangs von Elektronenanregungsenergie", *Z. Naturforsch.*, vol. 4a, pp. 321–327, 1949.
- [137] R. C. Powell, "Thermal and sample-size effects on the fluorescence lifetime and energy transfer in tetracene-doped anthracene", *Phys. Rev. B*, vol. 2, pp. 2090–2097, 1970.
- [138] I. Sokolik, R. Priestley, A. D. Walsler, R. Dorsinville, and C. W. Tang, "Bimolecular reactions of singlet excitons in tris(8-hydroxyquinoline) aluminum", *Appl. Phys. Lett.*, vol. 69, pp. 4168–4170, 1996.

Bibliography

- [139] D. Markovitsi, I. Lécuyer, and J. Simon, “One-dimensional triplet energy migration in columnar liquid crystals of octasubstituted phthalocyanines”, *J. Phys. Chem.*, vol. 95, pp. 3620–3626, 1991.
- [140] C. E. Bolton, N. J. B. Green, and S. M. Pimblott, “Modelling of geminate annihilation in quasi-one-dimensional solids”, *J. Chem. Soc., Faraday Trans.*, vol. 92, pp. 3391–3400, 1992.
- [141] J. Mi, L. Guo, Y. Liu, W. Liu, G. You, and S. Qian, “Excited-state dynamics of magnesium phthalocyanine thin films”, *Phys. Lett. A*, vol. 310, pp. 486–492, 2003.
- [142] E. Runge and E. K. U. Gross, “Density-functional theory for time-dependent systems”, *Phys. Rev. Lett.*, vol. 52, pp. 997–1000, 1984.
- [143] E. K. U. Gross and W. Kohn, “Time-dependent density functional theory”, *Adv. Quant. Chem.*, vol. 21, p. 255, 1990.
- [144] E. K. U. Gross, J. F. Dobson, and M. Petersilka, “Density functional theory of time-dependent phenomena”, *Top. Curr. Chem.*, vol. 181, pp. 81–172, 1996.
- [145] A. D. Becke, “Density-functional thermochemistry. 3. The role of exact exchange”, *J. Chem. Phys.*, vol. 98, pp. 5648–5652, 1993.
- [146] A. Schäfer, H. Horn, and R. Ahlrichs, “Fully optimized contracted gaussian-basis sets for atoms Li to Kr”, *J. Chem. Phys.*, vol. 97, pp. 2571–2577, 1992.
- [147] R. Bauernschmitt and R. Ahlrichs, “Treatment of electronic excitations within the adiabatic approximation of time dependent density functional theory”, *Chem. Phys. Lett.*, vol. 256, pp. 454–464, 1997.
- [148] F. Furche and R. Ahlrichs, “Adiabatic time-dependent density functional methods for excited state properties”, *J. Chem. Phys.*, vol. 117, pp. 7433–7447, 2002.
- [149] For a current version, go to <http://www.turbomole.de>.
- [150] N. Mataga and K. Nishimoto, “Electronic structure and spectra of nitrogen heterocycles”, *Z. Phys. Chem.*, vol. 13, p. 140, 1957.
- [151] Z. Shuai and J. L. Brédas, “Coupled-cluster approach for studying the electronic and non-linear optical properties of conjugated molecules”, *Phys. Rev. B*, vol. 62, pp. 15452–15460, 2000.
- [152] P. Tavan and K. Schulten, “The low-lying electronic excitations in long polyenes – a PPP-MRD-CI study”, *J. Chem. Phys.*, vol. 85, pp. 6602–6609, 1986.
- [153] P. Tavan and K. Schulten, “Electronic excitations in finite and infinite polyenes”, *Phys. Rev. B*, vol. 36, pp. 4337–358, 1987.
- [154] Z. Shuai, D. Beljonne, and J. L. Brédas, “Nonlinear optical processes in short polyenes: configuration interaction description of two-photon absorption and third-harmonic generation”, *J. Chem. Phys.*, vol. 97, pp. 1132–1137, 1992.
- [155] J. R. Heflin, K. Y. Wong, O. Zamani-Khamiri, and A. F. Garito, “Nonlinear optical-properties of linear-chains and electron-correlation effects”, *Phys. Rev. B*, vol. 38, pp. 1573–1576, 1988.

-
- [156] D. Guo, S. Mazumdar, S. N. Dixit, F. Kajzar, F. Jarka, Y. Kawabe, and N. Peyghambarian, "Role of the conduction-band in electroabsorption, two-photon absorption, and third-harmonic generation in polydiacetylenes", *Phys. Rev. B*, vol. 48, pp. 1433–1459, 1993.
- [157] D. Beljonne, G. E. O’Keefe, P. J. Hamer, R. H. Friend, H. L. Anderson, and J. L. Brédas, "Investigation of the linear and nonlinear optical response of edge-linked conjugated zinc porphyrin oligomers by optical spectroscopy and configuration interaction techniques", *J. Chem. Phys.*, vol. 106, pp. 9439–9460, 1997.
- [158] M. Albota, D. Beljonne, J. L. Brédas, J. E. Ehrlich, J. Y. Fu, A. A. Heikal, S. E. Hess, T. Kogej, M. Levin, S. R. Marder, D. McCord-Maughon, J. W. Perry, H. Rockel, M. R. C. Subramaniam, W. W. Webb, X. L. Wu, and C. Xu, "Design of organic molecules with large two-photon absorption cross sections", *Science*, vol. 281, pp. 1653–1656, 1998.
- [159] D. Beljonne, J. Cornil, Z. Shuai, J. L. Brédas, F. Röhlfing, D. D. C. Bradley, W. E. Torruellas, V. Ricci, and G. I. Stegeman, "General model for the description of the third-order optical nonlinearities in conjugated systems: Application to the all-trans β -carotene molecule", *Phys. Rev. B*, vol. 55, pp. 1505–1516, 1997.
- [160] D. Beljonne, Z. Shuai, J. Cornil, D. A. dos Santos, and J. L. Brédas, "On the nature of electronic excitations in poly(paraphenylenevinylene): A quantum-chemical investigation", *J. Chem. Phys.*, vol. 111, pp. 2829–2841, 1999.
- [161] E. Zojer, D. Beljonne, T. Kogej, H. Vogel, S. R. Marder, J. W. Perry, and J. L. Brédas, "Tuning the two-photon absorption response of quadrupolar organic molecules", *J. Chem. Phys.*, vol. 116, pp. 3646–3658, 2002.

List of Symbols and Abbreviations

α	Absorption coefficient
δ	Angle between two molecules in the unit cell
ϵ_n	On-site energy of FRENKEL excitons
$\phi(t)$	Temporal phase in SVEA
$\varphi(\omega)$	Spectral phase
$\varphi^{(n)}(\omega)$	n -th order derivative of φ with respect to ω
γ	Annihilation “constant” (general, may be time-dependent)
$\Gamma(t)$	Total temporal phase
Λ	Diffusion length
τ	Life time (general), pump-probe delay
$\tau_{r,1}, \tau_{r,2}$	Life times for intraband relaxation
ξ	Ratio $ P_- / P_+ $ between DAVYDOV components P_+ and P_-
1D	one-dimensional
2D	two-dimensional
3D	three-dimensional
a	1D lattice constant in stacking direction
\bar{a}	3D mean lattice constant
AC	Auto-correlation
AOPDF	Acousto-optic programmable dispersive filter
BBO	β -Barium Borate, β -BaB ₂ O ₄
BZ	Brillouin zone
c	Speed of light, unless indicated
c.c.	complex conjugate
CT(E)	Charge-transfer (exciton)
cw	continuous wave
D	Diffusion constant (or coefficient)
DC	DAVYDOV component
DS	DAVYDOV splitting
ESA	Excited state absorption
f	Coefficient describing the annihilation reaction
FE	FRENKEL exciton
FOD	Fourth order dispersion
FWHM	Full width at half maximum
GSB	Ground state bleaching (also NLA)
GVD	Group velocity dispersion
J	FRENKEL transfer integral
k	Wave number, wave vector (in the Brillouin zone)

List of Symbols and Abbreviations

$k^{(n)}(\omega)$ n -th order derivative of k with respect to ω
K Bandwidth product, wave number for the ultrasonic wave (AOPDF)
MePTCDI	... N,N'-dimethylperylene-3,4,9,10-dicarboximide
n Refractive index, population density
n_0 Initial exciton density at $t = 0$
$n_{o,e}$ Refractive index along ordinary/extraordinary axis
NLA Nonlinear absorption (also GSB)
OLED Organic light emitting diode
OMC Organic molecular crystal
OPA Optical parametric amplifier
\mathbf{p}, \mathbf{P} Transition dipoles (general)
PL Photoluminescence (time-resolved)
PTCDA 3,4,9,10-perylenetetracarboxylic dianhydride
r Anisotropy
R_F Förster radius
SE Stimulated emission
SFG Sum frequency generation
SHG Second harmonic generation
SPM Self-phase modulation
SVEA Slowly varying envelope approximation
TA Transient absorption (spectroscopy)
TOD Third-order dispersion
WLG White light generation
XC Cross-correlation

Publications

Parts of this work have been published or presented:

Articles in peer-reviewed journals

1. E. Engel, M. Koschorreck, K. Leo, and M. Hoffmann, “Ultrafast relaxation in quasi-one-dimensional organic molecular crystals”, *Phys. Rev. Lett.*, vol. 95, p. 157403, 2005
2. E. Engel, M. Koschorreck, K. Leo, and M. Hoffmann, “Excitonic intraband relaxation and polarization anisotropies in PTCDA on femtosecond and picosecond timescales”, *J. Lumin.*, vol. 112, pp. 299–302, 2005
3. E. Engel, K. Leo, and M. Hoffmann, “Ultrafast relaxation and exciton-exciton annihilation in PTCDA thin films at high excitation densities”, *Chem. Phys.*, in press
4. E. Engel, K. Schmidt, D. Beljonne, J.-L. Brédas, J. Assa, H. Fröb, K. Leo, and M. Hoffmann, “Transient absorption spectroscopy and quantum-chemical studies of matrix-isolated perylene derivatives”, *Phys. Rev. B*, submitted

Conference contributions

In case of talks, the presenters are underlined.

1. M. Koschorreck, E. Engel, K. Leo, and M. Hoffmann, “Ultrafast relaxation processes in organic molecular crystals of MePTCDI and PTCDA”, International Quantum Electronics Conference (IQEC), San Francisco, USA, 2004.
2. E. Engel, M. Koschorreck, K. Leo, and M. Hoffmann, “Ultrafast intraband relaxation and polarization anisotropies in perylene derivatives”, International Conference on Excitonic Processes in Condensed Matter (EXCON), Cracow, Poland, 2004.
3. M. Koschorreck, E. Engel, K. Leo, and M. Hoffmann, “Ultrafast exciton relaxation in quasi-one-dimensional molecular semiconductors”, 12th International Symposium on Ultrafast Phenomena in Semiconductors, Vilnius, Lithuania, 2004.
4. E. Engel, K. Leo, M. Hoffmann, K. Schmidt, D. Beljonne, and J.-L. Brédas, “Ultrafast transient absorption spectroscopy of matrix-isolated perylene-related molecules”, Quantum Electronics and Laser Science Conference (QELS), Baltimore, USA, 2005.

Dank

Ich danke allen, die zum Erfolg dieser Arbeit beigetragen haben:

Zuvorderst danke ich meinem Betreuer Prof. Dr. Karl Leo für die interessante Themenstellung auf dem noch wenig erschlossenen Terrain der Ultrakurzzeitspektroskopie an organischen Materialien, für seine Förderung meiner Arbeit sowie für sein Vertrauen, mir das Verstärkersystem zu übertragen. Sein vorbildlicher Führungsstil schafft ein zugleich offenes und motivierendes Arbeitsumfeld. Den Herren Professoren Dr. P. Petelenz (Krakau) und Dr. F. Stienkemeier (Freiburg) danke ich für ihr Interesse an meiner Arbeit und besonders für ihre Bereitschaft, sie zu begutachten.

Dem Leiter unserer Arbeitsgruppe “Exzitonenspektroskopie”, Dr. Michael Hoffmann, danke ich vielmals für zahlreiche Impulse, die mir halfen, den richtigen Weg einzuschlagen. Seine permanente Diskussionsbereitschaft und sein bewundernswertes physikalisches Wissen – besonders auf dem Gebiet organischer Halbleiter – haben sehr viel zum Verständnis beigetragen. Ferner stehe ich bei ihm für seine Geduld in seiner Schuld, mir viele theoretische Konzepte mehr als nur einmal zu erklären.

Letzteres gilt auch für Dr. Karin Schmidt und für ihre Engelsgeduld mit Experimentalphysikern. Des weiteren danke ich ihr für ihren theoretischen Beitrag in Form der Durchführung, Ausarbeitung und Deutung der Quantenchemierechnungen, welche entscheidend zur Interpretation der transienten Spektren beigetragen haben. Marco Koschorreck, meinem Mitstreiter während des ersten Jahres, danke ich herzlich für die großartige Zusammenarbeit während des gemeinsamen Erforschens der Ultrakurzzeitapparatur sowie für seine Beiträge auf dem Gebiet der Anisotropien und der Kurzzeiddynamik in MePTCDI.

Dr. Jacky Assa und Marieta Levichkova danke ich vielmals für die Anfertigung zahlreicher Proben hoher Qualität, die für diese Arbeit unverzichtbar waren.

Ich danke meinen Kollegen der vereinten Gruppe “Exzitonenspektroskopie & Ultrakurzzeitspektroskopie” für die harmonische alltägliche Zusammenarbeit, viele interessante Diskussion und (BR, VL, DM) manch experimentellen Kniff. Gemeinsam haben sie mir das Promovieren einfacher gemacht: Dr. Tobias Canzler, André Holzhey, Prof. Dr. Vadim Lyssenko, Dr. Dirk Meinhold, Dr. Ben Rosam, Rico Schüppel, Wolfgang Staroske, Marko Swoboda, und Dr. Markas Sudzius.

Für ihre Hilfe und Unterstützung danke ich den wichtigen Fachkräften unseres Institutes: Herrn Trepte in der mechanischen Werkstatt, Herrn Schmidt bei IT-Problemen und Frau Schmidt in der Verwaltung. Dem ganzen Team des “Instituts für Angewandte Photophysik” danke ich für ein motivierendes Arbeitsklima in einem harmonischem Umfeld.

Zu guter Letzt danke ich herzlichst meiner Familie für vielfältigste Art und Weise ideeller, geistiger, wissenschaftlicher... Unterstützung, nicht nur während meiner Promotionszeit. Meiner lieben KGU GBVP RCM JM für all jenes Un(an)greifbare und neue Anfänge voller Zauber.

Versicherung

Hiermit versichere ich, dass ich die vorliegende Arbeit ohne unzulässige Hilfe Dritter und ohne Benutzung anderer als der angegebenen Hilfsmittel angefertigt habe; die aus fremden Quellen direkt oder indirekt übernommenen Gedanken sind als solche kenntlich gemacht. Die Arbeit wurde bisher weder im Inland noch im Ausland in gleicher oder ähnlicher Form einer anderen Prüfungsbehörde vorgelegt.

Ich erkenne die Promotionsordnung der Fakultät Mathematik und Naturwissenschaften der Technischen Universität Dresden vom 20. März 2000 an.

Diese Arbeit wurde am Institut für Angewandte Photophysik der Technischen Universität Dresden unter der wissenschaftlichen Betreuung von Prof. Dr. Karl Leo angefertigt.

Dresden, den 25.11.2005

(Egbert Engel)

